Micromagnetic Study of Chiral Spin Textures Creation and Their Dynamics

THESIS

Submitted in partial fulfillment
of the requirements for the degree of

DOCTOR OF PHILOSOPHY

by

Sateesh Kandukuri

ID No. 2017PHXF0444H

Under the Supervision of

Prof. V Satya Narayana Murthy

BITS Pilani
Pilani | Dubai | Goa | Hyderabad

BIRLA INSTITUTE OF TECHNOLOGY AND SCIENCE, PILANI

2024

BIRLA INSTITUTE OF TECHNOLOGY AND SCIENCE, PILANI

CERTIFICATE

This is to certify that the thesis titled "**Micromagnetic Study of Chiral Spin Textures Creation and Their Dynamics**" submitted by **Sateesh Kandukuri** ID No **2017PHXF0444H** for award of Ph.D. of the Institute embodies original work done by him/her under my supervision.

Signature of the Supervisor:

Name in capital letters: V SATYA NARAYANA MURTHY

Designation: Associate Professor

Date: 04.12.2023

Acknowledgements

Throughout my PhD journey at BITS Pilani Hyderabad Campus, numerous individuals provided invaluable support and assistance in various ways. I want to express my heartfelt gratitude to every one of them, even though words may not fully convey the extent of my gratitude.

I want to start by extending my deep appreciation to my PhD mentor, Professor V Satya Narayana Murthy, for his invaluable support and encouragement during my doctoral journey. I am truly grateful to my advisor for generously sharing countless insights and consistently demonstrating patience in imparting knowledge, even when addressing fundamental queries. I would also like to extend my heartfelt appreciation to my Doctoral Advisory Committee members, Prof. P. K. Thiruvikraman and Prof. B. Harihara Venkataraman, for their valuable input, motivation, and assistance, which significantly enhanced the calibre of my thesis. Specifically, Prof. P K Thiruvikraman provided essential support with the Matlab programs vital to the completion of this thesis. I thank my fellow scholar, K Sai Anirudh from the Computer Science Department, for assisting me in installing and operating the mumax3 software at the commencement of my research.

I also want to thank Jeovani Brandão for his valuable guidance in helping me comprehend the micromagnetic studies relevant to the material I worked on. Additionally, I'd like to acknowledge and thank a group of individuals and communities: Alexander F. Schäffer, a researcher from Germany; Dr. Jeroen Mulkers, co-founder of mumax3; Edric Ellis, a developer at MathWorks; and the mumax3 community for their recommendations on post-processing micromagnetic data. Furthermore, my sincere appreciation goes out to Prof. Felipe Garcia-Sanchez from the Department of Physics at Universidad de Salamanca, Spain, for his invaluable suggestions, discussions, clarifications, and collaborative efforts that greatly contributed to the success of my thesis. I want to thank the Department of CeNSE, Indian Institute of Science, Bangalore, for granting me access to the fabrication and characterization facilities as part of the Indian Nanoelectronics Users Program.

I sincerely thank Prof. Sarmistha Banik, the current Head of the Department of Physics at BITS Pilani Hyderabad Campus, for allowing me to conduct my research smoothly and providing the necessary departmental resources. I also appreciate the Central Analytical Laboratory (CAL) at BITS Pilani Hyderabad Campus for offering their characterization facilities.

Additionally, I acknowledge BITS Pilani Hyderabad Campus for granting access to the Sharanga high-performance computational facility, which was invaluable for my simulations. I also thank the esteemed faculty of the Physics Department, particularly Prof. Kannan Ramaswamy and Prof. B Harihara Venkataraman, for their teachings in Condensed Matter Physics and Nanotechnology. I am grateful to Prof. Aravinda N Raghavan and Prof. Meenakshi Viswanathan for their guidance in the Research Methodology course and for providing insights into the necessary research hypotheses. I appreciate Prof. Sashideep Gutti and Prof. K V S Shiva Chaitanya for their valuable discussions and contributions. Special thanks to the Physics Department laboratory technicians, Mr Upendhar, Ms Ramadevi, and Mr Dharanidhar, for their unwavering assistance and support throughout my PhD journey.

Finally, I want to express my most profound and sincere gratitude to my parents, Lakshmi Kandukuri and Mayabrahma Chari Kandukuri; my wife Revathi and my son Harsha Nandan; and my sister Bhavani Tipparthi. I often regret the distance that separated me from my parents during these years. Nevertheless, their love for me has remained as deep as the ocean, regardless of where I've been. This dissertation is dedicated to them.

Abstract

Magnetism plays a significant role in a wide range of everyday applications. Magnetic materials serve as permanent magnets for sealing refrigerator doors, motors and alternators for producing electricity, soft magnets for guiding magnetic flux in transformers, functioning as memory storage devices in electronics, and enabling magnetic resonance imaging (MRI) scans in hospitals. When considering the economic impact of magnetism, the most substantial contribution comes from the energy and motor sectors. In 2020, electricity production and distribution generated an annual revenue of approximately $1.5 trillion, while electric motors accounted for $163 billion. Notably, the growth in electric transportation is rapidly expanding this sector. Additionally, the information and communication field, particularly data storage devices that have been integral to computing for six decades, represented a revenue of $56 billion. In 2019, magnetic random-access memory (MRAM) entered the market as an emerging technology. It is anticipated that this market will experience rapid growth in the upcoming years. Projections suggest that by 2026, the MRAM market is expected to reach $1 billion and continue to expand beyond that point.

Three key trends in microelectronics are downsizing components, managing power consumption, and handling vast volumes of data. Presently, the microelectronics industry is advancing towards technology nodes ranging from 5 to 3 nanometers. Another critical trend involves the continuous rise in power consumption linked to information and communication technology (ICT). The third significant trend pertains to the exponential growth of the data generated by our society. In 2020, we generated 37 ZB (equals 10^{21} bytes) of data. The overall power consumption associated with ICT keeps increasing. And more and more data centers are being constructed for cloud computing. Each of them consumes a hundred megawatts to call them for high-performance computing. The main difficulty is controlling and managing the circuits' heating. In countries like the US and Europe, 15% of the overall electrical consumption is due to ICT (21% expected in 2030). Another challenge in the current development of microprocessors is the increasing complexity of the interconnect paths. In 2003, the microelectronics industry operated at the 19 nm node, and a typical microprocessor featured approximately 10 km of interconnects. Fast forward to 2018, when the industry had progressed to the 14 nm technology node, and the interconnect length had grown significantly to around 2500 km.

As we approach fundamental limits, spintronics technology seems to be a promising solution to address these challenges. Nonvolatile storage devices are expected to contribute to the reduction of power consumption in electronic circuits. While facing growing competition from Flash Solid State Drives (SSD), Hard Disk Drives (HDD) maintain a cost advantage per gigabit of storage. Launching MRAM volume production signifies the microelectronics industry's acceptance of this hybrid Complementary Metal Oxide Semiconductor (CMOS)/Magnetic technology. This step is expected to streamline significantly the industrialization process for upcoming spintronic devices. Additionally, MRAM is anticipated to find applications in various areas such as artificial intelligence, memory computing, low-power electronics, the Internet of Things (IoT), High-Performance Computing (HPC), and cryoelectronics.

Magnetic skyrmions are unique chiral vortex spin textures in magnetic systems, known for their topological stability at nanometer scales and high mobility even at low current densities ($10^6\ A/m^2$). These characteristics have made them highly attractive for advanced memory technologies. Consequently, magnetic skyrmions are anticipated to play a pivotal role in developing next-generation energy-efficient spintronics computing. To use magnetic skyrmion as an energy-efficient information carrier, controlled creation and manipulation of chiral spin textures are required.

The first chapter of this thesis focuses on the extensive data generated by our society and its substantial impact on data center evolution, especially concerning their energy consumption. I then delve into the current CMOS technology and stress the importance of investigating options "Beyond CMOS." I also highlight the potential of spintronics and describe the shift from HDD to MRAMs. Furthermore, I introduce magnetic skyrmions as a promising path toward energy-efficient computing in the future. Chapter two highlights the significance of utilizing micromagnetic tools as a preliminary step preceding any resource-intensive experimentation. Additionally, I explore the micromagnetism theory, which serves as a foundation for conducting micromagnetic studies. Subsequent chapters 3, 4, and 5 provide a detailed examination of micromagnetic investigations related to the formation of chiral spin textures and their dynamic behaviour. These studies involve the utilization of spin-polarized currents and the magnetization reversal technique in square, rectangular, and circular nanostructures, respectively. The conclusive remarks and future prospective developments are presented in the concluding chapter.

CONTENTS

List of Tables

List of Figures

List of Abbreviations and Symbols

MRI – Magnetic Resonance Imaging

MRAM – Magnetic Random Access Memory

ICT – Information and Communication Technology

ZB – Zettabyte

SSD – Solid State Drives

HDD – Hard Disk Drives

IoT – Internet of Things

HPC – High Performance Computing

CMOS – Complementary Metal Oxide Semiconductor

IEA – International Energy Agency

TWh – Tera Watt-hours

5G – Fifth Generation

IRDS – International Roadmap for Devices and Systems

GMR – Giant Magnetoresistance

MTJ – Magnetic Tunnel Junction

STT – Spin Transfer Torque

SOT – Spin Orbit Torque

TMR – Tunnelling Magnetoresistance

eFlash – Embedded Flash

SRAM – Static Random Access Memory

DRAM – Dynamic Random Access Memory

MB – Megabyte

GB – Gigabyte

FinFET – Fin Field Effect Transistor

DW – Domain Wall

DMI – Dzyaloshinskii Moriya interaction

SANS – Small Angle Neutron Scattering

LTEM – Lorentz Transmission Electron Microscopy

MFM – Magnetic Force Microscopy

SP-STM – Spin Polarized Scanning Tunnelling Microscopy

STXM – Scanning Transmission X-ray Microscopy

DFT – Density Functional Theory

FD – Finite Difference

FE – Finite Element

GPU – Graphics Processing Unit

OOMMF – Object Oriented Micromagnetic Framework

LLG – Landau Lifshitz Gilbert

LLGS – Landau Lifshitz Gilbert Slonczewski

PSD – Power spectral density

FFT – Fast Fourier Transform

S^n – n-sphere

X – Order parameter space

Q – Topological charge

m(**r**) – Direction of the magnetic moment at **r**

r – Position vector

ν – Vorticity

η – Helicity

l_{ex} – Exchange length

M(**r**) – Magnetization vector

M_s – Saturation magnetization

$\boldsymbol{m_r}$ – Normalized magnetization unit vector

γ_0 – Gyromagnetic ratio

α – Phenomenological damping constant

$\mathbf{H_{eff}}$ – Effective field

U – Total micromagnetic energy function

μ_0 – Vacuum permeability constant

$\mathcal{E}_{ex}$ – Exchange energy density

A – Exchange stiffness constant

$\mathcal{E}_{dmi}$ – DMI energy density

D_x , D_y – In-plane components of the DMI

D_i – Isotropic DMI constant

D_a – Anisotropic DMI constant

$\mathcal{E}_{an}$ – Anisotropic energy density

K_u – Anisotropy constant

$\mathbf{u}$ – Unit vector

$\mathbf{H_{ext}}$ – External magnetic field

$\mathcal{E}_z$ – Zeeman energy density

$\mathcal{E}_d$ – Demagnetization energy density

$\mathbf{H_d}$ – Demagnetization field

$\boldsymbol{\mathcal{T}}_{STT}$ – Slonczweski spin transfer torque

$\boldsymbol{m_p}$ – Fixed layer magnetization

J_z – Current density along the z-direction

e – Charge of an electron

$\hbar$ – Reduced Planck constant

l – Thickness of the free layer

P – Spin polarization

Λ – Slonczewski parameter, which characterizes the spacer layer

ε' – Secondary spin-torque parameter

B_z – Static magnetic field

$h_z(t)$ – Alternating magnetic field

h_0 – Alternating field's amplitude

f_c – Cut-off frequency

t_p – Positive current pulse duration

t_n – Negative current pulse duration

r – Distance between the skyrmions ($|\boldsymbol{r_1} - \boldsymbol{r_2}|$)

$\boldsymbol{G}$ – Gyrotropic vector

$\widetilde{\mathcal{D}}$ – Dissipative tensor

$f(r)$ – Interaction force between the skyrmions

t_w – Current pulse width

d_{nc} – Nano contact width

CHAPTER 1

Towards Magnetic Skyrmions

- In the end, it's all about Topology.  = 

1.1 Introduction

Today, Netflix accounts for over a third of all internet traffic in the United States. It warns me of our dependence on digital data and the internet we use now. These days, when we share our memories through pictures or videos on social media platforms, they will be saved in one of the vast repositories of big data centers. The rapid advancement of digital services has led to an exponential increase in the volume of data being transmitted and processed, creating a significant demand for data centers and data transmission networks. According to the International Energy Agency (IEA) report (2022), internet users have doubled since 2010, and global internet traffic has increased by 20-fold [1, Table 1.1]. It also stated that for every bit of data that traverses the network between the data centers and end users, an additional five bits of data are transmitted within and among the data centers. Today, almost all of the world's internet traffic is routed through data centers and streaming services alone. Due to this, data centers are emerging in many places to meet business needs and Informational Technology services.

Table 1.1 Global trends in digital and energy indicators, 2015-2021. Source - IEA, 2022

	2015	2021	Change
Internet users	3 billion	4.9 billion	+60%
Internet traffic	0.6 ZB	3.4 ZB	+440%
Data center energy use (excluding crypto)	200 TWh	220-320 TWh	+10-60%
Crypto mining energy use	4 TWh	100-140 TWh	+2300-3300%
Data transmission network energy use	220 TWh	260-340 TWh	+20-60%

Data centers need vast amounts of electricity to run and keep their machinery cool. In 2020, data centers consumed an astounding 196 to 400 terawatt-hours (TWh) of energy, equivalent to 1% to 2% of global energy consumption. This exceeds the annual energy usage of entire nations like Nigeria, Colombia, and Argentina [2, 3]. The demand for data center services is rising due to 5G, media streaming, and transformative technologies like artificial intelligence, virtual reality, and blockchain. As existing technologies' efficiency improvements slow down, it's crucial to develop and adopt more efficient technologies. Government and industry efforts are vital to enhance energy efficiency and promote a sustainable future in data center operations. In addition to these measures, one effective way to prevent an unsustainable surge in energy consumption is to reconsider our ever-increasing enthusiasm for data.

1.2 Spintronics for "Beyond CMOS"

Complementary Metal-Oxide-Semiconductor (CMOS) technology has been the foundation of modern computing and electronic devices for several decades. A key element in CMOS-based electronic and logical devices is digital logic: a binary switch for on and off states. It plays a role in enabling the creation of circuits and facilitating various functions crucial for the system's success. As the demand for higher performance, increased energy efficiency, and advanced functionalities continues to grow, the limitations of CMOS technology, including power consumption, heat dissipation, scaling challenges, speed limitations, and storage density constraints, have prompted the exploration of alternative technologies.

As stated in the International Roadmap for Devices and Systems (IRDS), "Beyond CMOS" is a category of potential future digital logic technologies that seek to surpass the existing limitations of CMOS scaling [4]. One promising field that holds great potential for Beyond CMOS applications is spintronics. It involves the utilization of electron spin, in addition to its charge, to encode, process, and store information. Spintronics offers several advantages that make it suitable for advanced computing and memory systems beyond traditional CMOS. It offers non-volatility, faster data processing, high-density storage, low power consumption, compatibility with CMOS, and the potential for novel functionalities. Spin-based systems can enable the development of neuromorphic computing, quantum computing, and other emerging computing architectures.

The breakthrough identification of giant magnetoresistance (GMR) [5, 6] in 1988 by Albert Fert and Peter Grünberg stands as a momentous achievement within the realm of spintronics, which explores the manipulation and utilization of electron spin for information processing. Their work laid the foundation for exploring various phenomena related to spin transport, spin dynamics, and the behaviour of nanostructured magnetic systems under electric currents. Moreover, the practical applications of spintronics have already been realized on a large scale. GMR spin valves and magnetic tunnel junctions (MTJs) have found widespread use as magnetic field sensors in read heads for tape and hard disk drives. They have also been employed as position or proximity sensors in diverse applications such as cars and automated industrial tools.

Furthermore, the discoveries of spin-transfer torque (STT) [7, 8], spin-orbit torque (SOT) [9], giant tunnelling magnetoresistance (TMR) [10,11] in MgO-based MTJs, and large interfacial magnetic anisotropy at magnetic metal/oxide interfaces have propelled the development of scalable non-volatile magnetic random-access memories (MRAMs) [12-15]. Commercial STT-MRAMs [14] have emerged as viable alternatives to embedded flash (eFlash) memory or static RAM (SRAM) in embedded cache memories due to their easy integration with CMOS technology, low energy consumption, fast switching capabilities, and superior endurance.

1.3 HDD to MRAM

In the current landscape, digital information storage predominantly relies on flash memories, dynamic random-access memory (DRAM), and hard disk drives (HDD). Among these, HDD poses a critical challenge due to its reliance on mechanical components, namely the storage disk and read/write head. The mechanical movement introduces drawbacks such as slower operation speeds and higher power consumption. On the other hand, DRAM, consisting of non-moving parts, enables faster sequential read/write operations (HDD ~ 100 MB/s, DRAM ~ 500 MB/s) for handling large files and achieves a higher number of input/output operations per second (HDD ~ 100, DRAM ~ 100,000) [16], resulting in improved multitasking performance at reduced power consumption.

However, despite its advantages, DRAM is hindered by its volatile nature. This means that when devices are powered off, the capacitor leaks the electrical charge, leading to data loss. Flash memory, in contrast, is non-volatile since it doesn't rely on capacitors, but endurance

concerns limit it. Therefore, researchers and technologists actively explore spintronic concepts and devices as promising alternatives. Spintronics offers non-volatile characteristics and infinite endurance, making it an appealing direction for overcoming the limitations of traditional storage technologies like DRAM.

In recent developments, Intel announced the successful integration of embedded MRAM into its advanced 22 nm FinFET CMOS technology on 300 mm wafers [17]. Notably, Samsung and Everspin/Global Foundries have also unveiled their achievements in this domain, introducing a 1GB embedded MRAM on their respective technology nodes of 28 nm and 22 nm [18, 19]. The commercialization of STT-MRAMs has gained momentum, with their adoption as a viable substitute for eFlash in embedded cache memories. Additionally, STT-MRAMs show promising potential as a replacement for SRAM and even as a persistent dynamic RAM (DRAM) technology. These advancements signify significant progress in MRAM integration and pave the way for innovative memory solutions in various applications. Table. 1.2 provides the comparison of current volatile and non-volatile memories.

Table 1.2 Comparison of volatile and nonvolatile memories at advanced CMOS technology. Source – Ref. [20]

	SRAM	DRAM	STT-MRAM	SOT-MRAM
Cell size(μm^2)	0.0267	0.0026	0.014	0.0282
Write energy/bit (fJ)	76	89	<500	75
Read energy/bit (fJ)	55	58	60	15
Write latency (ns)	2.75	10	<10	1.2
Write latency (ns)	2.5	10	3.5	1
Non-volatility	no	no	yes	yes

1.4 Racetrack Memory

An innovative approach to enhance data density while maintaining thermal stability involves exploring domain walls (DW) in nanowires arranged in three dimensions instead of the current two-dimensional operation in MRAM technology. This groundbreaking concept is commonly called racetrack memory, proposed by Stuart Parkin et al. [21]. In racetrack memory, memory bits correspond to magnetic domains and are recorded by the motion of

domain walls induced by an electric current. Another promising direction that shares a similar operational principle is the utilization of magnetic Skyrmions [22, 23], which are topological spin textures formed through the Dzyaloshinskii-Moriya interaction (DMI) [24, 25]. Magnetic Skyrmions possess several advantages over domain walls, making them particularly compelling for future memory applications. One key advantage is their lower critical energy requirement for motion, enabling efficient and low-power manipulation. Additionally, Skyrmions exhibit intriguing functionalities such as topological protection, non-volatility, and high-speed operation, further enhancing their suitability for advanced memory technologies.

1.5 Magnetic Skyrmions

Magnetic skyrmions are vortex-like chiral spin textures. Over the past years, magnetic skyrmion spin textures have been observed experimentally in noncentrosymmetric magnets and ultrathin magnetic films on heavy metal substrates. These systems have broken space-inversion symmetry, and spin-orbit coupling induces an asymmetric exchange interaction. This interaction, also called Dzyaloshinskii-Moriya Interaction (DMI), is the primary source for stabilizing skyrmion spin textures.

1.5.1 Noncentrosymmetric Magnets

The first evidence of a magnetic skyrmion was reported by Muhlbauer et al. using small-angle neutron scattering (SANS) experiments in 2009 [26]. The transition metal compound MnSi is a typical weakly magnetic d-electron compound. MnSi is a cubic structure with a lattice parameter of 0.46 nm. The Mn and Si atoms are displaced from the nominal face-centred cubic position in opposite [111] directions. Four Mn and Si atoms are in a unit cell, and the cubic structure lacks inversion symmetry (B_{20}). The breakthrough experiment with neutron scattering showed the two-dimensional skyrmion lattice in MnSi perpendicular to the applied weak external magnetic field (0.16 T). The skyrmion phase is stable at temperatures below 29.5 K.

After the discovery of a magnetic skyrmion by SANS, real-space observation gave direct images of skyrmions in a helical magnet $Fe_{0.5}Co_{0.5}Si$ in 2010 by using Lorentz transmission electron microscopy (LTEM), as reported by the group led by Tokura et al. [27]. This group has also observed a helical ground state in the same material, $Fe_{0.5}Co_{0.5}Si$, in 2006 [28]. The neutron scattering experiment identified the skyrmion lattice, and the LTEM work showed the internal structure of an individual skyrmion. For the first time, it was possible to see the spin

whirls with a center spin pointing downwards and the spins at the edge pointing out of the plane.

Later, Munzer et al. reported the skyrmion phase in $Fe_{0.8}Co_{0.2}Si$ using SANS [29]. A similar magnetic skyrmion phase is found in the insulating material Cu_2OSeO_3 by using neutron scattering [30]. Depending on the material, various magnetic transition temperatures (close to RT for FeGe) and helimagnetic modulation periods (ranging from 3 nm (MnGe) to 200 nm ($Fe_{1-x}Co_xSi$)) have been reported [31-35]. In addition to SANS for bulk samples and LTEM for thin plate samples, the magnetic force microscopy (MFM) technique can be used for the real space imaging of spin textures at the surface of bulk magnetic materials.

1.5.2 Ultrathin Magnetic Films

Skyrmions have been detected in ultrathin magnetic films grown epitaxially on heavy metals. Initial studies focused on two material combinations: single layers of Fe on Ir(111) and bilayers of PdFe on Ir(111) [36, 37]. In these systems, the magnetic moments in the Fe or PdFe layer interact through ferromagnetic exchange coupling. With its high atomic number, the significant spin-orbit coupling generated by the heavy metal (Ir) leads to the emergence of substantial interfacial DMI [23]. This interaction arises due to the absence of inversion symmetry at the interface and plays a crucial role in this context. The Hamiltonian governing the interfacial Dzyaloshinskii-Moriya interaction (DMI) between neighbouring atomic spins $\mathbf{S_1}$ and $\mathbf{S_2}$ is defined as

$$H_{DMI} = (\mathbf{S_1} \times \mathbf{S_2}) \cdot \mathbf{d_{12}}$$

where $\mathbf{d_{12}}$ represents the associated DMI vector. When $d_{12} > 0$, the DMI promotes counterclockwise rotations from $\mathbf{S_1}$ to $\mathbf{S_2}$, while for $d_{12} < 0$, the system tends to favour lower energy for clockwise magnetization rotation. In systems composed of a magnetic film (Fe) and a metal (Ir), the interfacial DMI can be seen as arising from Fe-Ir-Fe triangles. The DMI vector $\mathbf{d_{12}}$ lies in the interface's plane and perpendicular to the vector connecting $\mathbf{S_1}$ and $\mathbf{S_2}$, as schematically shown in Fig. 1.1.

The relative size of the skyrmion is determined by the interplay between the exchange interaction and the interfacial Dzyaloshinskii-Moriya interaction (DMI). In the case of the two ultrathin films, the interfacial DMI is comparatively strong, while the exchange interaction is notably feeble at the interface. As a result of these factors, skyrmions within these systems exhibit smaller dimensions. Furthermore, it is crucial to apply substantial magnetic fields,

typically around 1 Tesla, and maintain low temperatures to stabilize the skyrmion phase in these materials.

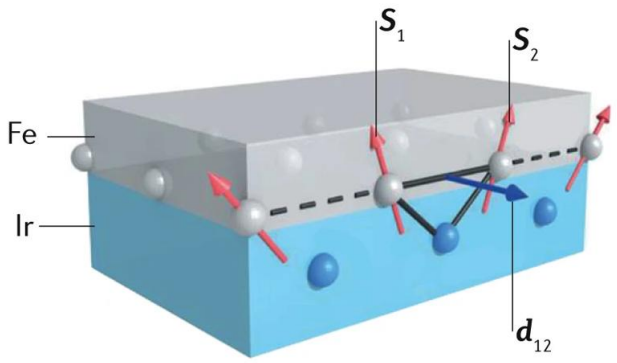

Figure 1.1 Illustration of interfacial DMI at the interface between Fe and Ir. Source – Ref. [23].

For a thorough investigation of the spin texture of a magnetic skyrmion on the surface of a magnetic layer, researchers have employed the spin-polarized scanning tunnelling microscopy (SP-STM) technique. In this approach, a ferromagnetic tip is pre-magnetized in a specific direction. The spin-polarized tunnel current varies with the cosine of the angle between the tip and the local sample magnetization. Consequently, this method enables the detection of a local magnetization component that aligns with the tip's magnetization direction. The pioneering research conducted by Wiesendanger et al. unveiled the presence of a helical spin texture with a constant spin helicity in an Mn monolayer on a W(110) surface, confirming the significant role of the DMI at the surface or interface [38]. Although ultrathin films are promising for applications, epitaxial growth is not easily compatible with standard spintronic technologies.

1.5.3 Room Temperature Skyrmions

Recent advancements in the creation of perpendicularly magnetized multilayers using sputtering deposition offer a hopeful direction for developing magnetic systems with individual skyrmions that can exist at room temperature. Several research teams have made significant strides, not only in the stabilization of skyrmions at room temperature but also in their manipulation, creation, and displacement via current-induced techniques. In multilayer structures consisting of alternating layers of a magnetic material and a heavy metal film, such as those created by stacking Co layers (each 0.6 nm thick) between Ir (1 nm thick) and Pt (1 nm thick) layers and repeating this sequence 10 times [39]. The combined effect of the DMI at the Ir/Co and Co/Pt interfaces induces the formation of skyrmions within the Co layers. These skyrmions in adjacent Co layers are interconnected through the thin non-magnetic layers. The

interconnected columns of skyrmions form a substantial magnetic volume, contributing to their stability even at room temperature and under relatively weak external magnetic fields, typically only a few tens of milli tesla. Notably, this unique magnetic pattern extends vertically throughout the multilayer structure, as observed through scanning transmission X-ray microscopy (STXM), which reveals a disordered arrangement of individual skyrmions. Recent experiments involving current pulses on these multilayers have prompted the formation of skyrmion assemblies within the phase containing magnetic domains. This specific multilayer configuration can be manufactured using conventional technologies in spintronic devices, such as magnetron sputtering deposition.

Adjusting the relative thicknesses of the Co and Fe layers within the system allows a transition from a configuration with randomly dispersed individual skyrmions to a structured skyrmion lattice. Stable room-temperature skyrmions have been successfully realized in various multilayered structures. For instance, in specific configurations such as Ta/CoFeB/TaO_x trilayers [40] with a skyrmion radius of 1 μm, (Pt/Co/Ta)×15 multilayers [41] with a skyrmion radius of 120 nm, (Pt/CoFeB/MgO) ×15 multilayers [42] with a 120 nm skyrmion radius, and Pt/Co/MgO trilayers with a 65 nm skyrmion radius. These developments hold great promise for the rapid advancement of skyrmionic devices.

Despite the widespread interest in skyrmions' insights to physicists and materials chemists, only a few noncentrosymmetric magnetic systems host these topological phases. By exploring various material compositions, crystal structures, and magnetic interactions, researchers are actively striving to establish a more comprehensive set of design principles to identify critical factors that influence the emergence and stability of skyrmions. Table 1.3 provides the existing noncentrosymmetric skyrmion materials that can be divided into three main design strategies based on the underlying crystalline lattice symmetry: polar C_{nv}, chiral T or O, and D_{2d} point groups [43, 44]. Each group hosts different types of skyrmions: Néel-type skyrmions, Bloch-type skyrmions, and antiskyrmions, respectively.

Table 1.3 Classification of skyrmion hosting materials based on the crystalline lattice symmetry.

Point group	Space group	Conductivity	Material	Sample	Temperature (K), Magnetic field (T)	Characterization	Spin texture and size (nm)	Ref.
T	$P2_13$	Metal	MnSi	Bulk	28-29.5 K, 0.162 T	SANS	Bloch-Sk, 18	26
				Film	<22.5 K, 0.18 T	LTEM	Bloch-Sk, 18	45
			FeGe	Film: 75nm Film: 15 nm	250-270 K, 0.1 T 60 K, 0.1-0.4 T	LTEM	Bloch-Sk, 70	31
			$Mn_{1-x}Fe_xGe$	Film	<250 K, 0.1-0.5T	LTEM	Bloch-Sk, <100	46
		Semi-metal	MnGe	Film	0-150 K, 0, 2.4 T	LTEM	Bloch-Sk, 3	32,33
			$Fe_{1-x}Co_xSi$	Bulk	25-30 K, 0.03-0.06 T	SANS	Bloch-Sk	34,35
			$Fe_{0.5}Co_{0.5}Si$	Film	5-40 K, 0.05-0.07 T	LTEM	Bloch-Sk, 90	27
		Insulator	Cu_2OSeO_3	Bulk	56-58 K, 0.02-0.06 T	SANS	Bloch-Sk, 60	30
				Film	5-57 K, 0.08 T	LTEM	Bloch-Sk, 50	47
O	$P4_132$	Metal	$Co_8Zn_9Mn_3$	Film	300-320 K, 0.2-0.6 T	LTEM	Bloch-Sk, 125	48
$\mathbf{D_{2d}}$	I-42m	Metal	$Mn_{1.4}Pt_{0.9}Pd_{0.1}Sn$	Film	100-400 K, 0-0.6 T	LTEM	Anti-Sk, 135	49
$\mathbf{C_{3v}}$		Metal	Fe/Ir(111)	Fe: Monolayer	11 K, 0 T	SPSTM	Neel-Sk, 1	36
				Fe: Trilayer	8 K, 2.5 T	SPSTM	Neel-Sk, 4	50
			PdFe/Ir(111)	Bilayer	<8, 1-2 T	SPSTM	Neel-Sk, 7	37
			$(Ir/Co/Pt)_{10}$	Multilayer	300 K, 0-0.08 T	STXM, XMCD	Neel-Sk, 30-90	39
			Ir/Fe/Co/Pt	Multilayer	300K, 0-0.1 T	MFM	Neel-Sk, 50-75	51
			Pt/Ru/Co/Pt/Ru/Co/Pt	Multilayer	300K, 0-0.06 T	MFM	Afm-Sk, 20-30	52
			[Co/Pd]/Ru/[Co/Pd]	Multilayer	300K, 0.04 T	LTEM	Afm-Sk, 80	53
$\mathbf{C_{3v}}$	R3m	Semi-metal	GaV_4S_8	Bulk	9-13 K, 0.02-0.16 T	SANS, AFM	Neel-Sk, 17	54
			GaV_4Se_8	Bulk	<17.5 K, 0-0.45 T	SANS	Neel-Sk, 22	55

SANS: Small Angle Neutron Scattering, LTEM: Lorentz Transmission Electron Microscopy, SPSTM: Spin-Polarized Scanning Tunneling Microscopy, STXM: Scanning Transmission X-ray Microscopy, XMCD: X-ray Magnetic Circular Dichroism, MFM: Magnetic Force Microscopy and AFM: Atomic Force Microscopy. Bloch-Sk: Bloch Skyrmion, Neel-Sk: Neel Skyrmion, Anti-Sk: Antiskyrmion and Afm-Sk: Antiferromagnetic Skyrmion.

1.6 Topology of Chiral Spin Textures

Topology and homotopy provide a comprehensive framework for understanding chiral textures' origin and stability. By incorporating the concept of winding number, a unified description emerges. This framework facilitates a straightforward analysis of the stability of these textures and their transformability. When examining magnetization configurations, the notion of topological equivalence arises for two configurations that can be continuously transformed into each other without encountering an insurmountable energy barrier. This concept is rooted in mathematical homotopy theory, which explores the deformability of functions.

Topologically nontrivial chiral spin textures can be analogously visualized as knots in a rope. Just like a knot in a rope cannot be untangled without manipulating its extremities or resorting to cutting the rope, these textures possess similar stability. The stability of these textures arises from their inherent resistance to deformation. Mutually deformable magnetization configurations can be described as mappings, $f : S^n \rightarrow X$, from the n-sphere S^n (referred to as the "base manifold") to the order-parameter space X (known as the "target manifold"). These mappings give rise to equivalence classes, also known as homotopy classes, denoted as $\pi_n(X)$. The winding number, or degree of mapping, deg(f), quantifies how many times the target manifold X wraps around the base manifold S^n. And it serves as a bijection between the homotopy classes and the integers Z, enabling the classification of different homotopy classes. Importantly, configurations with distinct winding numbers belong to different homotopy classes and, as a result, are not topologically equivalent. Consequently, these configurations cannot be continuously transformed into one another.

The magnetic material is characterized by a continuous magnetization vector field **m**(**r,** t) to establish a connection between Topology and the formalism of micromagnetics. This field represents the magnetization vector with a constant magnitude **m**, and it is defined in a continuous space parametrized by the position vector **r** and time t.

The stable topological spin textures are characterized by an invariant integer topological charge defined as [22, 23, 56]

$$Q = \frac{1}{4\pi} \iint \mathbf{m}(\mathbf{r}).\left(\partial_x \mathbf{m}(\mathbf{r}) \times \partial_y \mathbf{m}(\mathbf{r})\right) dxdy$$

where **m**(**r**) is the direction of the magnetic moment at **r** = (r cos φ, r sin φ). The topological charge, also called the skyrmion number or winding number, indicates the number of times the reduced magnetization wraps the unit sphere. Skyrmion like axisymmetric spin textures are parametrized as **m**(**r**) = [cos **Φ**(**r**) sin **Θ**(**r**), sin **Φ**(**r**) sin **Θ**(**r**), cos **Θ**(**r**)] with **Φ**(**r**) = νφ + η. Where the terms vorticity (ν) and helicity (η) are related to the magnetization rotation from the core to the periphery of the spin texture. Once the boundary conditions (spin state at the core and periphery) are fixed, vorticity determines the topological charge, and helicity determines the type of spin texture.

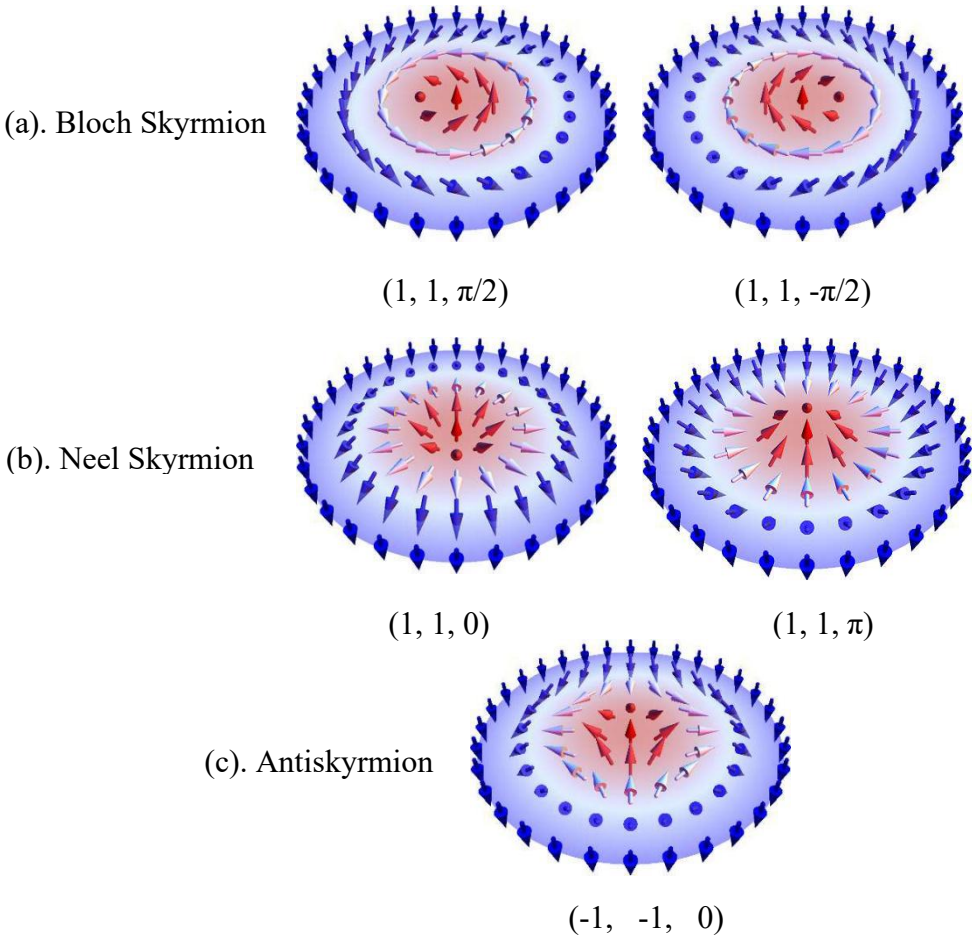

Figure 1.2 Different chiral spin texture representations based on (Q, ϕ, η) for the fixed spin orientation at the center and periphery. The two possible spin orientations for **(a)** Bloch skyrmion, **(b)** Neel skyrmion. **(c)** The helicity only makes a little difference in the spin illustration for an antiskyrmion. The arrows indicate the spin direction and the perpendicular spin component is represented by the color: red is out of the plane, white is in-plane, and blue is into the plane. Source – Ref.56

Skyrmions have a well-defined chirality between their core ($\pm m_z$) and the periphery ($\mp m_z$). There is a difference in the chirality of the skyrmions observed in the bulk compounds (Bloch skyrmions) and thin films (Neel skyrmions) due to the type of DMI. Figure 1.2 explains the two possible chiral structures for the Bloch and Neel skyrmions with the spin-up magnetization ($+m_z$) at the core are $(Q, \varphi, \eta) = (1, 1, \pm\pi/2)$ (+ $\pi/2$ corresponds to clockwise and - $\pi/2$ for the counter-clockwise direction of the spins in a plane vertical to the radial direction) and $(Q, \varphi, \eta) = (1, 1, 0 \text{ or } \pi)$ (0 corresponds to the spins divergence and π for convergence in a plane along the radial direction) respectively. The spin texture with centre magnetization $+m_z$, a negative topological charge, and negative vorticity is called antiskyrmion $(-1, -1, \eta)$. For an antiskyrmion with $|Q| = 1$, helicity varies between 0 and 2π - the structure will have a two-fold rotational symmetry with alternative Bloch and Neel-type spin rotations.

CHAPTER 2

Micromagnetism

- Spin: I'm here  *and there* 

Instead of predicting my state, anticipate how our collective actions will unfold.

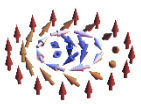

2.1 Overview

Magnetic phenomena encompass various length scales and interactions, which are crucial to understanding complex processes like magnetization reversal in magnetic materials. The micromagnetics theoretical framework [57-59] has proven to be a reliable tool to model and understand magnetization behaviour in magnetic materials at mesoscopic scales, typically ranging from nanometers to micrometres. It takes a different approach compared to purely quantum mechanical theories, such as density functional theory (DFT) [60]. DFT and related quantum theories are primarily concerned with understanding the intricate behaviour of individual atomic spins and the inherently uncertain nature of quantum systems. On the other hand, micromagnetics offers a unique perspective. The explanation of magnetic behaviour is made simpler while retaining significant quantum effects, especially those connected to ferromagnetism. Micromagnetics employs a classical approach rather than tracing the motion of individual magnetic spins. It describes the magnetization as a continuous vector field with expectation values. This method is based on the fundamental assumption that the magnetic material's internal forces are strong enough to preserve the magnetization alignment, causing neighbouring magnetic moments to align in parallel over a characteristic length scale much larger than the material's lattice constant.

Micromagnetic computations offer valuable insights into the range of magnetic phenomena, such as magnetization dynamics, hysteresis, domain structures, and domain wall motion. These insights are crucial in enhancing materials for various applications, including permanent and soft magnetic materials to data storage, spintronics, and sensing technologies.

The practical significance of micromagnetism is evident through the following primary reasons for conducting research in this field:

- Confirming or interpreting experimental findings,
- Optimizing device designs,
- Predicting new phenomena,
- Validating analytical models.

Before conducting costly or time-consuming experiments, micromagnetic simulations are crucial for investigating the effects of parameter variations. Otherwise, it is unfeasible to investigate thoroughly. Furthermore, simulations offer the advantage of monitoring quantities that can't be observed experimentally, such as individual micromagnetic energy components, thereby enhancing our understanding of the studied phenomena.

Table 2.1 List of micromagnetic software tools.

Software	Release	FE/FD	GPU capable?	Free?
LLG micromagnetics Simulator	1997	FD	No	Commercial
OOMMF	1998	FD	No	Free
micromagnus	2003	FD	No	Commercial
magpar	2003	FE	No	Free
Nmag	2007	FE	No	Free
GPMagnet	2010	FD	Yes	Commercial
FEMME	2010	FE	No	Commercial
tetramag	2010	FE	Yes	Commercial
finmag	2011	FE	No	Free
Fastmag	2011	FE	Yes	Commercial
Mumax	2011	FD	Yes	Free
micromagnum	2012	FD	Yes	Free
magnum.fe	2013	FE	No	Commercial
magnum.fd	2014	FD	Yes	Free
mumax^3	2014	FD	Yes	Free
LLG micromagnetics simulator v4.	2015	FD	Yes	Commercial
Grace	2015	FD	Yes	Free
OOMMF	2016	FD	Yes	Free
fidimag	2018	FD	No	Free
commics	2018	FE	No	Free

The main distinction is based on how these packages discretize the nanostructures: the Finite Difference (FD) or Finite Element (FE) approach. GPU: Graphics Processing Unit

2.2 Micromagnetic Tools

In the 1960s, people began using computers to address micromagnetic problems, focusing on examining domain walls [61]. These problems are notably less complex than the ones researchers tackle today. Typically, they involve one-dimensional scenarios with only a few data points. The field experienced a significant breakthrough with the release of the object oriented micromagnetic framework (OOMMF) in 1998 [62], fundamentally transforming how micromagnetic simulations are conducted and enabling more intricate investigations of magnetic phenomena at the nanoscale. Then, numerical micromagnetism made significant progress by developing many micromagnetic software tools and codes. Table 2.1 from Ref. 59 provides an overview of several micromagnetic codes.

Any micromagnetic software aims to solve the magnetization vector dynamics using a phenomenological Landau Lifshitz Gilbert (LLG) equation [63]. To achieve this, two commonly used numerical methods are finite difference and finite element methods. These methods share a fundamental approach: both break down the system's geometry into smaller unit cells or discrete elements. However, they differ in their specific approximations during this discretization process.

Finite Difference Method:

- The geometry is divided into a grid of discrete cells.
- It approximates the derivatives of the magnetization within each cell by using the values at neighbouring points. This involves calculating how the magnetization changes from one point to another.
- It is typically simpler to implement and computationally efficient for regular grid structures.

Finite Element Method:

- The geometry is divided into finite elements with various shapes, including triangles, quadrilaterals, or more complex polygons.
- It allows for a more flexible discretization of irregular geometries, making it well-suited for complex or non-uniform structures.
- It approximates the magnetization within each element using piecewise functions, and these approximations can vary in complexity and accuracy based on the chosen finite element basis functions.

The difficulty in numerical micromagnetics primarily stems from the intricate calculations needed to determine the effective magnetic field resulting from various energy factors influencing magnetization dynamics. The magnetostatic interaction is the most demanding computationally in both methods, mainly due to its long-range nature. It involves considering how the magnetization at one location affects the magnetization at all other points in the system. In our calculations discussed in the upcoming chapters, we employed mumax3 software [64, 65], which utilizes the finite difference method for numerical simulations.

2.3 Basic Assumptions in Micromagnetics

It is essential to analyze the presumptions upon which mircomagnetism relies to comprehend the behaviour of ferromagnetic materials. These assumptions arise from the nature of magnetic matter, which comprises magnetic dipoles referred to as elementary magnets. At the atomic level, these dipoles can be correlated with charged particles' spin and orbital angular momentum. In ferromagnetic materials, the spins of electrons with overlapping wave functions tend to orient themselves in parallel due to the Heisenberg exchange interaction. This alignment of spins can be locally approximated as nearly parallel, especially when the distance between two spins is much smaller than the range of the exchange interaction, known as the exchange length (l_{ex}). Therefore, for the two nearest neighbour spins, $S_i \approx S_j$ for $|r_i - r_j| < l_{ex}$

Micromagnetism operates on the assumption of a uniform density of these elementary magnets. It approximates the discrete distribution of magnetic moments ($\boldsymbol{m_i}$) using a continuous vector density termed magnetization $\mathbf{M}(\mathbf{r})$ with a constant magnitude of saturation magnetization M_s. And it is convenient to work with reduced magnetization unit vector $\boldsymbol{m_r} = \mathbf{M}(\mathbf{r})/M_s$ with $|\boldsymbol{m}(\boldsymbol{r})| = 1$, which represents the normalized direction of the local magnetization at each point in space.

2.4 Magnetization Dynamics: LLG equation

The famous LLG equation governs the magnetization dynamics in magnetic nanostructured materials.

$$\frac{d\boldsymbol{m}}{dt} = -\frac{\gamma_0}{1+\alpha^2}\left(\boldsymbol{m} \times \mathbf{H_{eff}} + \alpha(\boldsymbol{m} \times (\boldsymbol{m} \times \mathbf{H_{eff}}))\right)$$

Where γ_0 is the gyromagnetic ratio, α is the phenomenological damping constant. This equation describes the precession of magnetization under the effective field $\mathbf{H_{eff}}$. The effective field acting on the magnetization is the variational derivative of the total micromagnetic energy function U concerning $\boldsymbol{m}$.

$$\mathbf{H_{eff}} = -\frac{1}{\mu_0 M_s}\frac{\delta U[\boldsymbol{m}]}{\delta \boldsymbol{m}}$$

U considers Heisenberg's exchange interaction, DMI, anisotropic energy, Zeeman, and magnetostatic energy.

2.4.1 Exchange Energy

Exchange interaction arises from the quantum mechanical exchange coupling between neighbouring magnetic moments. It is a short-range, strong interaction that favours parallel alignment of adjacent spins, which leads to a spatial variation in the magnetization. In continuum approximation, the exchange energy density is defined as,

$$\mathcal{E}_{ex} = A\,(\nabla \boldsymbol{m})^2 = A[(\nabla m_x)^2 + \left(\nabla m_y\right)^2 + (\nabla m_z)^2]$$

The exchange stiffness constant (A in J/m) is a material property that characterizes the strength of the exchange interaction. Higher A values indicate stronger exchange coupling, favouring spatial homogeneity in the magnetization.

2.4.2 Dzyaloshinskii-Moria Interaction

As explained in the previous chapter, the DMI is an asymmetric exchange interaction from spin-orbit coupling. While the Heisenberg symmetric exchange interaction seeks to orient the adjacent spins in parallel, the DMI tries to align them perpendicularly. This interaction leads to the formation of non-collinear spin structures like magnetic skyrmions by twisting the magnetic configuration. In micromagnetics, the DMI induced at the interfaces has the form,

$$\mathcal{E}_{dmi} = D_x\left(m_z\frac{\partial m_x}{\partial x} - m_x\frac{\partial m_z}{\partial x}\right) + D_y\left(m_z\frac{\partial m_y}{\partial y} - m_y\frac{\partial m_z}{\partial y}\right)$$

Where D_x and D_y are in-plane components of the DMI (in J/m^2). The DMI couplings are known as Lifshitz invariants expressed in antisymmetric differential form. For $D_x = D_y$, the DMI is isotropic, and it favours the stabilization of skyrmions. And anisotropic DMI (D_x , $-D_y$), favours the formation of antiskyrmions.

2.4.3 Anisotropy Energy

The energy of a magnetic system depends on the direction of magnetization relative to the internal structure of a magnetic material. This dependence comes from the spin-orbit coupling of the electrons in crystals, which is described by the anisotropy energy. This energy prefers the magnetic moments to align along the easy axes of the crystal. The symmetry of the crystals confirms the angular dependence of the magnetocrystalline anisotropy energy. This energy quantifies the energy cost associated with deviating from this preferred direction. The simplest case of crystalline anisotropy is the uniaxial, manifested in hexagonal, tetragonal and rhombohedral crystal systems. In a micromagnetic framework, the average uniaxial anisotropic energy density is described as,

$$\mathcal{E}_{an} = -K_u\ (\mathbf{m}.\mathbf{u})^2$$

Where K_u is anisotropy constant (in J/m^3), and $\mathbf{u}$ is the unit vector specifying the preferred magnetization direction.

2.4.4 Zeeman Energy

Zeeman energy accounts for the interaction between the magnetization and an external magnetic field ($\mathbf{H_{ext}}$).

$$\mathcal{E}_z = -\mu_0\ (\mathbf{m}.\mathbf{H_{ext}})$$

Where μ_0 is the vacuum permeability constant. This part describes how the magnetic moments align themselves with the external field. When $\mathbf{m}$ is parallel to $\mathbf{H_{ext}}$, energy is minimized. Zeeman and uniaxial anisotropy energies are local, meaning they rely solely on the magnetization at a specific point. On the other hand, exchange energy signifies a short-range interaction, aiming to orient all spins in parallel without favouring any particular orientation.

2.4.5 Magnetostatic Energy

It is associated with the magnetostatic field generated by the magnetization distribution itself. This energy arises from the energy required to establish a magnetic field that counteracts the magnetization distribution within the material. That's why it is also called demagnetization energy.

$$\mathcal{E}_d = -\frac{\mu_0}{2}\ (\mathbf{m}.\mathbf{H_d})$$

This energy term reflects the cost of creating a magnetic field that opposes the magnetization distribution. It's especially significant in non-uniform magnetization distributions. The pre

factor 1/2 is introduced to avoid overestimating the energy. Because each magnetic moment interacts with another, there is double counting of these energies.

2.5 Current-Induced Magnetization Dynamics

The emergence of spintronics devices has prompted the development of extensions to the micromagnetic model to consider the influence of spin-transport effects [66]. The concept involves creating an effective magnetic field by manipulating the spin of conducting electrons. This method enables the integration of spintronic devices onto electronic chips while remaining compatible with CMOS technology, thereby facilitating the advancement of integrated MRAM. The key requirement is establishing a collective spin alignment known as spin-polarized current. In conventional metals such as copper, electrons lack inherent spin polarization, each electron having a randomly oriented spin. When these individual spins are combined, they cancel each other out, resulting in an overall absence of spin polarization. However, various endeavors have been undertaken to generate a net spin polarization within the electron flow. These endeavours explored a phenomenon called spin-transfer torque (STT).

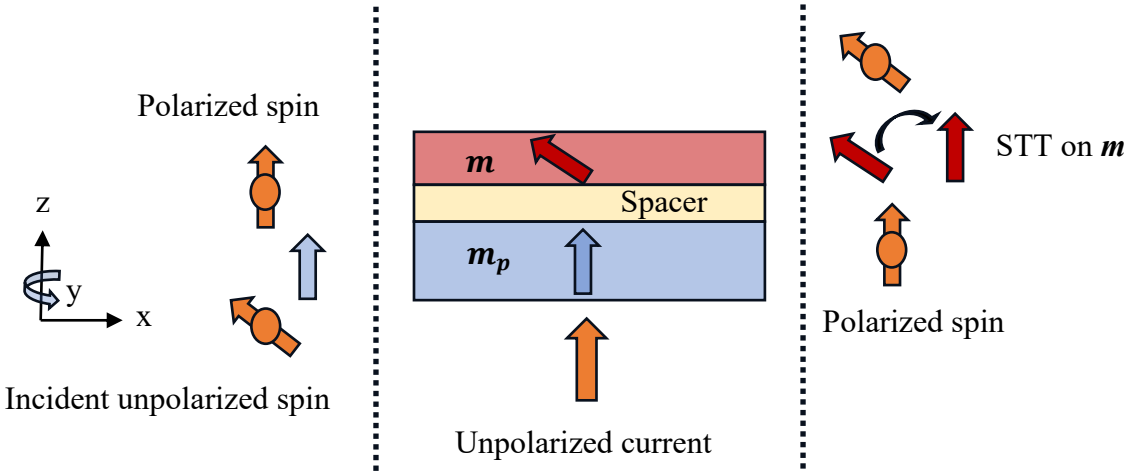

Figure 2.1 Working mechanism of Spin transfer torque. The central part of the figure shows the front view of a typical trilayer nanostructure comprised of a free layer (m) / spacer / fixed layer (m_p). The arrows (light blue and red) inside the nanostructure indicate the initial magnetization directions. When an unpolarized current passes through the nanostructure, first, it gets polarized by the fixed layer (left part of the figure). Then it alters the free layer magnetization through spin transfer torque (right part of the figure).

2.6 Spin-Transfer Torque

One method for generating a net spin polarization within an electron current involves its passage through a magnetic film (Fig. 2.1). This process enables angular momentum transfer from the magnetization to the flowing electrons, ultimately establishing a net spin polarization in the current. Slonczewski and Berger [7, 8, 67] initially laid out the theoretical foundation for this approach, and it was later confirmed through experimental implementation in the following years [68, 69]. This method involves a specific structure comprising two magnetic layers separated by a non-magnetic spacer. One layer has a fixed magnetization (in real systems, it is pinned with an antiferromagnetic layer), while the other has a free magnetization. When you use conductive spacers in these setups, they are called "spin valves," when insulating spacers are used, they are referred to as "magnetic tunnel junctions." When the electron current traverses the fixed magnetic layer, it undergoes spin polarization by exchanging angular momentum with the magnetization. Subsequently, this spin-polarized current proceeds into the free magnetic layer, transferring angular momentum by exerting torque on the magnetization. This mechanism effectively shifts spin angular momentum from the fixed to the free layer magnetization, giving rise to the term "spin transfer torque."

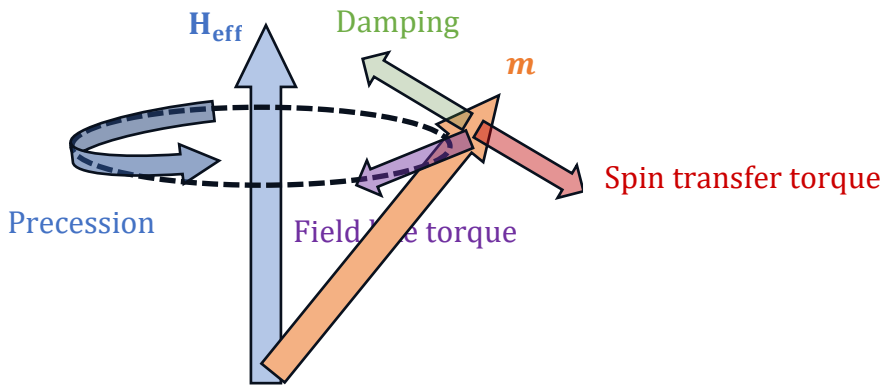

Figure 2.2 Illustration of the LLGS dynamics. The magnetization (m) precesses about the effective field direction (H_{eff}). The green arrow indicates the damping torque that aligns the magnetization towards effective field. The red arrow is the spin transfer torque, and the purple arrow is the field field-like torque from spin-polarized currents.

The hypothesis of this thesis is based on the creation of chiral spin textures using spin-polarized currents. Therefore, the LLG equation is expanded with the Slonczweski spin transfer torque ($\boldsymbol{\mathcal{T}}_{STT}$) that arises from the spin-polarized currents [64, 70]. It is defined as,

$$\boldsymbol{\mathcal{T}}_{STT} = \beta \frac{\varepsilon - \alpha\varepsilon'}{1+\alpha^2}\left(\boldsymbol{m} \times \left(\boldsymbol{m_p} \times \boldsymbol{m}\right)\right) - \beta \frac{\varepsilon' - \alpha\varepsilon}{1+\alpha^2}\left(\boldsymbol{m} \times \boldsymbol{m_p}\right)$$

$$\beta = \frac{\gamma \hbar J_z}{M_s e l}$$

$$\varepsilon = \frac{P\Lambda^2}{(\Lambda^2+1) + (\Lambda^2-1)(\boldsymbol{m} \cdot \boldsymbol{m_p})}$$

Here $\boldsymbol{m_p}$ is the fixed layer magnetization, J_z the current density along the z direction, e the charge of the electron, l the thickness of the free layer, P the spin polarization, Λ the Slonczewski parameter which characterizes the spacer layer and ε' the secondary spin-torque parameter. Figure 2.2 explains the dynamics of the free layer magnetization under spin-polarized currents using the LLG equation with Slonczweski spin transfer torque (LLGS equation). The first part of the Slonczewski spin transfer torque equation comes from the in-plane component of the STT (adiabatic), and the other part is from its perpendicular component (non-adiabatic or field-like torque). The importance of these two torques depends on the magnetic material and device structure and is critical in determining the threshold currents for magnetization switching.

CHAPTER 3

Creation of Chiral Spin Textures

- Topologically, skyrmion and antiskyrmion have opposite winding numbers. "The evolution of skyrmion and antiskyrmion from a stripe-like domain is similar to pair production phenomena."

3.1 Previous Works

Recent studies on the nontrivial topological spin texture, such as skyrmions, merons, and bimerons [71-74], are expected to be the key components of next-generation energy-efficient spintronics known as skyrmionics. For the conventional [75-78], neuromorphic [79, 80], and reservoir computing [81] applications, controlled and effective creation of spin textures is required. Until recently, these spin textures have been created by reversing the magnetization at the desired location. In 2020, a review article by Xichao Zhang et al. [56] discussed the creation of a magnetic skyrmion, including an external magnetic field, spin-polarized current, local electric field, laser, and imprinting. In 2014, Wataru Koshibae and Naoto Nagaosa showed skyrmions and antiskyrmions by local heating [82]. Antiskyrmions were observed in bulk materials with lower symmetry [83] and later were experimentally observed at room temperature in Heusler compounds with D_{2d} symmetry [49]. Hoffmann [84] and Güngördü [85] have predicted that interfacial DMI with C_{2v} symmetry in ultrathin films can form antiskyrmions.

There are different methods of creating skyrmions, as mentioned in the review article [56], we are focusing on their creation by employing a perpendicularly applied spin-polarized current. In 2012, Youngbin Tchoe and Jung Hoon Han theoretically predicted creating an isolated skyrmion using a perpendicularly applied spin current to a circular chiral ferromagnet [86]. In 2013, Sampaio et al. numerically studied the nucleation of an isolated skyrmion in a circular disk by sending the spin-polarized current through a nano-contact [87]. In the same year, Romming et al. experimentally created a single isolated skyrmion in a Pd/Fe bilayer system using a spin-polarized scanning tunnelling microscope (SP-STM) [37]. In 2016 Yuan and Wang, employing micromagnetic simulations, demonstrated the skyrmion formation in a spin valve nanostructure using a designed nanosecond current pulse [88]. They observed a skyrmion

only when the fixed layer magnetization is in the plane and perpendicular to the free layer magnetization. Yin et al. theoretically suggested creating a single skyrmion in helimagnetic thin films [89]. 2017 Legrand et al. experimentally created the skyrmions by applying a uniform spin current into nano-tracks [90]. In the same year, Woo et al. experimentally demonstrated skyrmion creation using a bipolar spin current pulse into a Pt/CoFeB/MgO multilayer [91]. Hrabec et al. also showed the creation of skyrmion by applying electric current through asymmetric electric contacts placed on a symmetric magnetic bilayer system [92].

3.2 Chiral Spin Textures Creation

In this chapter, we discuss the formation of an isolated skyrmion, skyrmion lattice, and antiskyrmion lattice using different spin-polarized current pulses into a square Co/Pd nanostructure. These spin texture formations are explained based on the magnetization reversal through spin-transfer torques [7, 8, 66, 67]. The reversal behaviour depends on the current density, pulse width, and DMI. Asymmetric behaviour of STT is observed for lower current densities. The evolution of the antiskyrmion lattice is observed by merging adjacent incomplete skyrmions for lower current densities and longer pulse widths. The formation of the skyrmion and antiskyrmion lattice has also been observed for higher current densities and lower current pulse widths through dumbbell spin textures (Q = 0).

3.3 System and Simulations

We have considered a square nanostructure consisting of a fixed/spacer/free layer of dimensions 200 nm x 200 nm (Fig. 3.1). The fixed and free layers magnetization is perpendicular to the plane of the nanostructure. The effective thickness of the Co free layer is 3 nm [93]. The spacer layer, Pd, introduces the interfacial DMI required to form magnetic skyrmions. The dynamics of the free layer are governed by the LLG equation with the Slonczewski spin-transfer torque. After defining the energies, the simulations have been done using mumax3 [64, 65] with a mesh size of 1 nm x 1nm x 1 nm. The following magnetic parameters are used in the simulations: M_s = 280 kA/m; A = 15 pJ/m; K_u = 0.06 MJ/m^3, α = 0.1 and D = 0.30 – 0.50 mJ/m^2 [94]. The spin polarization is taken as P = 0.4 and for the symmetrical free and fixed layers Λ = 1, and ε' = 0 [87, 88, 95]. The skyrmions have been created in the free layer for various electrical current pulse widths and current densities applied perpendicular to the plane of the nanostructure. The size of the skyrmion is defined as the diameter of the circle of m_z = 0 contour.

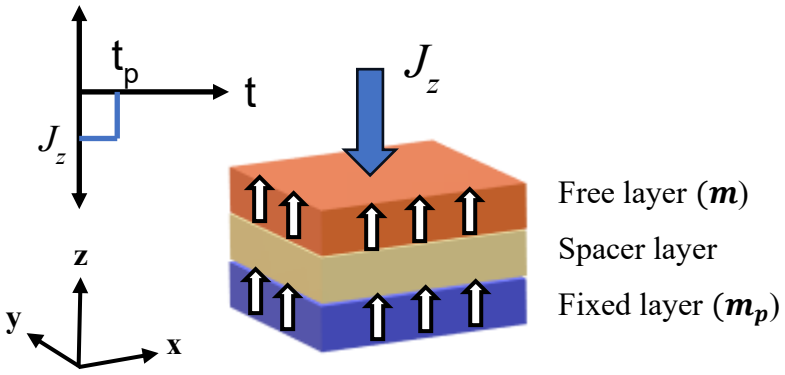

Figure 3.1 Square nanostructure with spin-polarized current direction.
The arrows inside the geometry indicate the initial magnetization directions, and the current flows along the negative z direction.

3.3.1 Current Pulse Width 1.0 ns

The work started with a current density (J_z) of 0.1 x 10^{12} A/m^2 applied perpendicular to the nanostructure in a negative z-direction for 1.0 ns. The spin-polarized current does not induce the magnetization reversal for all the ranges of DMI. Increasing the current density to 0.2 x 10^{11} A/m^2 single skyrmion is observed for D $\geq$ 0.4 mJ/m^2. The topological charge variation for J_z = 0.2 x 10^{11} A/m^2 is shown in Fig. 3.2a. For D = 0.30 mJ/m^2, from 0.73 ns (Q = 0.6) to 1.0 ns (Q = -0.7), the magnetization reversal at the edge centre moves in the counter-clockwise direction to the adjacent edge through some intermediate states (Figs. 3.2b – e). In the relaxation, the spin state is annihilated by reducing its size. For D = 0.35 mJ/m^2, the reversal behaviour is similar to 0.30 mJ/m^2 up to 0.87 ns (Figs. 3.2f and g). The magnetization reversal continued from the edge towards the centre of the nanostructure (Fig. 3.2h) and created a skyrmion-like spin texture (Q = 0.9, Fig. 3.2i) at the edge of the pulse. As the periphery of the spin texture is close to the nanostructure's edge, this spin state is annihilated by expanding its size in the relaxation. For D = 0.40 and 0.45 mJ/m^2, the captured spin states indicate the early reversal of magnetization (Fig. 3.2j and k). It has created a skyrmion (Q = 1) at the nanostructure centre (Fig. 3.2l). Once the current pulse is off, the skyrmion is stabilized through breathing mode [96], as shown in Fig. 3.2m. For D = 0.50 mJ/m^2, the topological charge variation is similar to lower DMIs up to 0.6 ns, and a skyrmion (Q $\approx$ 1) is formed at the edge of the pulse through some intermediate states (Figs. 3.2n – p). And it is stabilized through breathing mode (Fig. 3.2q). Variation of the skyrmion size with time is shown in Fig. 3.2r. The oscillations indicate the breathing mode, and the skyrmion is stabilized after 5 ns.

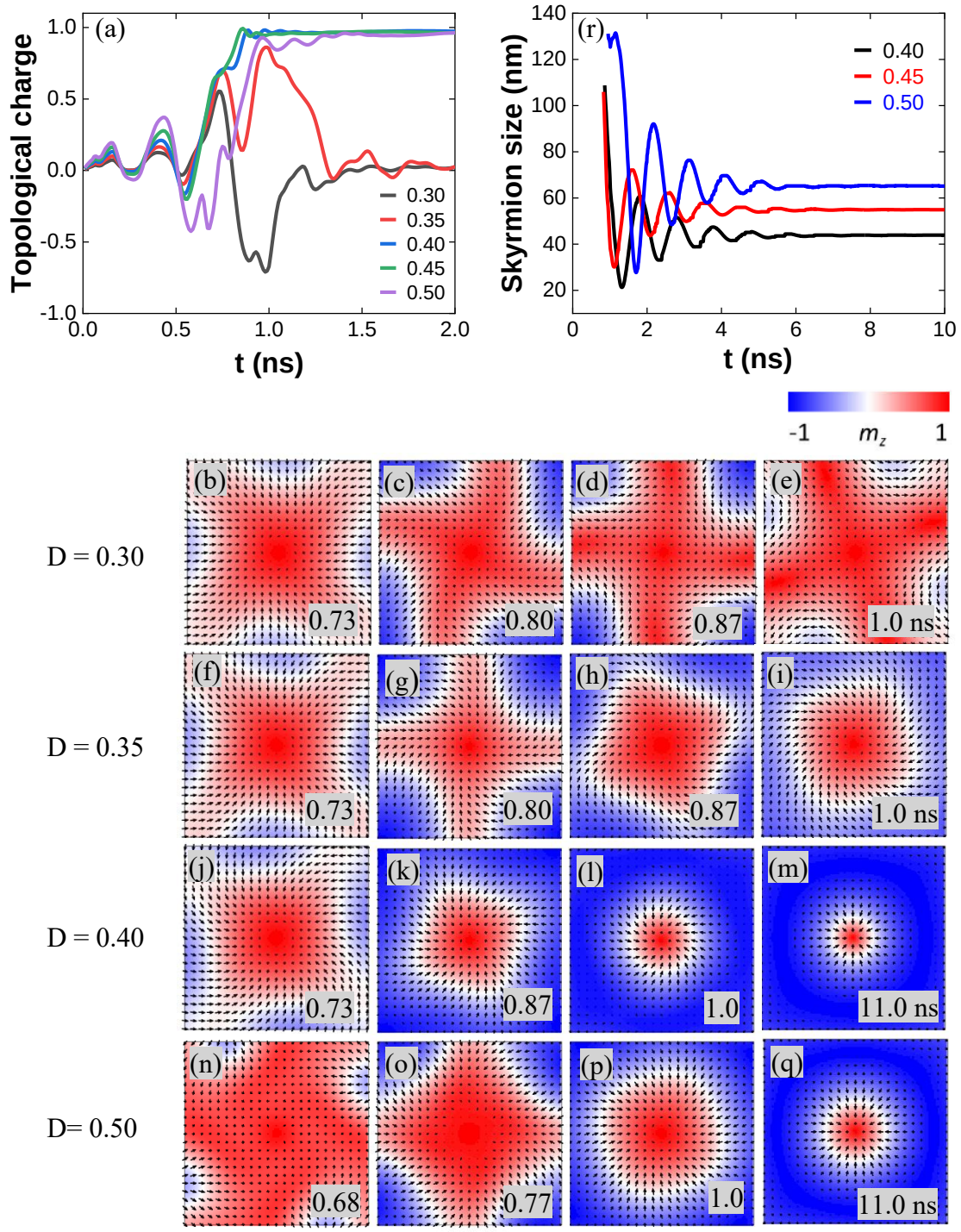

Figure 3.2 **(a)** Topological charge variation for J_z = 0.2 x 10^{12} A/m^2 and 1.0 ns pulse width. **(b) – (e)** The captured spin states reflect the topological charge variation at different times for D = 0.30 mJ/m^2, red colour indicates the magnetization along the +z direction, blue along the –z direction and white in the plane. **(f) – (i)** For D = 0.35 mJ/m^2. **(j) – (m)** For D = 0.40 mJ/m^2. **(l)** Skyrmion at 1.0 ns and **(m)** skyrmion stabilized after breathing mode. Similar type of states are observed for D = 0.45 mJ/m^2. **(n) – (q)** For D = 0.50 mJ/m^2, the size of the stable skyrmion in **(q)** at 11.0 ns is bigger than in **(m,** D = 0.40 mJ/m^2**)**. **(r)** Skyrmion stabilization through breathing mode and the size of the skyrmion increases with DMI.

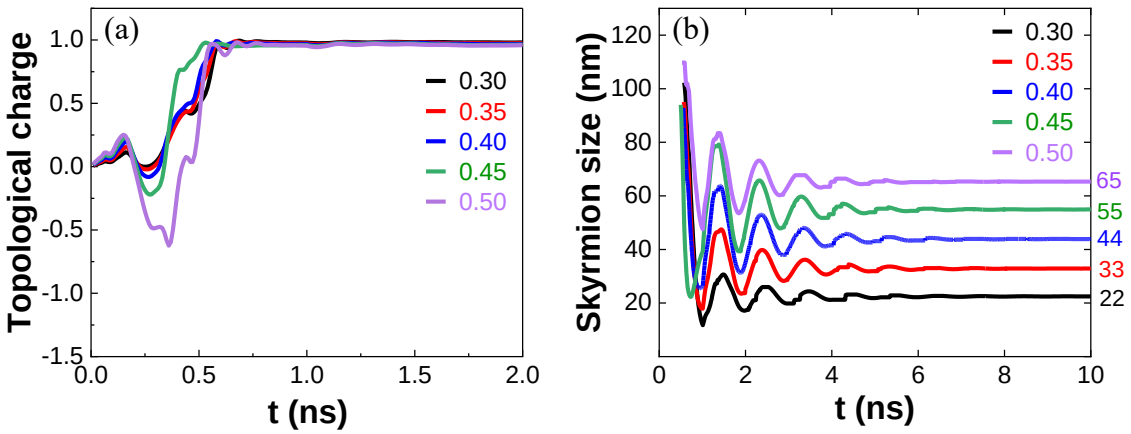

Figure 3.3 (a) Topological charge variation for J_z = 0.3 x 10^{12} A/m^2 and 1.0 ns pulse width. (b) Skyrmion stabilization through breathing mode and the size of the skyrmion increases with DMI.

Increasing J to 0.3 x 10^{12} A/m^2, a stable (1,1,π) skyrmion is formed for all the DMIs by magnetization reversal from the corners (figs. 3.3a and 3.3b show the topological charge and skyrmion size variation with time).

Fig. 3.4a shows the topological charge variation for J = 0.4 x 10^{12} A/m^2. For D = 0.30 and 0.35 mJ/m^2, magnetization reversal from the edge centres combines to form a skyrmion at the centre and is annihilated by reducing its size. For D = 0.40 mJ/m^2, the skyrmion created by reversal from the corners lengthens along the edges and expands towards the centre. Later, it is annihilated by reducing its size. For D = 0.45 mJ/m^2, the reversal from the corners moves in a counter-clockwise direction to the edge centre, as shown in Figs. 3.4b and 3.4c. The spin orientation and the topological charge indicate the incomplete formation of the (-1,1,0) skyrmions at the edges. The reversal extended and moved to the other corner, as shown in Fig. 3.4d (-1,1,η) antiskyrmions evolved by merging the boundaries of the adjacent incomplete skyrmions. The calculated topological charge -3 for the lattice shows it contains a (1,1,η) skyrmion surrounded by four antiskyrmions (Figs. 3.4e and f). The difference in the chirality of the skyrmion and antiskyrmion can be observed in the enlarged image, Fig. 3.4g. It is noted that the helicity of the skyrmion and antiskyrmions is changing due to an increase in the field-like torque (Fig. 3.5). First, the antiskyrmions are annihilated by reducing their size, followed by the skyrmion annihilation. For D = 0.50 mJ/m^2, up to 0.5 ns, the reversal process is similar to D = 0.45 mJ/m^2, creating a skyrmion at the centre and incomplete antiskyrmions at the edges

(Figs. 3.4h – 3.4k). The antiskyrmions are annihilated by moving along the edges, and then the skyrmion at the centre (Fig.3.4l) is stabilized through breathing mode.

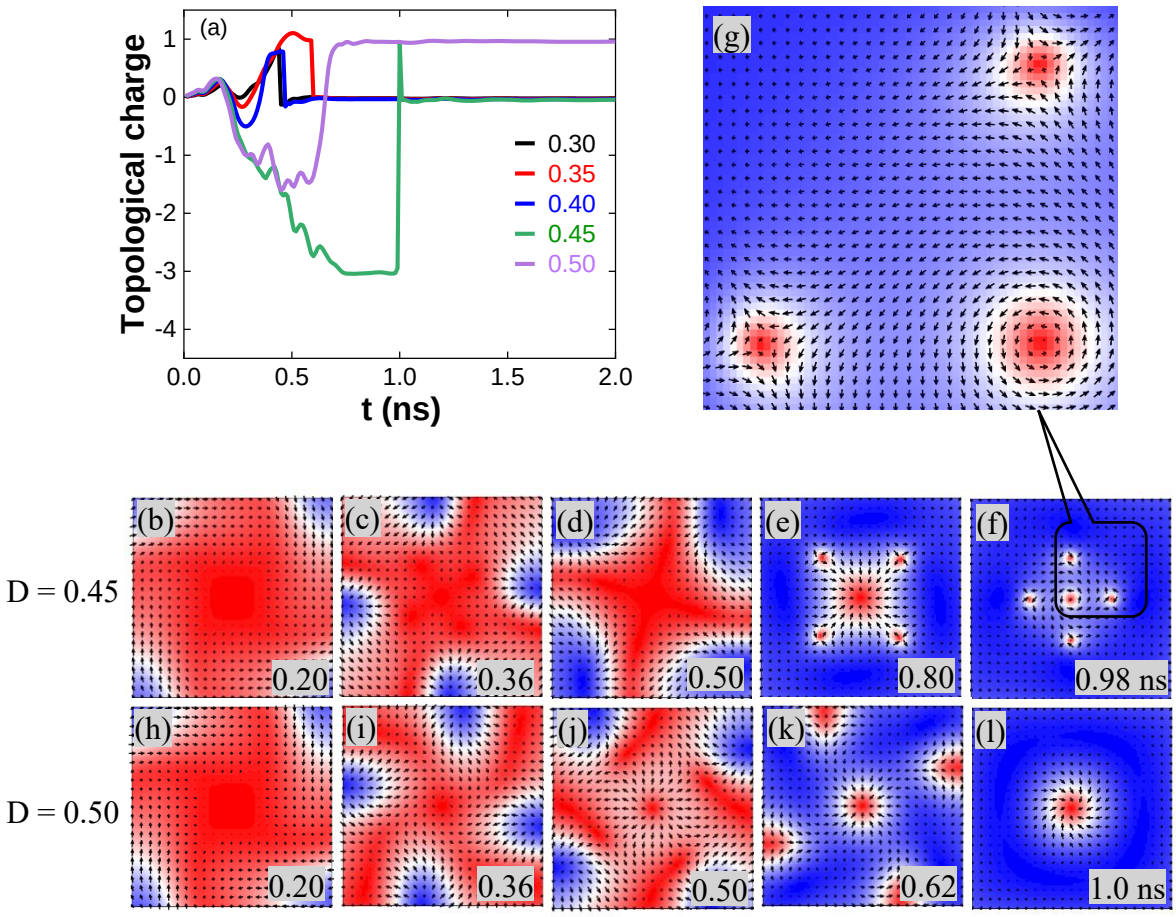

Figure 3.4 **(a)** Topological charge variation for J_z = 0.4 x 10^{12} A/m^2 and 1.0 ns pulse width. **(b) – (f)** The captured spin states reflect the topological charge variation at different times for D = 0.45 mJ/m^2, **(e)** at 0.80 ns and **(f)** at 0.98 ns have Q = -3.0 is because of the centre skyrmion with Q = +1 and four antiskyrmions with a total Q = - 4.0. **(g)** The captured enlarged image clearly shows the orientations of the spins, indicating the formation of the centre skyrmion and antiskyrmions. **(h) – (l)** For D = 0.50 mJ/m^2, **(k)** at 0.62 ns have Q = -1.5 is due to the centre skyrmion and incomplete antiskyrmions at the edges. **(l)** Centre skyrmion after the annihilation of incomplete antiskyrmions.

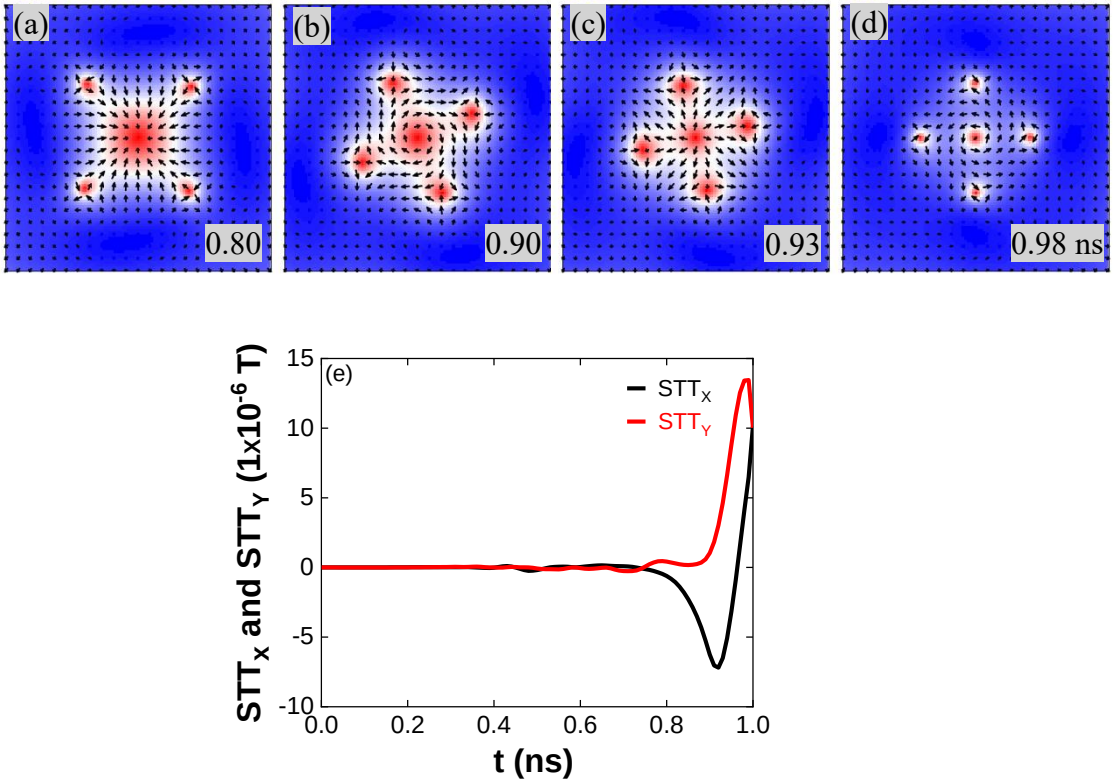

Figure 3.5 Helicity of skyrmion and antiskyrmion lattice for J_z = 0.4 x 10^{12} A/m^2, 1.0 ns pulse width and D = 0.45 mJ/m^2. **(a)** (1, 1, π) skyrmion, and (-1, -1, -π/2) antiskyrmion. **(b)** (1, 1, -π/2) skyrmion, and (-1, -1, 0) antiskyrmion. (c) (1, 1, 0) skyrmion and (-1, -1, 0) antiskyrmion. **(d)** (1, 1, π/2) skyrmion and (-1, -1, π/2) antiskyrmion. The helicity of the skyrmion and antiskyrmions change is due to the field like torque. **(e)** Field like torque variation. Large variation in STT is observed after ≈ 0.8 ns.

For J_z = 0.5 x 10^{12} A/m^2, a stable skyrmion is formed for all the DMIs except for 0.45 mJ/m^2. Fig. 3.6a shows the topological charge variation. The formation of the stable skyrmion is similar for D = 0.30 - 0.40 mJ/m^2. For the D = 0.45 mJ/m^2, magnetization reversal from the adjacent corners and around the nanostructure centre forms an antiskyrmion lattice surrounding a skyrmion (Figs. 3.6b – d). First, the skyrmion is annihilated by reducing its size (Fig. 3.6e), followed by antiskyrmion annihilation. For the D = 0.50 mJ/m^2, magnetization reversal moved from one corner to the adjacent corner in a counter-clockwise direction (Figs. 3.6f – h). Antiskyrmion lattice surrounding a skyrmion is formed due to combining the magnetization reversal from the adjacent corners (Figs. 3.6i – j). Later, at 0.96 ns, the antiskyrmions are annihilated by reducing their size, and the Skyrmion (Fig. 3.6k) is stabilized through breathing mode.

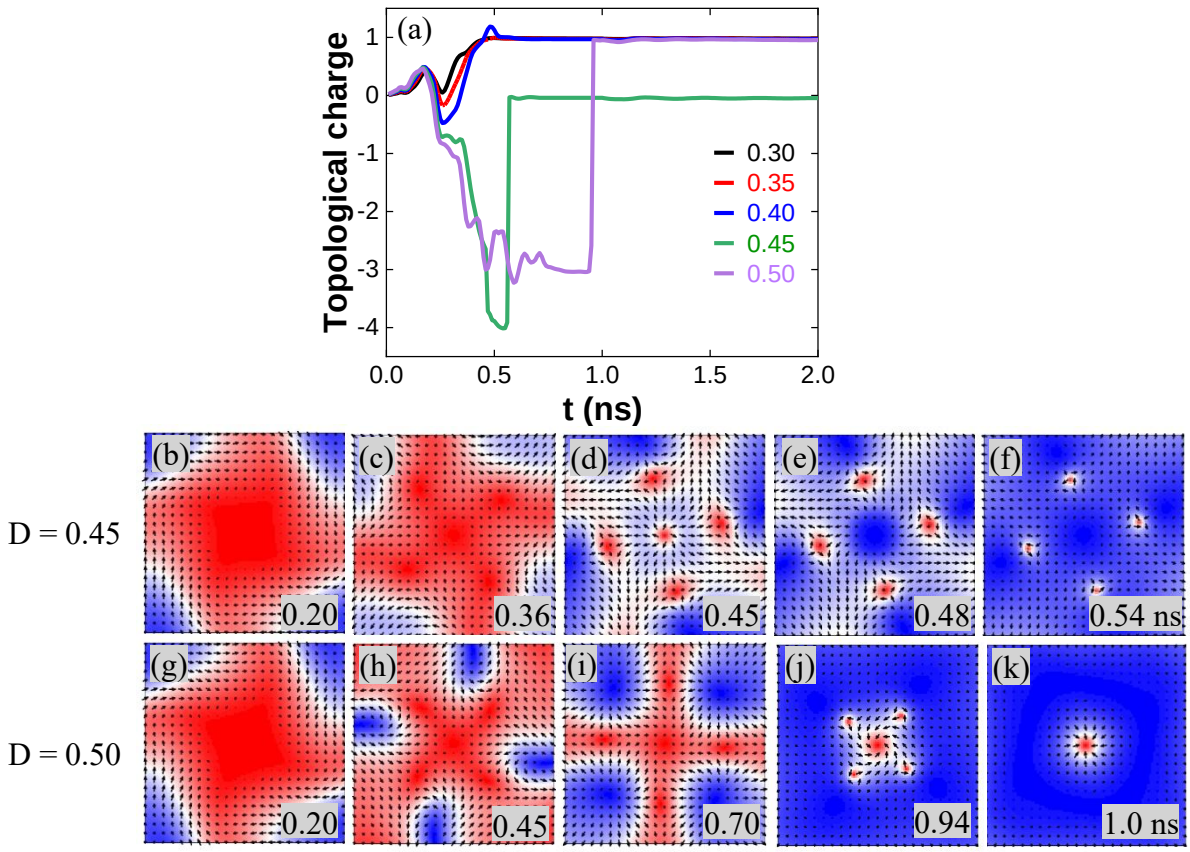

Figure 3.6 **(a)** Topological charge variation for J_z = 0.5 x 10^{12} A/m^2 and 1.0 ns pulse width. **(b) – (f)** The captured spin states reflect the topological charge variation at different times for D = 0.45 mJ/m^2, **(d)** at 0.45 ns have Q = -3.0 is because of the centre skyrmion with Q = +1 and four antiskyrmions with a total Q = - 4.0. **(e)** at 0.48 ns the centre skyrmion is annihilated and the four antiskyrmions have Q = - 4.0. **(f)** Antiskyrmions size is reduced during the annihilation process. **(g) – (k)** For D = 0.50 mJ/m^2, **(j)** at 0.94 ns have Q = -3.0 is due to the centre skyrmion and four antiskyrmions. **(l)** Centre skyrmion after the annihilation of incomplete antiskyrmions.

At higher current densities ($J_z \geq$ 0.6 x 10^{12} A/m^2), a single skyrmion is formed through the magnetization reversal from the corners of the nanostructure for all the values of DMI. The behaviour of STT is more complex and incomparable for lower current densities ($J_z <$ 0.6 x 10^{12} A/m^2, Fig. 3.7a) to different DMIs. For higher currents, a systematic variation is observed (Fig. 3.7b). The formation of the stable and unstable skyrmion at different current densities and DMIs is shown in Fig. 3.7c. As the DMI increases, the current density range for the formation of the stable skyrmion increases (region 1). For a given DMI above the threshold current density, the skyrmion is annihilated by reducing its size during the current pulse (region 2). To see the impact of the current pulse width on the stability of the skyrmion, we have reduced the pulse width to 0.5 ns.

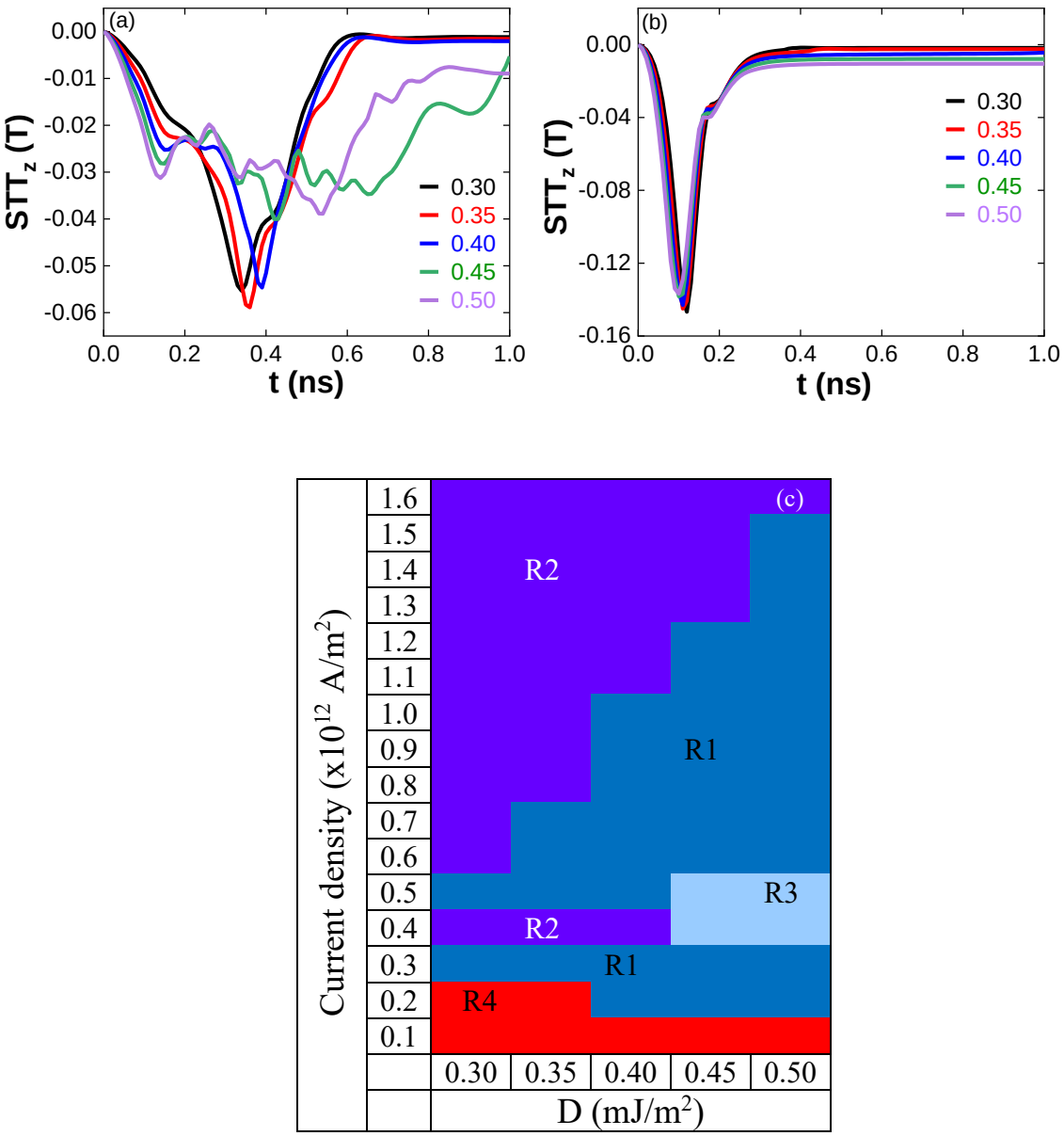

Figure 3.7 STT variation at different DMIs (a) J_z = 0.4 x 10^{12} A/m^2 and (b) J_z = 1.0 x 10^{12} A/m^2. STT is more complex and uncomparable for smaller currents (J_z < 6 x 10^{11} A/m^2), and for higher currents, systematic variation is observed. **(c) Phase diagram of stable and unstable skyrmions**. Region one (R1) indicates the stable skyrmions - as the DMI increases, the current density range for the formation of the stable skyrmion increases, region two (R2) unstable skyrmions (annihilation by reducing the size), region three (R3) antiskyrmion lattice as the intermediate state during the skyrmion formation and annihilation and in region four (R4) skyrmions have not been observed.

3.3.2 Current Pulse Width 0.5 ns

In the case of a 1.0 ns pulse and for $J_z = 0.2 \times 10^{12}$ A/m^2, a skyrmion is formed after 0.5 ns. Fig. 3.8a shows the nonlinearity in the skyrmion formation time with DMI for 1.0 ns at $J_z = 0.3 \times 10^{12}$ A/m^2. Except for D = 0.45 mJ/m^2, skyrmion formation started during the relaxation, and finally, the skyrmion annihilated for other DMIs. For D = 0.45 mJ/m^2, skyrmion formed at the end of the pulse (for 0.5 ns) and is stabilized in the relaxation.

Figure 3.8b shows the topological charge for $J_z = 0.4 \times 10^{12}$ A/m^2. Up to D = 0.40 mJ/m^2, the skyrmion formation and annihilation process is similar to a 1.0 ns pulse. For D = 0.45 mJ/m^2, the topological charge increases negatively to the edge of the pulse (Q = -2), and decreasing to zero indicates the formation and annihilation of incomplete skyrmions at the periphery of the nanostructure. For D = 0.50 mJ/m^2, the oscillatory nature in the topological charge is due to the merging of the incomplete skyrmions in the relaxation.

Figure 3.8c is the topological charge for $J_z = 0.5 \times 10^{12}$ A/m2. A skyrmion is annihilated in the relaxation for D = 0.30 and 0.35 mJ/m^2 and is stable for D = 0.40 mJ/m^2. It could be due to overcoming DMI energy than exchange energy for D = 0.40 mJ/m^2. At D = 0.45 mJ/m^2 and for 1.0 ns pulse, the antiskyrmion lattice is formed below 0.5 ns and is annihilated immediately due to the current. In the present case, since the current is switched off at 0.5 ns, the antiskyrmion lattice exists up to ~ 1.1 ns. Finally, the antiskyrmions are annihilated through the formation of incomplete skyrmions. For D = 0.50 mJ/m^2, Q = -3 (0.5 ns) to 0 (1.2 ns) indicates the formation and annihilation of incomplete skyrmions at the periphery of the nanostructure.

For higher current densities ($J_z \geq 0.6 \times 10^{12}$ A/m^2), the skyrmion formation (< 0.5 ns) and stabilization are the same as a 1.0 ns pulse. Fig. 3.8d shows the skyrmion phase diagram at different current densities and DMIs. Decreasing the pulse width from 1.0 ns to 0.5 ns increases the maximum current density required to form the stable skyrmion. We also observed the stability for a given DMI depends on the pulse width. We have investigated the skyrmion formation for 0.1 ns pulse to confirm this further.

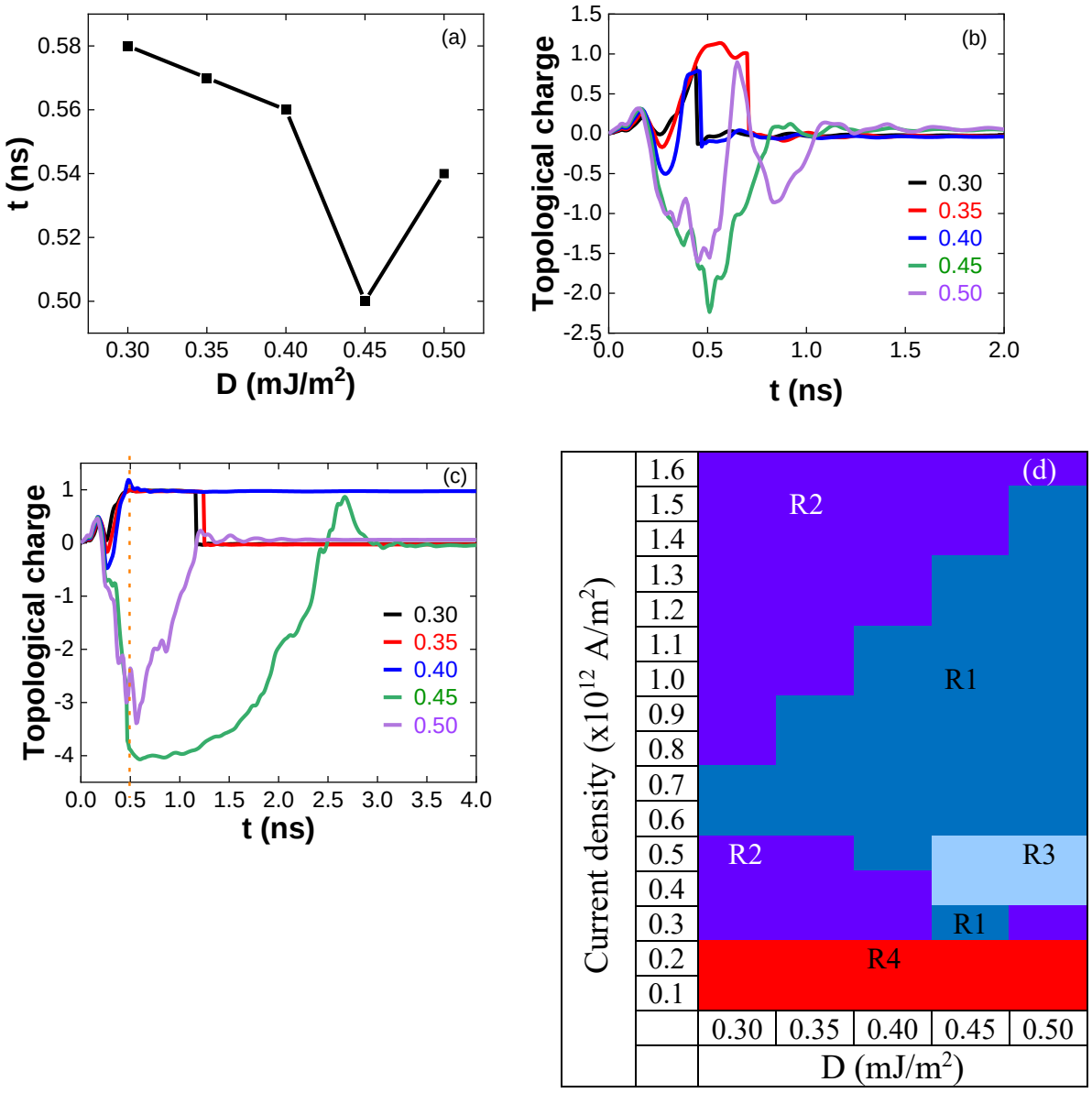

Figure 3.8 (a) Skyrmion formation time dependence on DMI for J_z = 0.3 x 10^{12} A/m^2 and pulse width 1.0 ns. Formation happens on or above 0.5 ns. Topological charge variation for 0.5 ns pulse width (b) J_z = 0.4 x 10^{12} A/m^2 and (c) J_z = 0.5 x 10^{12} A/m^2. (d) Phase diagram of stable and unstable skyrmions for 0.5 ns pulse width. R1 indicates the stable skyrmions, R2 unstable skyrmions (annihilation by reducing the size), R3 antiskyrmion lattice as the intermediate state during the skyrmion formation and annihilation and in R4 skyrmions have not been observed.

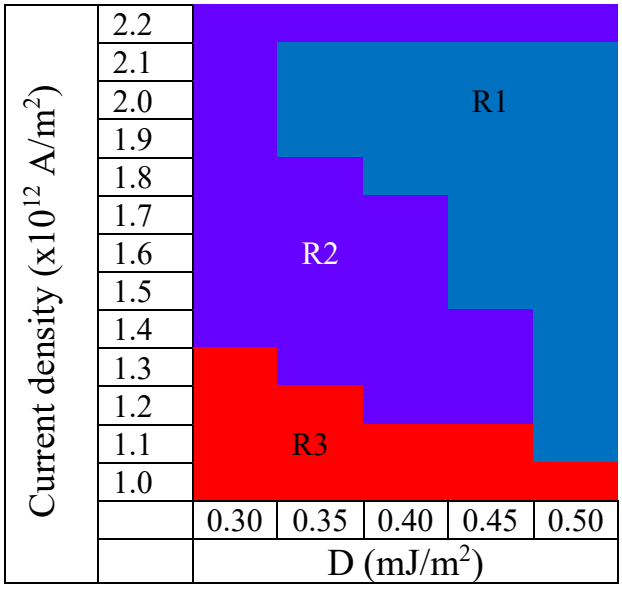

Figure 3.9 Phase diagram of stable and unstable skyrmions for 0.1 ns pulse width. R1 indicates the stable skyrmions, R2 unstable skyrmions (annihilation by reducing the size) and R3 skyrmions have not been observed. As the DMI increases, the minimum current density required for the formation of the stable skyrmion decreases. The maximum current density at which stable skyrmion observed is 2.1 x 10^{12} A/m^2 and is the same for all DMIs.

3.3.3 Current Pulse Width 0.1 ns

The skyrmion phase diagram for 0.1 ns pulse width is shown in Fig. 3.9. It can be concluded that as the DMI increases, the minimum current density required for stable skyrmion formation decreases. The maximum current density at which stable skyrmion is observed is 2.0 x 10^{12} A/m^2 and is the same for all DMIs. It is also noted that for a given DMI, the time at which the skyrmion nucleation starts depends on the current density and pulse width. The pulse width has been decreased to 0.05 ns to verify the maximum current density dependence on the skyrmion formation time. Interestingly, skyrmion lattice has been observed.

Skyrmion and antiskyrmion lattices:

The topological charge variation for J_z = 5.0 x 10^{12} A/m^2 and pulse width 0.05ns is shown in Fig. 3.10a. The magnetization reversal started from the boundary of the nanostructure. Magnetic stripes evolved symmetrically (Fig. 3.10b and c); later, a centre skyrmion surrounded by dumbbell-shaped spin textures is formed (Fig. 3.10d). For D = 0.30 mJ/m^2, the centre skyrmion is annihilated by reducing its size, followed by dumbbell spin textures moving towards the edges. For D = 0.35 – 0.50 mJ/m^2, one end of the dumbbell turns into the skyrmion and the other into the antiskyrmion (Fig. 3.10e) [97]. The central skyrmion and antiskyrmion

lattice are annihilated by reducing their size (Fig. 3.10e and f). The enlarged images of Figs. 3.10d, e, and f are shown in Figs. 3.10g, h, and i, respectively.

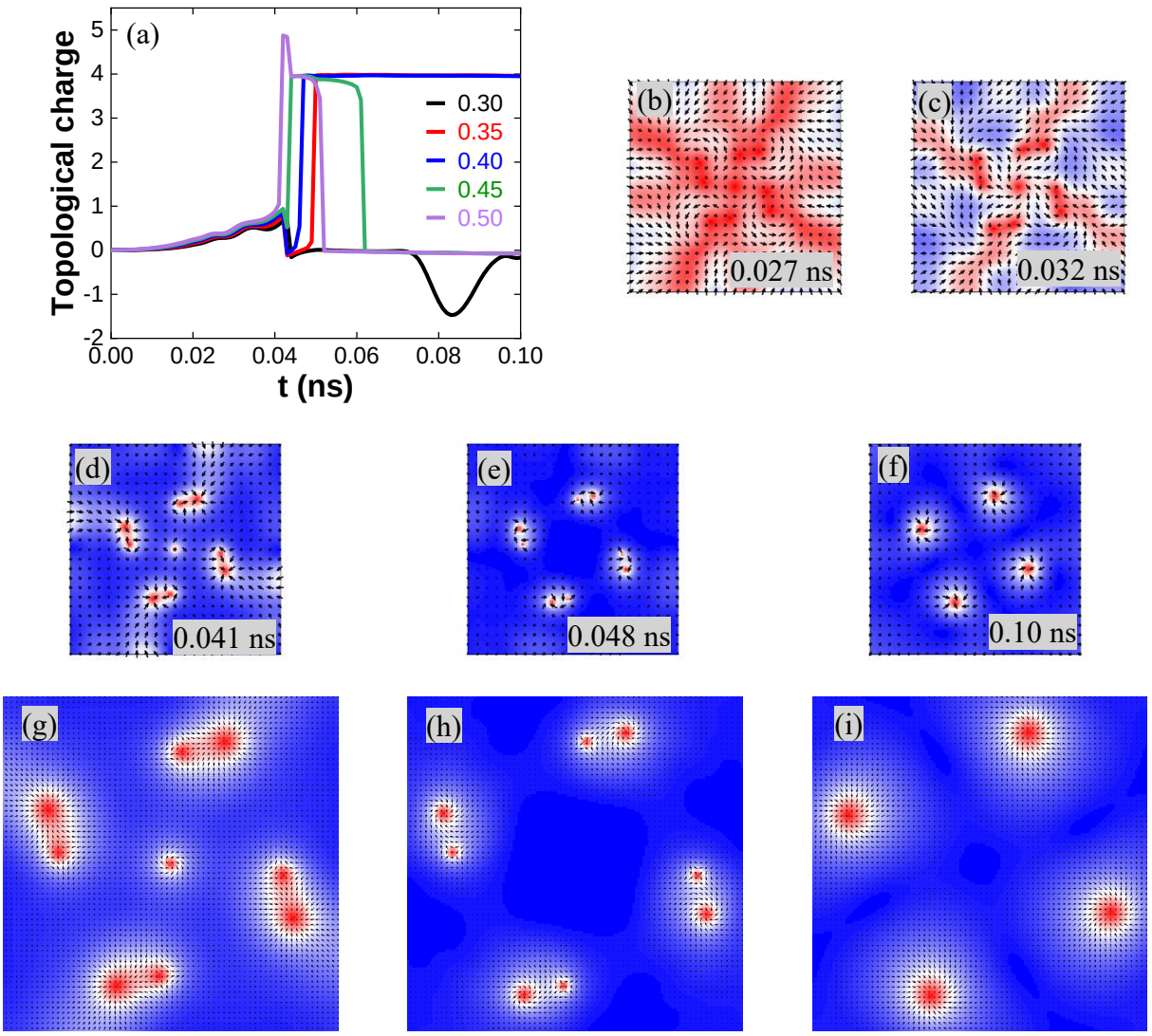

Figure 3.10 (a) Topological charge variation for J_z = 5.0 x 10^{12} A/m^2 and 0.05 ns pulse width. **(b) – (f)** For D = 0.35 mJ/m^2, spin states observed during the skyrmion lattice formation. **(b), (c)** magnetic stripes and **(d)** centre skyrmion surrounded by dumbbell spin texture. The dumbbell spin texture contains a skyrmion and an antiskyrmion with Q = 0. **(e)** Skyrmion and antiskyrmion lattice separation from the dumbbell spin texture, Q = 0 at 0.048 ns. **(f)** Skyrmion lattice after the annihilation of antiskyrmion lattice. **(g) – (i)** are the enlarged images of (d) – (f). A similar type of textures is observed for other DMIs also.

After the current pulse is switched off, for D = 0.35 mJ/m^2, the skyrmions simultaneously showed breathing mode and gyrotropic mode (Fig. 3.11a) [98, 99]. The reference circle in Fig. 3.11b helps us to understand the skyrmion motion in the relaxation process. Initially, the separation increases due to the interaction between the skyrmions (Fig. 3.11a) [100-102]. At the maximum separation, the repulsion between them goes to a minimum, and they behave like isolated skyrmions. (An isolated skyrmion away from the nanostructure centre comes to the centre through the gyrotropic motion in the relaxation [98, 99]). Hence, the separation between the skyrmions decreases. Once they come closer, the repulsion dominates, leading to the increase of separation and annihilation at the edges.

For D = 0.40 mJ/m^2, in the relaxation, the size of the skyrmion and the separation between them increases (Figs. 3.11c and d). The separation between skyrmions increases mainly due to the skyrmion–skyrmion interaction, leading to the lattice annihilation at the edges. For D = 0.45 – 0.50 mJ/m^2, the lattice is annihilated immediately after the current pulse is switched off by reducing the skyrmions' size.

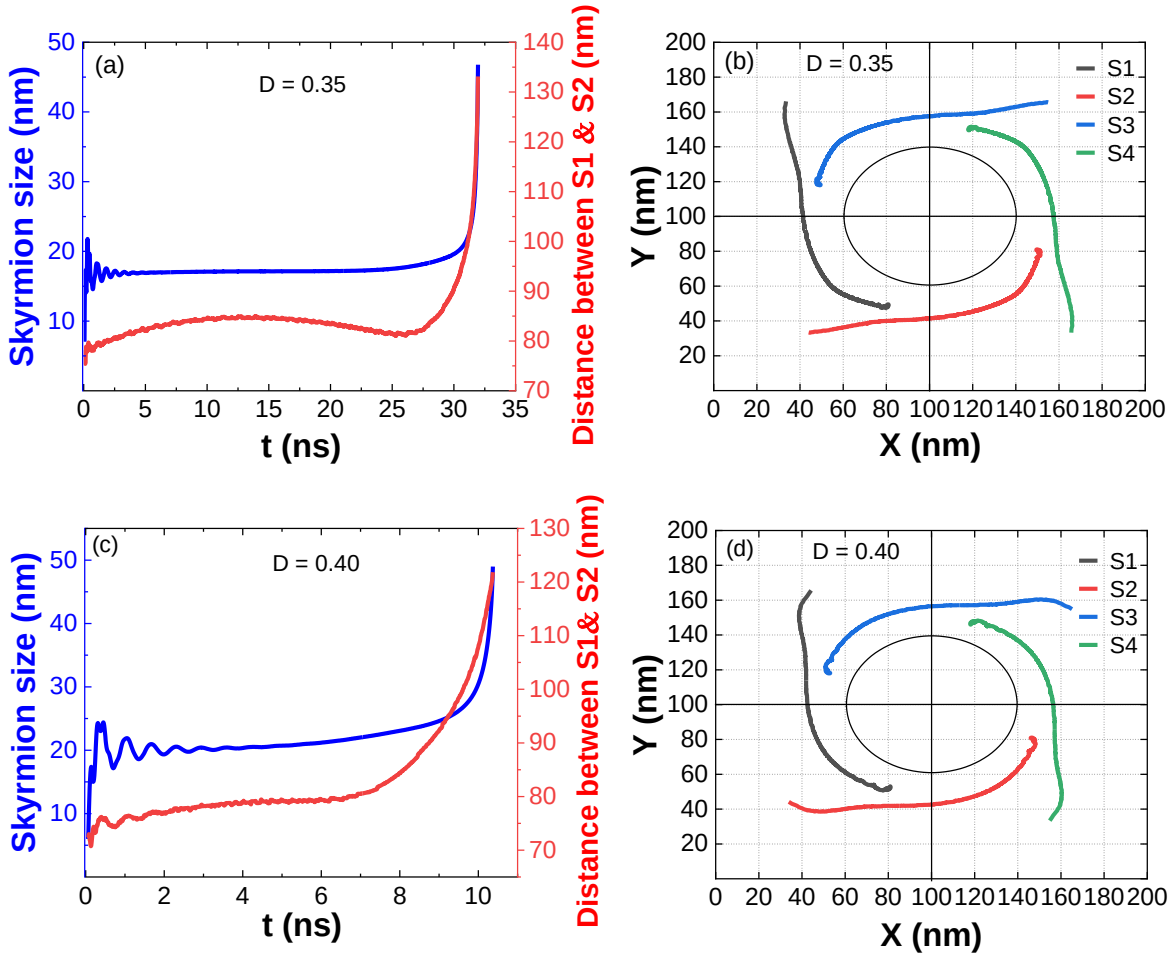

Figure 3.11 Breathing and gyrotropic modes of skyrmion lattice. **(a)** For D = 0.35 mJ/m^2 after breathing mode, the skyrmion size is almost constant before annihilation. The separation between the skyrmion 1 and 2 initially increases due to the interaction between them. At maximum separation, repulsion between the skyrmions goes to a minimum, and they behave like isolated and try to come to the centre through the gyrotropic motion. Hence, the separation between the skyrmions decreases. After reaching a minimum separation, the repulsion dominates, and the skyrmions annihilate by moving to the edges. **(b) Skyrmion movement in the lattice**. The reference circle is an eye guide to understand the skyrmion motion. All the four skyrmions have similar behaviour. **(c)** For D = 0.40 mJ/m^2, the size of skyrmion increases during relaxation leading to an increase in the repulsion and separation. **(d)** Compared to D = 0.35 mJ/m^2, the skyrmion motion from the reference circle indicates the absence of gyrotropic motion and the domination of skyrmion repulsion because of the bigger size.

Figures. 3.12a and 3.12b are the skyrmion lattice formation time and the pulse width dependence with DMIs, respectively. As the DMI increases, the formation time has decreased. The above type of skyrmion lattice formation depends on the pulse width. The minimum and maximum pulse widths decrease and the pulse width range increases with increasing DMI.

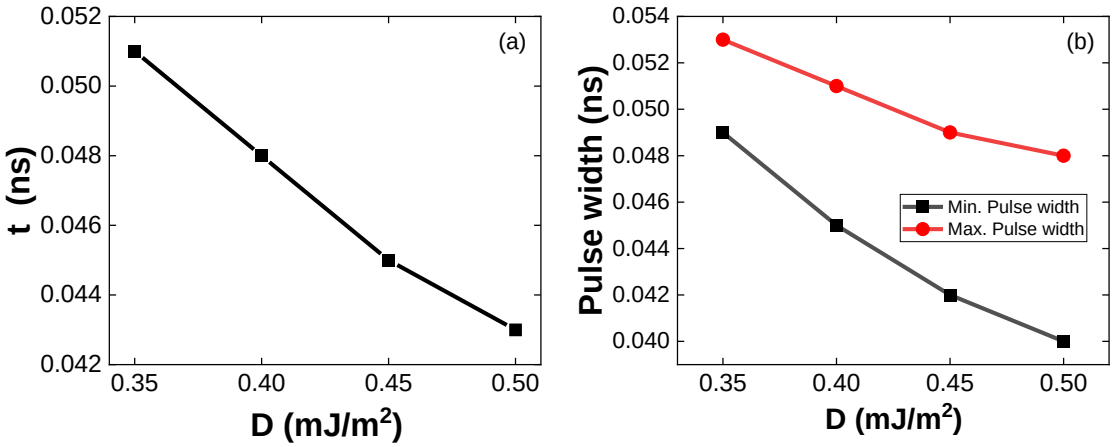

Figure 3.12 Skyrmion lattice formation time and pulse width dependence on DMI. **(a)** Formation time decreases with an increase in DMI. **(b)** The minimum and maximum pulse widths decrease, and the pulse width range increases with increasing DMI.

3.4 Edge Roughness

To confirm the edge roughness effect on the formation of the spin textures, we have run the simulations for the nanostructures with edge roughness of 2%, 5% and 10%. In Mumax3, there is no function for the edge roughness. Matlab is used to create the image files with the above per cent of edge roughness (Fig. 3.13).

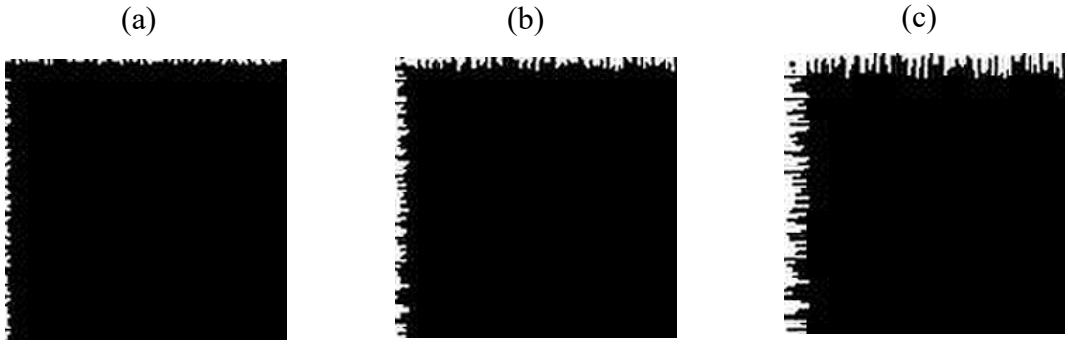

Figure 3.13 Matlab images with edge roughness of **(a)** 2%, **(b)** 5 %, **(c)** 10%

In the ideal case (0% edge roughness), we have observed the formation of antiskyrmions for D = 0.45 and 0.50 mJ/m^2 at lower current density and longer pulse width. We have chosen D = 0.50 mJ/m2 to see the effect of edge roughness. For J_z = 0.5 x 10^{12} A/m^2 and pulse width of 1.0 ns, the reversal behaviour is similar to the nanostructures without edge roughness up to 0.45 ns (Fig. 3.14). In the ideal case, we observed a stable skyrmion surrounded by antiskyrmions during the pulse time. We can see the effect of edge roughness in the formation of the antiskyrmions by merging the incomplete skyrmions at the edges. A 10% edge roughness still forms the antiskyrmions.

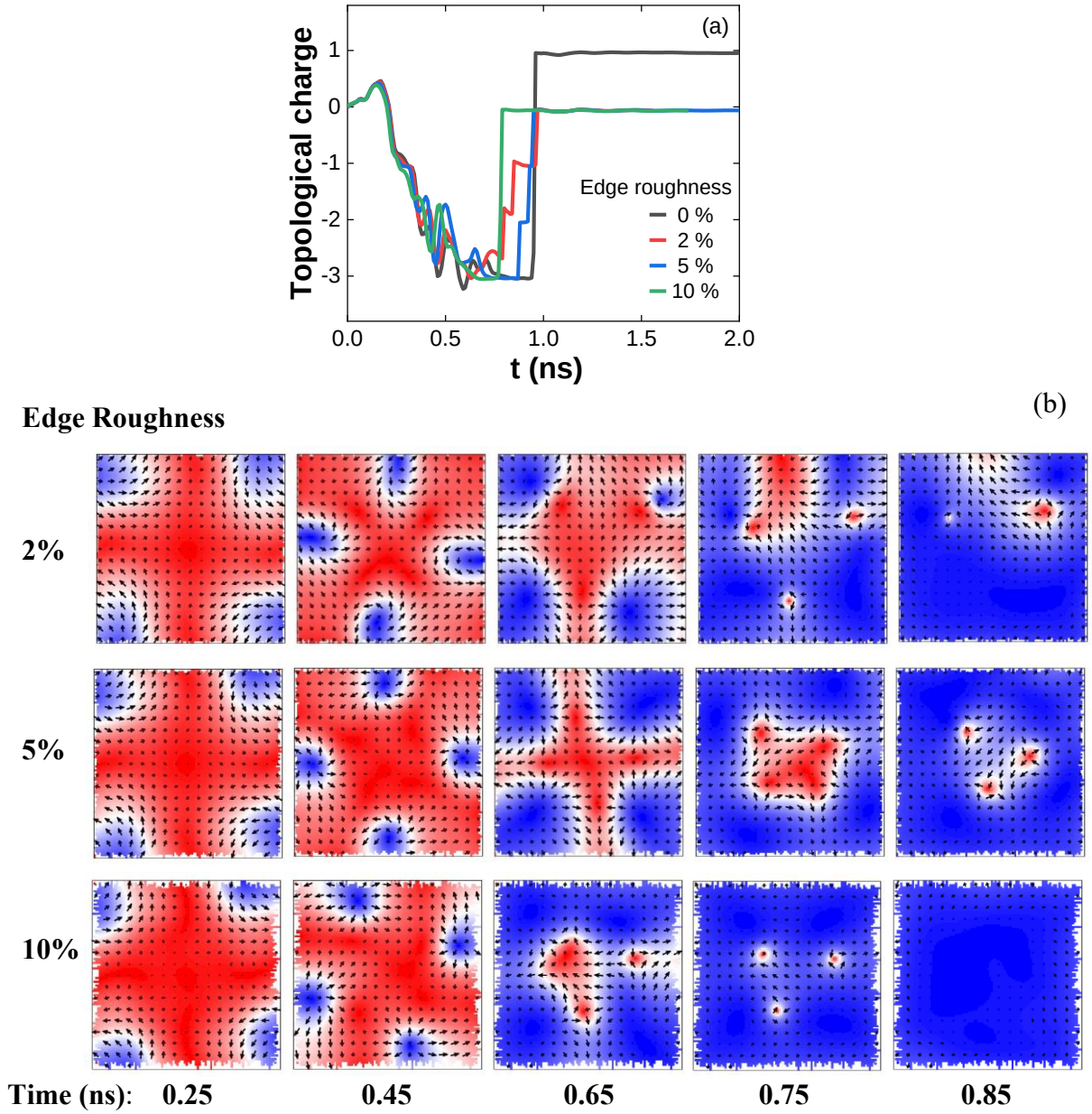

Figure 3.14 Edge roughness effect on the formation of antiskyrmions for D = 0.50 mJ/m^2, J_z = 0.5 x 10^{12} A/m^2 and pulse width of 1.0 ns.

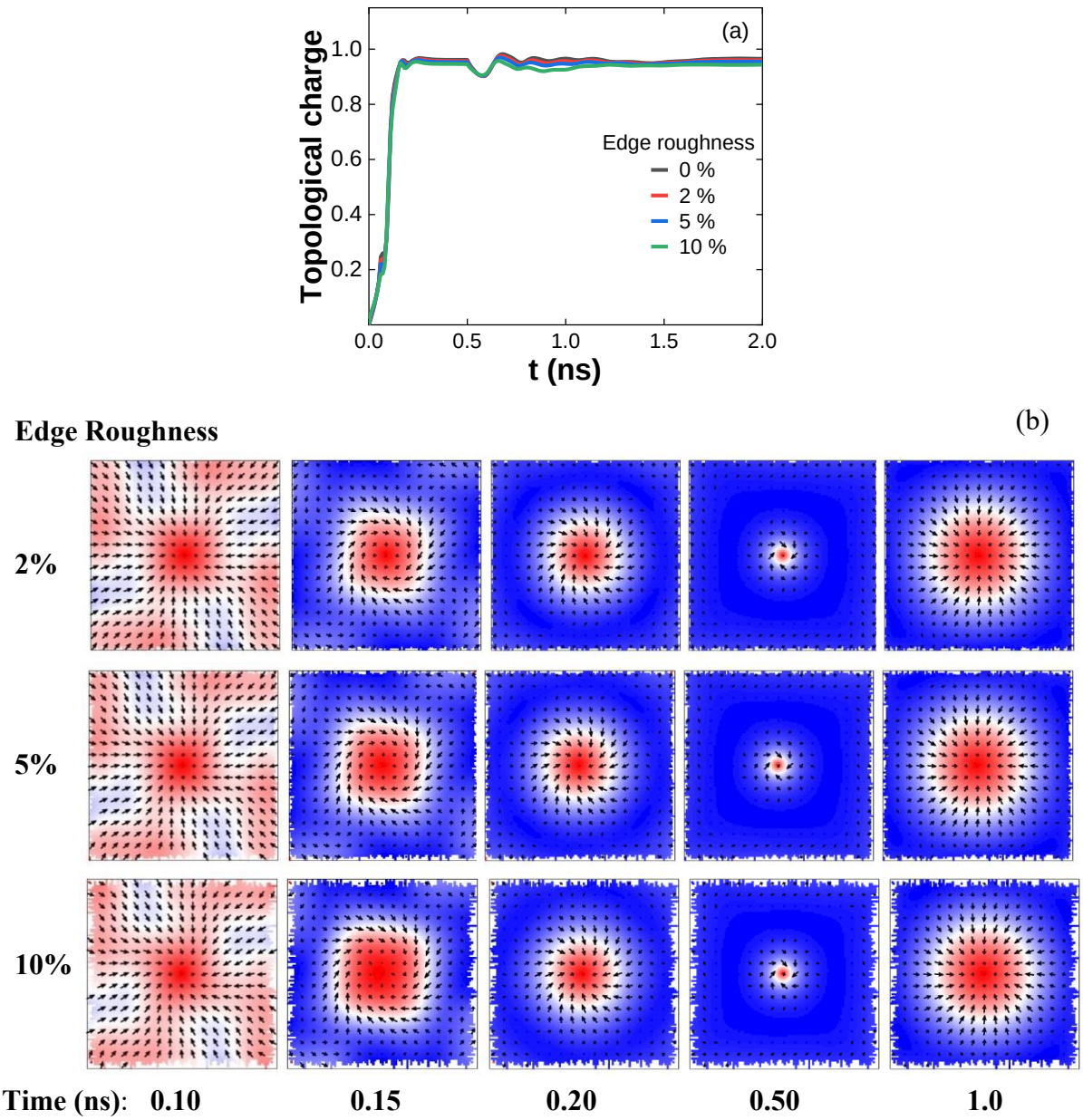

Figure 3.15 Edge roughness effect on the formation of stable skyrmion for D = 0.50 mJ/m^2, J_z = 1.0 x 10^{12} A/m^2 and pulse width of 0.5 ns.

For J_z = 1.0 x 10^{12} A/m^2 and pulse width of 0.5 ns, the magnetization reversal induced a stable skyrmion like in the ideal case, and it's not affected by the edge roughness (Fig. 3.15).

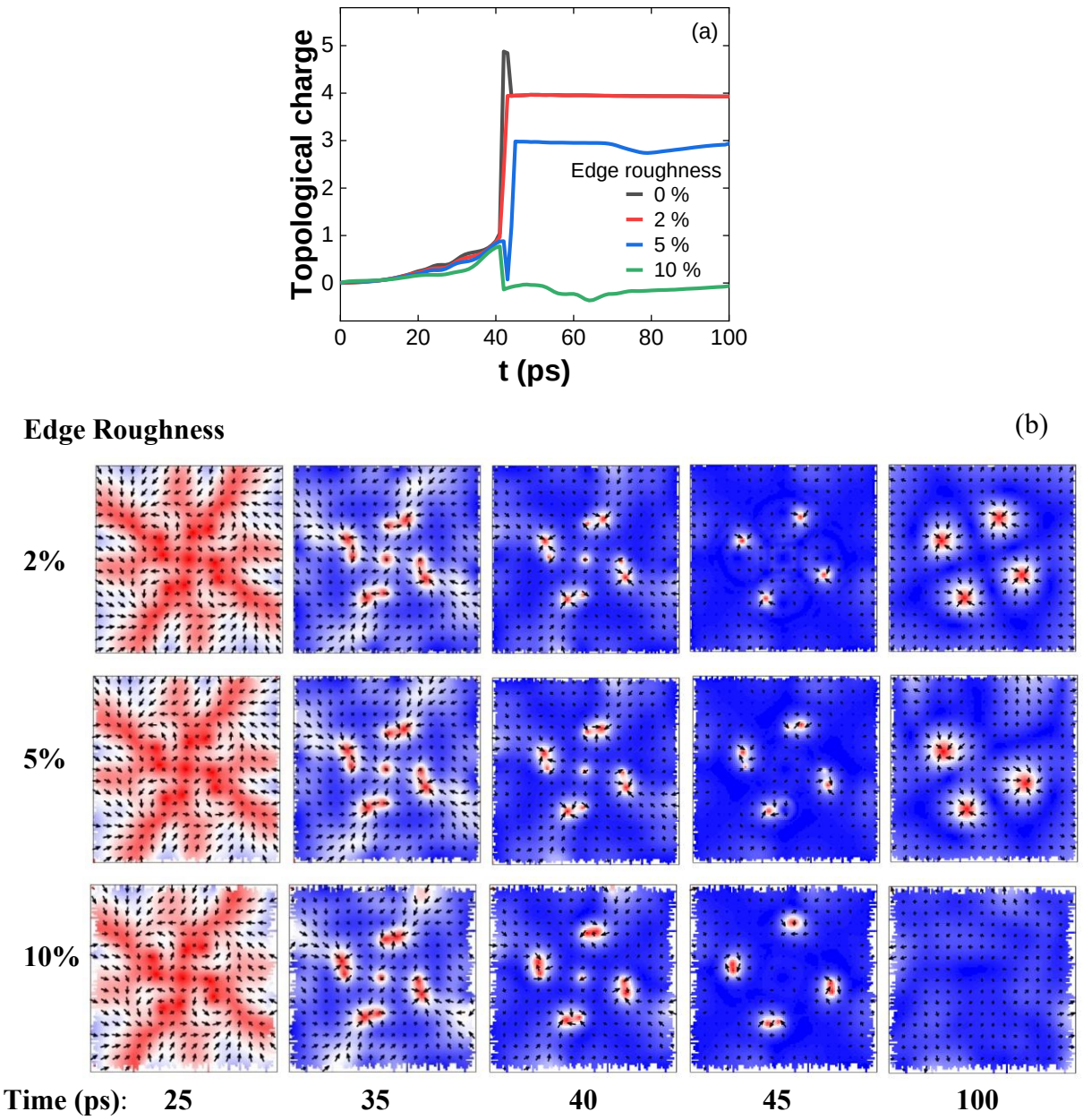

Figure 3.16 Edge roughness effect on the formation of skyrmion lattice for D = 0.50 mJ/m^2, J_z = 5.0 x 10^{12} A/m^2 and a pulse width of 45 ps.

Like in the ideal case (0% edge roughness), the centre skyrmion is surrounded by the dumbbell-shaped spin textures containing a skyrmion and antiskyrmion with topological charge, Q = 0 is formed around 40 ps (Fig. 3.16). As the edge roughness increases, the annihilation happens at early times. The above observations conclude that the formation of the antiskyrmions, stable Skyrmion and Skyrmion lattice can occur with the edge roughness (up to 10%) of the nanostructures. Even though the antiskyrmions are formed with edge roughness, they are not formed symmetrically like in the ideal case.

3.5 Summary

Our study shows how current density and pulse width influence skyrmion and antiskyrmion formation in a square nanostructure. Lower current and longer pulses create isolated skyrmions, while high current and short pulses lead to skyrmion and antiskyrmion lattices. Tuning these parameters and material properties allows for the controlled creation of stable chiral spin textures, a promising development for future devices.

CHAPTER 4

Dynamics in a Rectangular Nanostructure

- Like charge particles or magnetic poles, skyrmion spin textures of identical types show a repulsive tendency.

In the previous chapter, we showed the creation of chiral spin textures by flipping the entire confined square nanostructure magnetization [103]. The skyrmion spin texture showed a breathing mode in the relaxation. Those modes were studied by Joo Von Kim et al. in a circular nano dot structure [96]. Previously, D Capic et al. reported that a skyrmion pair with a finite separation in a square thin film is relaxed through the gyrotropic motion [102]. The studies in this chapter observe similar behaviour.

Here, we present the creation of chiral spin textures in a rectangular Co/Pd nanostructure through the magnetization reversal using spin-polarized currents. An unstable antiskyrmion evolution and breathing mode of the skyrmion during relaxation is observed while creating a skyrmion. Lorenzo Camosi et al. reported that thin film systems with C_{2v} symmetry induce anisotropic DMI [104]. We used a DMI with an opposite sign along the two perpendicular in-plane directions to study the effect of spin texture formation, and an anisotropic DMI favoured the stable antiskyrmion formation. Further, the dynamic modes of isolated skyrmion and antiskyrmion spin textures are explored with external magnetic fields. Finally, we showed the creation of a chiral spin texture pair with an asymmetric current pulse and explained the interaction between the skyrmion pair using the Thiele equation [105].

4.1 Model and Simulations

Chiral spin texture creation and dynamics are studied on a rectangular nanopillar structure using the micromagnetic simulation software mumax3 [64, 65]. The nanostructure comprises a thick reference layer at the bottom and a thin free layer at the top, separated by a spacer layer (Fig. 4.1a). The magnetization of the free ($\boldsymbol{m}$) and reference layer ($\boldsymbol{m_p}$) are defined perpendicular to the plane of the nanostructure. The free layer's magnetization is manipulated

through spin-polarized currents for the chiral spin texture creation. The LLGS equation describes the energy minimization dynamics of the free layer.

Simulations are performed on free layer dimensions of 250 nm x 150 nm x 3 nm with discretized cell sizes of 1 nm x 1nm x 1nm. The material parameters are considered from a symmetric Pd/Co/Pd multilayer system [94], which possesses an interfacial DMI required to form chiral spin textures. We considered isotropic DMI for creating skyrmions and anisotropic DMI for antiskyrmion with an exchange constant of A = 15 pJ/m, a saturation magnetization of M_s = 280 kA/m, a uniaxial anisotropy of K_u = 0.06 MJ/m^3, and a Gilbert damping constant of α = 0.1. The following sections are devoted to the study of chiral spin texture formation and its dynamics using the current densities in the range -0.1 x 10^{12} to -5.0 x 10^{12} A/m^2 and different pulse widths (0.5 ns for isolated skyrmions and 30 – 150 ps for skyrmion pair) for DMI magnitudes of 0.30 to 0.50 mJ/m^2. For isolated chiral spin texture creation, the spin-polarized current is applied in a negative z-direction $(-J_z)$, and for the spin texture pair creation, asymmetric pulses are applied. We used the same spin polarization of P = 0.4 and $\varepsilon' = 0$ in all the cases.

4.2 Creation of an Isolated Chiral Spin Texture

4.2.1 Skyrmion

Initially, the free layer is uniformly magnetized $(\hat{z})$ and then relaxed to obtain the equilibrium state in the presence of isotropic DMI (D_i). Then, a spin-polarized current density is applied for 0.5 ns in this study. Depending on the current value and the DMI constant, we can find different final states. The current density (J_z) up to -0.3 x 10^{12} A/m^2 didn't induce the magnetization reversal for any of the DMI values. For J_z = -0.4 x 10^{12} A/m^2, D_i = 0.30 and 0.35 mJ/m^2, magnetization reversal started across the opposite corners and moved along the edges to the other corners. Due to the short current pulse width (0.5 ns), this reversal is annihilated later. For D_i = 0.40 to 0.50 mJ/m^2, spin reversal merging from opposite corners seems to create an antiskyrmion, but it collapsed immediately.

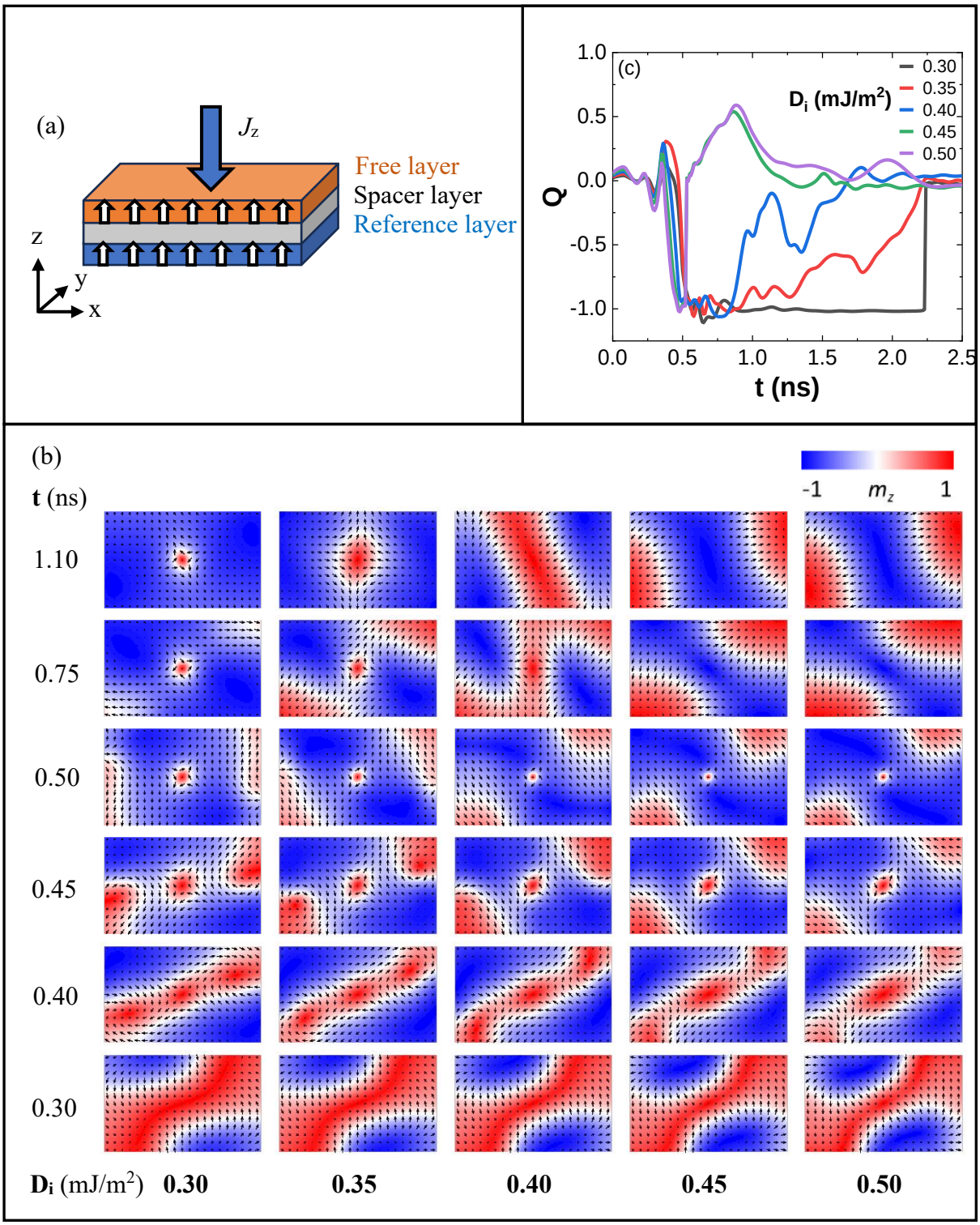

Figure 4.1 (a) Rectangular nanostructure with spin-polarized current direction. The arrows inside the geometry indicate the initial magnetization directions, and the current flows along the -z direction. (b) and (c) represents the spin states and corresponding topological charge variation for J_z = -0.5 x 10^{12} A/m^2. The spin states at different instants for D_i = 0.30 – 0.50 mJ//m^2 show the evolution of antiskyrmion. The topological charge Q = -1 for the corresponding spin state indicates that the spin texture is an antiskyrmion.

The spin states and topological charge variation for J_z = -0.5 x 10^{12} A/m^2 are shown in Figs. 4.1b and 4.1c, respectively. For all DMIs, an unstable antiskyrmion evolved from spin reversal merging at the end of the pulse. The antiskyrmion annihilated at 2.24 ns for 0.30 mJ/m^2 DMI. It is eradicated through expansion for 0.35 and 0.40 mJ/m^2 DMI and collapsed immediately for 0.45 and 0.50 mJ/m^2 DMI.

Figures 4.2a and 4.2b show, respectively, the spin states and the corresponding topological charge variation for J_z = -0.6 x 10^{12} A/m^2. In the case of D_i = 0.30 mJ/m^2, spin reversal formed a stripe-like domain, which is ripped off into a skyrmion and two antiskyrmions. At first, the skyrmion, followed by the antiskyrmions, are eradicated. A skyrmion is formed within the pulse for D_i = 0.35 - 0.50 mJ/m2. Moreover, it is stabilized through breathing mode in the relaxation process for D_i = 0.35 – 0.45 mJ/m^2. That is confirmed by the topological charge at 5ns in Fig. 2b. For 0.50 mJ/m^2 DMI, the skyrmion is annihilated by expanding its core. Figure 4.2c explains the core size variation of a stable skyrmion, and clearly, the skyrmion size increases as the DMI strength increases, as expected due to the role of DMI.

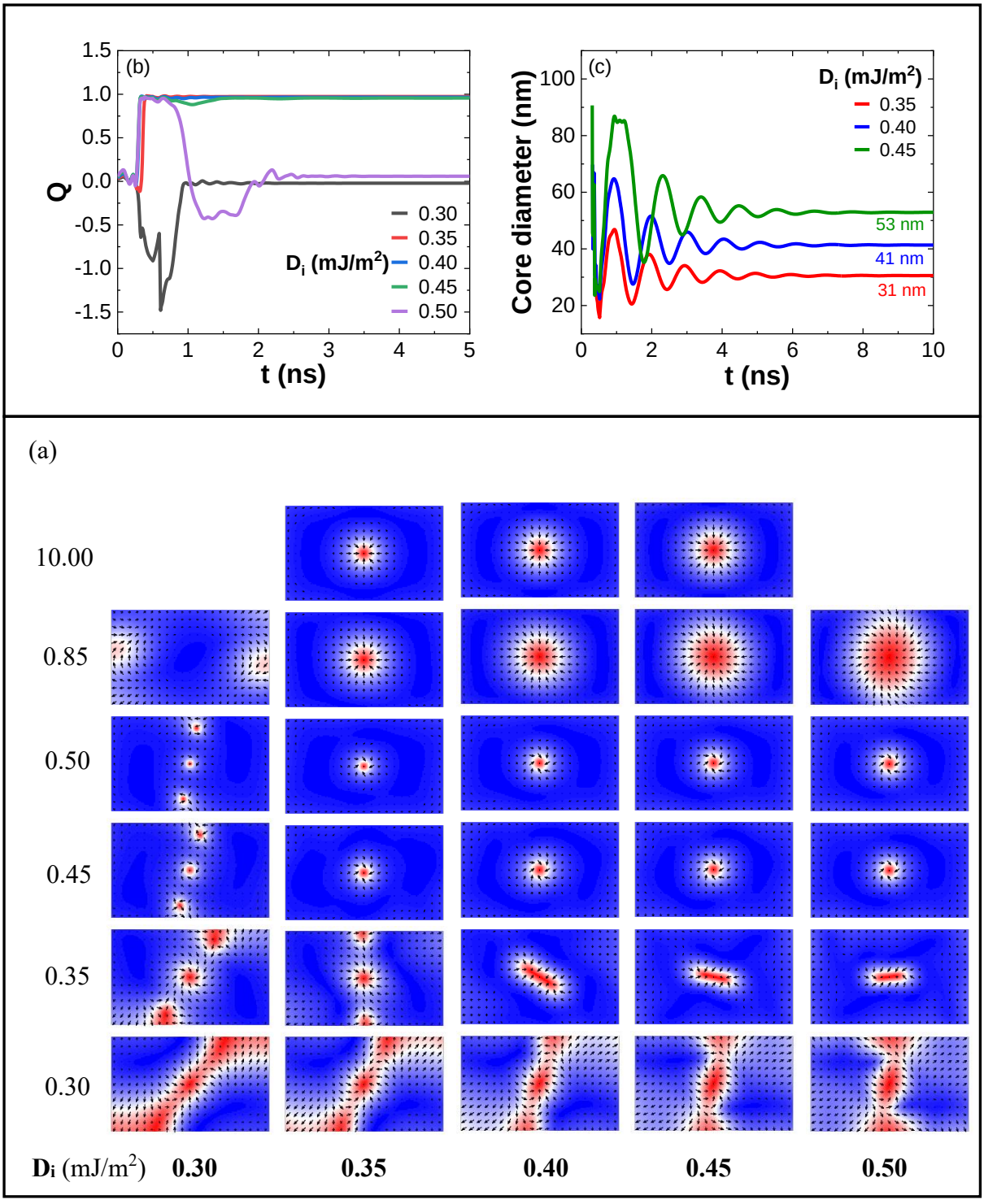

Figure 4.2 Spin states, topological charge Q and the skyrmion core diameter variation for J_z = -0.6 x 10^{12} A/m^2. **(a)** Evolution of stripe-like domain ripped off into a skyrmion and two incomplete antiskyrmions for D_i = 0.30 and 0.35 mJ/m^2. Skyrmion is stabilized to the D_i = 0.35 – 0.45 mJ//m^2. **(b)** The topological charge Q = 1 at 10 ns indicates the stable skyrmion. **(c)** The core diameter variation upto ~ 5 ns indicates the breathing mode, and the skyrmion size increases with DMI strength.

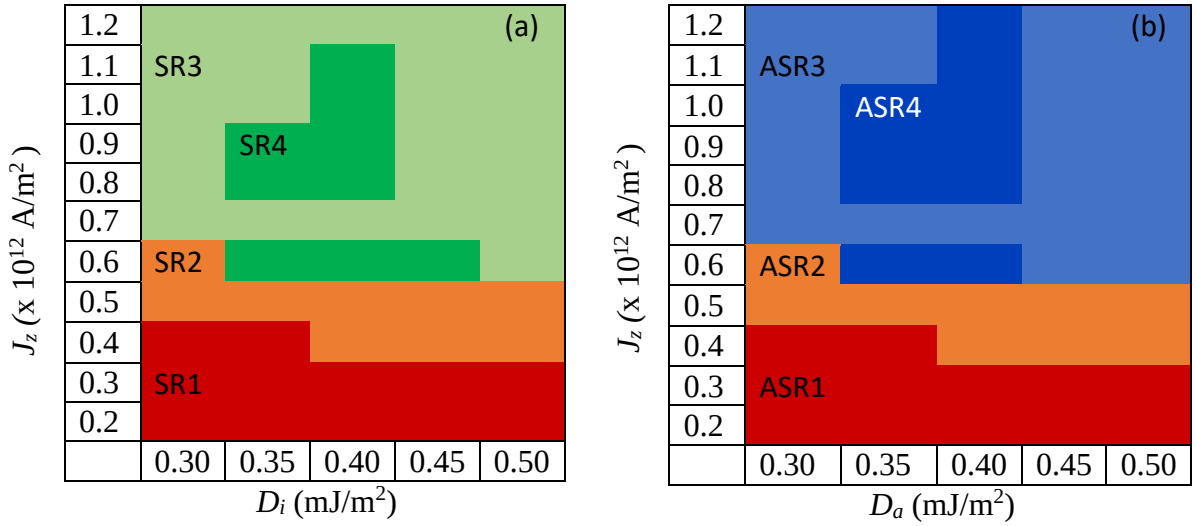

Figure 4.3 The phase diagram of the skyrmion and antiskyrmion formation.
(a) Skyrmion: SR1 is the region of no-skyrmion, SR2 is the region of skyrmion and antiskyrmion evolution, SR3 and SR4 are the unstable and stable regions of skyrmion formation.
(b) Antiskyrmion: ASR1 is the region of no-antiskyrmion, ASR2 is the region of skyrmion and antiskyrmion evolution, ASR3 and ASR4 are the unstable and stable regions of antiskyrmion formation.

The phase diagram of skyrmion formation for the isotropic DMIs from 0.30 to 0.50 mJ/m^2 and different spin-polarized current densities applied for 0.5 ns are shown in Fig. 4.3a. The current densities $J_z \geq$ -0.7 x 10^{12} A/m^2 created a skyrmion for all the DMIs. The skyrmion is destroyed within the current pulse width for D_i = 0.30 mJ/m2 and $J_z \geq$ -0.7 x 10^{12} A/m2. A stable skyrmion is observed for D_i = 0.35 mJ/m^2 at J_z = -0.8 and -0.9 x 10^{12} A/m^2 and for D_i = 0.40 mJ/m^2 from J_z = -0.8 to -1.1 x 10^{12} A/m^2. Above these current densities, the skyrmion is annihilated within the current pulse. In the case of D_i = 0.45 and 0.50 mJ/m^2, the skyrmion is unstable and eradicated through the expansion of the core during the relaxation.

4.2.2 Antiskyrmion

We implemented a modified mumax3 code for anisotropic DMI favouring antiskyrmion formation. The in-plane DMI component magnitudes are assumed to be equal $\left(\|D_x\| = \|D_y\| = \mathrm{D}_a\right)$ to compare the dynamics of skyrmions and antiskyrmions. Isolated antiskyrmion formation for different current densities is similar to the skyrmion formation. Notably, the unstable skyrmion formation is observed for J_z = -0.5 x 10^{12} A/m^2 and for all the anisotropic DMIs is shown in supplementary Fig. 4.4a (The corresponding topological charge variation is shown in supplementary Fig. 4.4b). For or D_a = 0.30 mJ/m^2 and J_z = -0.6 x 10^{12} A/m^2, a stripe-like domain evolved and ripped out into an antiskyrmion and two skyrmions (Fig. 4.5a and b). Under the same material parameters and with an equal magnitude of isotropic and anisotropic forms of DMI, the core size of the antiskyrmion is slightly larger than the skyrmion size (Fig. 4.5c). The phase diagrams of the Skyrmion (Fig. 4.3a) and Antiskyrmion (Fig. 4.3b) show that the formation of a particular chiral spin texture depends on the nature of the DMI. In the regions SR1 and ASR1, the spin texture nucleation is not observed. Merging of magnetization reversal from the corners created an unstable skyrmion and antiskyrmion phase in SR2 and ASR2 regions. Even though skyrmion and antiskyrmion nucleation happen in the respective regions of SR3 and ASR3, they are annihilated by shrinking their size within the current pulse time. In the regions SR4 and ASR4, stable skyrmion and antiskyrmion nucleation is observed, respectively.

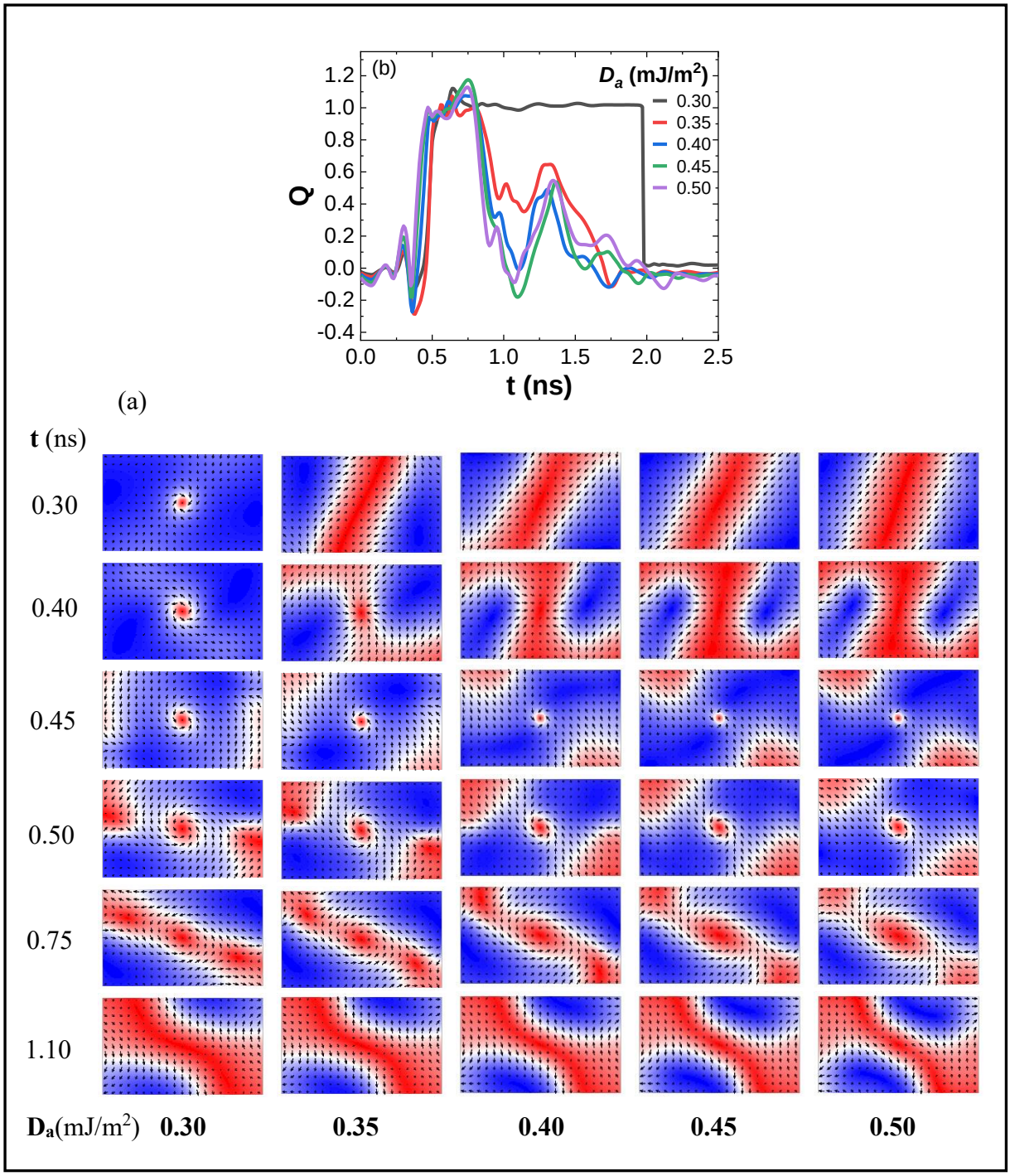

Figure 4.4 Spin states and corresponding topological charge variation for J_z = -0.5 x 10^{12} A/m^2. **(a)** The spin states at different instants for D_a = 0.30 – 0.50 mJ//m^2 show the evolution of skyrmion. **(b)** The topological charge Q = 1 for the corresponding spin states indicates that the spin texture is a skyrmion.

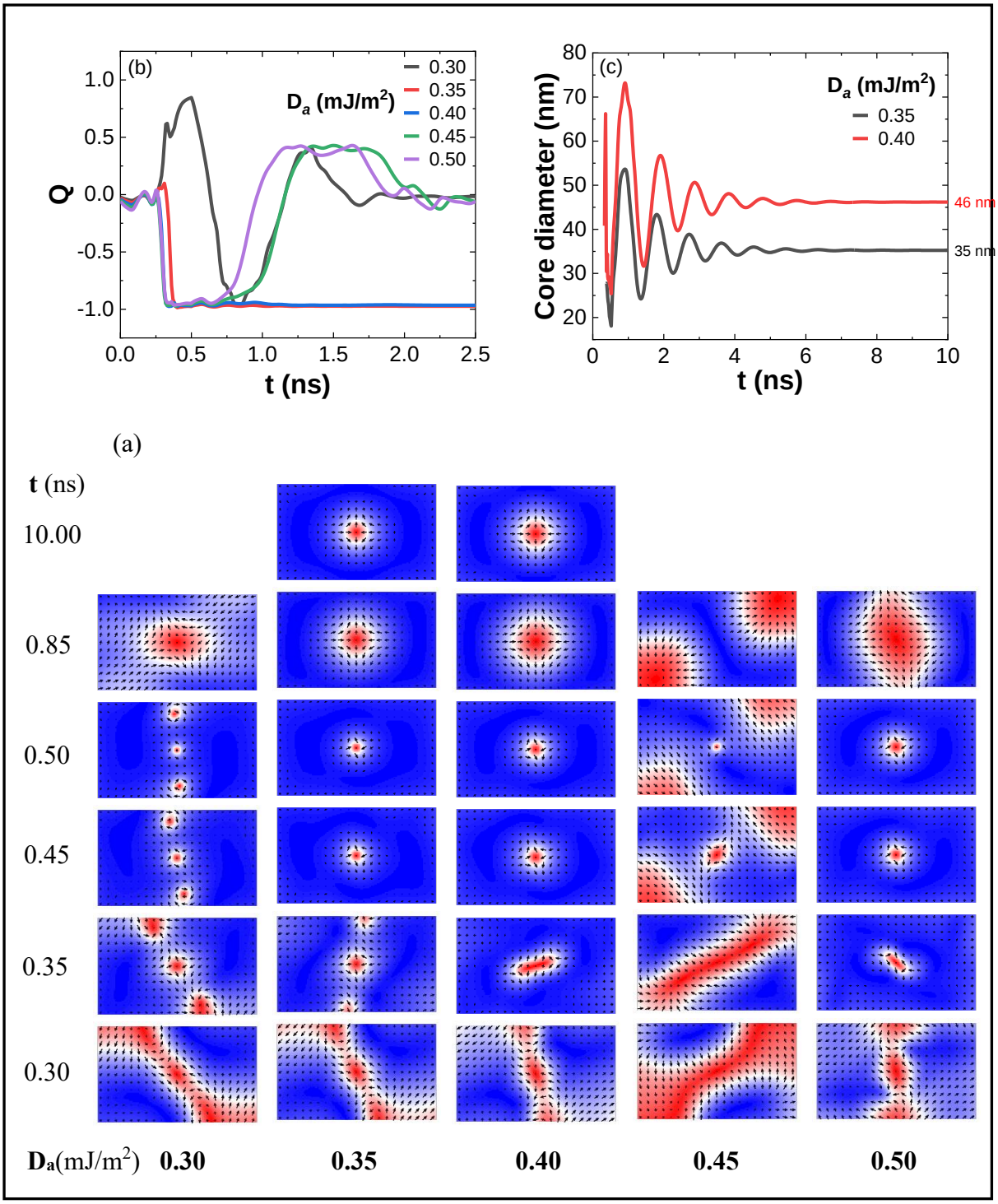

Figure 4.5 Spin states, topological charge Q and the antiskyrmion core diameter variation for J_z = -0.6 x 10^{12} A/m^2. **(a)** Evolution of stripe-like domain is ripped off into an antiskyrmion and two incomplete skyrmions for D_a = 0.30 and 0.35 mJ/m^2. Skyrmion is stabilized for D_a = 0.35 – 0.40 mJ//m^2. **(b)** The topological charge Q = -1 at 10 ns indicates a stable antiskyrmion. **(c)** The core diameter variation up to ~ 5 ns indicates the breathing mode, and the antiskyrmion size increases with DMI strength.

4.3 Dynamics under Perpendicular Sinusoidal Fields

The spin-polarized current nucleated chiral spin textures are stabilized through the breathing mode. Due to that, in this section, we explore the excitation dynamics under ac magnetic fields with isotropic DMI of 0.35 mJ/m^2 for Skyrmion and anisotropic DMI of 0.35 mJ/m^2 for antiskyrmion. Initially, the stability of the spin textures is tested by applying a static uniform magnetic field perpendicular to the system. As the spin direction at the core centre is upwards, the core size is increased for the positive field and decreased for the opposite field. The Skyrmion is stable for the constant field range of -40 to 12 mT, and the antiskyrmion is stable between -52 to 10 mT (Fig. 4.6). Above these high positive fields, the spin texture is unstable because the system width is less than the length of the chiral structure. Under the static perpendicular magnetic field (B_Z), the dynamic modes of the spin textures are computed from their transient response to an applied field in the form $h_z(t) = h_0 \sin(2\pi f_c t)/(2\pi f_c t)$. With 0.1 mT excitation field's amplitude (h_0) and 50 GHz cut-off frequency (f_c), the dynamics are evaluated for 20 ns. Figure 4.7 shows the power spectral density (PSD) calculated for excitation modes by employing the Fast Fourier Transform (FFT) on transient dynamic magnetization. The PSD plot displays four discrete modes (f_1 - f_4), whose frequencies exhibit a linear dependence on the static field.

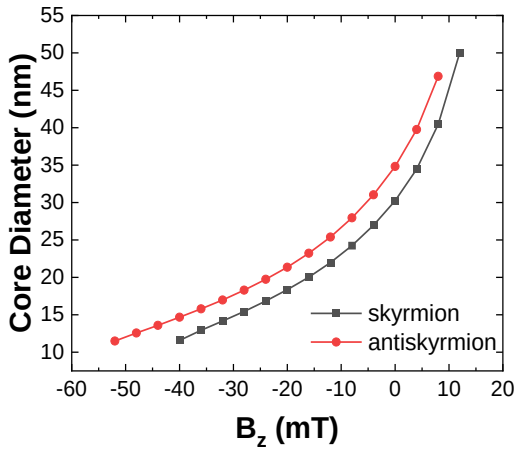

Figure 4.6 Skyrmion and antiskyrmion core diameter under the perpendicular static magnetic field B_z.

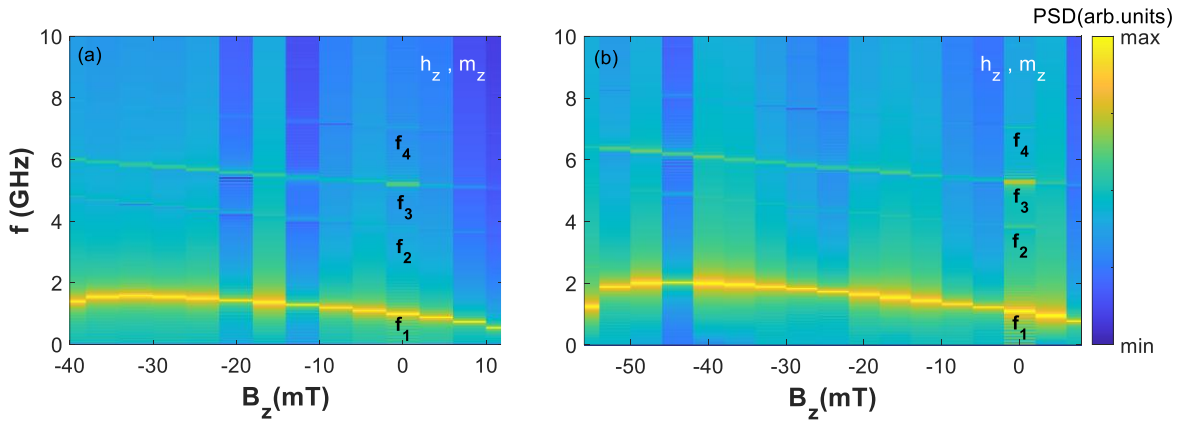

Figure 4.7 Power spectral density color map of excitations for **(a)** skyrmion and **(b)** antiskyrmion under the static field B_z.

Further, the spatial dynamic behaviour of the spin texture is studied using the sinusoidal magnetic field $h_z(t) = h_0 \sin(2\pi f_r t)$ with the resonant mode frequencies obtained earlier. After the field is applied for 20 ns, magnetic states are saved at time intervals of $1/20f_r$ over ten oscillation periods. The spatial fluctuations of the magnetization are calculated using $\delta m(t) = m(0) - m(t)$, where $m(0)$ represents the initial equilibrium state. Fig. 4.8a shows the spatial fluctuations of three magnetization components at one instant for the four resonant mode frequencies under zero static magnetic field of the skyrmion spin texture. Fig. 4.8b represents the m_z component fluctuation ($\delta m_z(t)$) along the x-axis, passing through the centre of the nanostructure for one period of oscillation. The skyrmion and antiskyrmion spin textures show similar dynamic responses to the sinusoidal excitation fields. For mode one (f_1), the spatial fluctuation of the magnetization in Fig. 4.8a and also from the plot of $\delta m_z(x, t)$ in Fig. 4.8b show that the dynamic response is predominately from the spin texture. As the core magnetization expands and contracts, one can conclude that mode one is the breathing mode of the spin texture. The other three modes (f_2 – f_4) are hybrid due to the nanostructure edges excitation with the spin texture's breathing mode, as previously reported by Kim et al. [96]. Mainly, the short sides of the system in mode two (f_2), the corners in mode three (f_3) and the system edge centres in mode four (f_4) are excited along with the breathing mode of the spin texture. We observed similar dynamic excitations for the corresponding modes of the spin texture under the stable static field range (B_z).

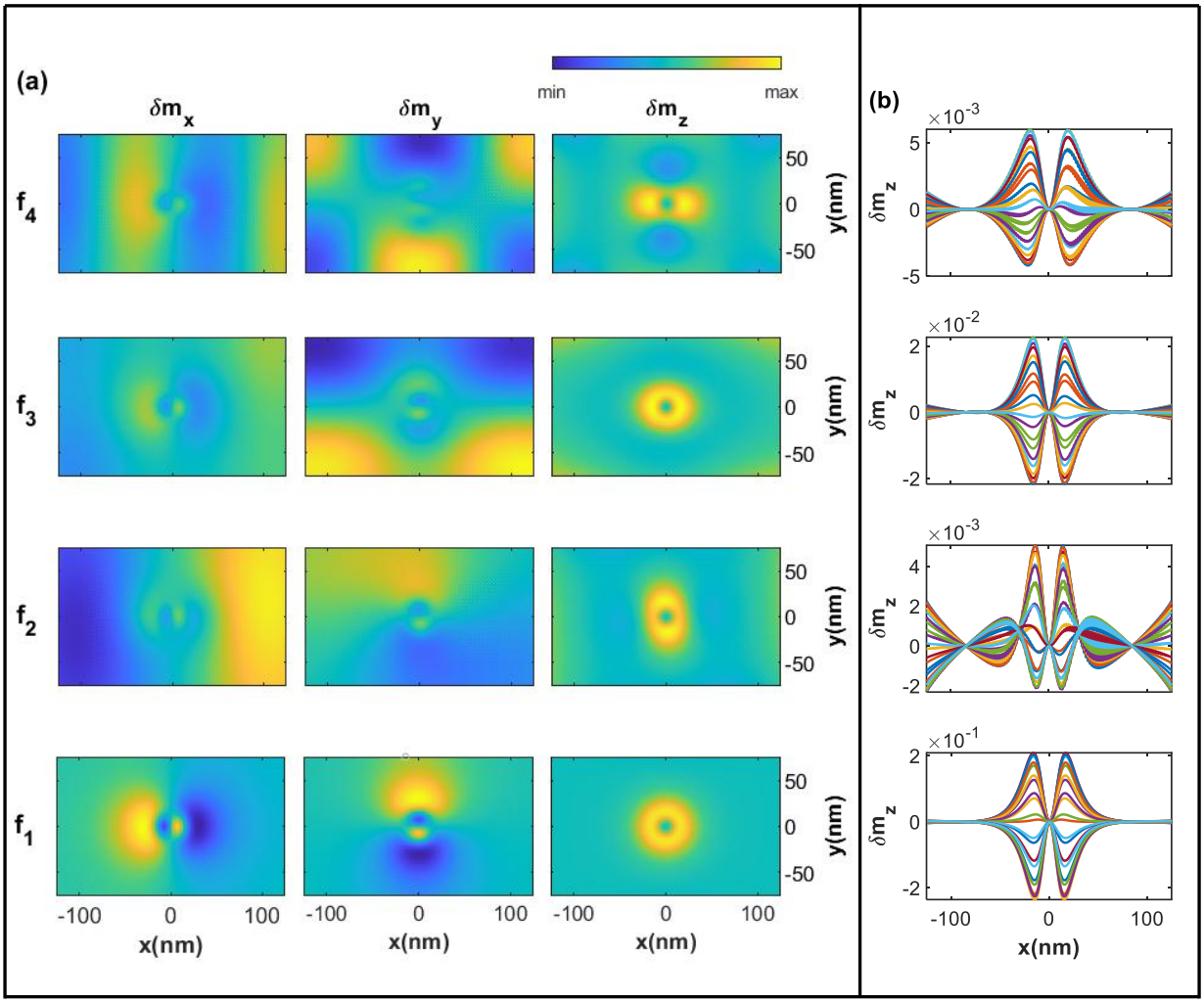

Figure 4.8 Spatial fluctuations in the magnetization of skyrmion spin texture for B_z = 0 mT.
(a) Magnetization components spatial fluctuations for four modes ($f_1 - f_4$).
(b) Variation of δm_z along the x - axis for one period of oscillation.

4.4 Chiral Spin Texture Pair Creation

In the isolated chiral spin texture creation, the magnetization reversal is initiated from the corners of the system, and it happens earlier for a larger value of DMI. It is due to spins tilting more strongly at the nanostructure boundaries for the higher DMI (Fig. 4.9a). To see how the initial spin state configuration affects the chiral spin texture creation, we applied a short positive current pulse $(+\hat{z})$ to saturate the state, and then we applied a negative pulse $(-\hat{z})$. We observed chiral spin texture pair formation for the negative current densities $\geq 2.0 \times 10^{12}$ A/m^2 and the pulse widths < 150 ps. Spin reversal induced a stripe-like domain, which is ripped off into an antiskyrmion and two skyrmions for isotropic DMI. The strip is ripped off into a skyrmion and two antiskyrmions for anisotropic DMI. In the case of isotropic DMI, antiskyrmion annihilated immediately. The skyrmion pair stabilized in some cases during the relaxation (Fig. 4.9b), and the behaviour is opposite to the anisotropic DMI.

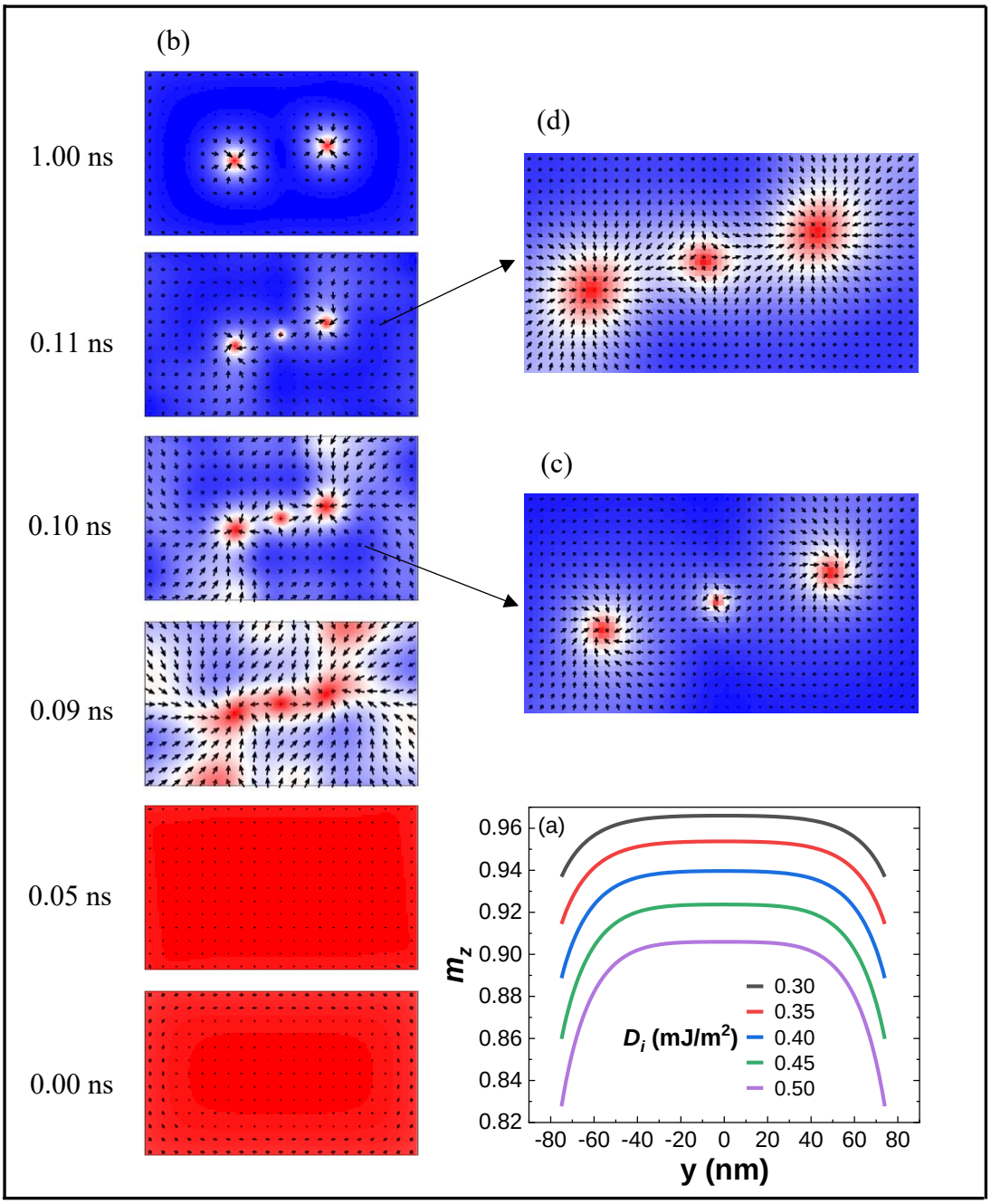

Figure 4.9 (a) The magnetization component m_z at the boundary edges along the width of the nanostructure for the different DMI values. **(b)** Spin states of skyrmion pair creation with an asymmetric current pulse for D_i = 0.35 mJ/m^2: J_z = 3.0 x 10^{12} A/m^2 applied for 50 ps ($t_{p)}$ and J_z = -3.0 x 10^{12} A/m^2 applied for 70 ps (t_n). **(c)** and **(d)** are zooms of the spin states at 0.10 and 0.11 ns.

Figure 4.10 shows the skyrmion pair dynamics for 10 and 50 ps positive pulse (t_p) and 82 ps negative pulse (t_n) with a current density of 3.0 x 10^{12} A/m^2 and D_i = 0.35 mJ/m^2. Once the current pulse is off, due to repulsive interaction, the skyrmion pair moved away from each other in a gyrotropic path (Fig. 4.10a and c) by showing a breathing mode of nearly 5 ns (Fig. 4.10b and d). The skyrmion pair annihilated at the edges for a 10 ps positive pulse (t_p), and for 50 ps it is stabilized. We assign this behaviour to the repulsive interaction, which depends on the initial separation between the skyrmion pair (r_i) – 76 nm for 10 ps and 87 nm for 50 ps.

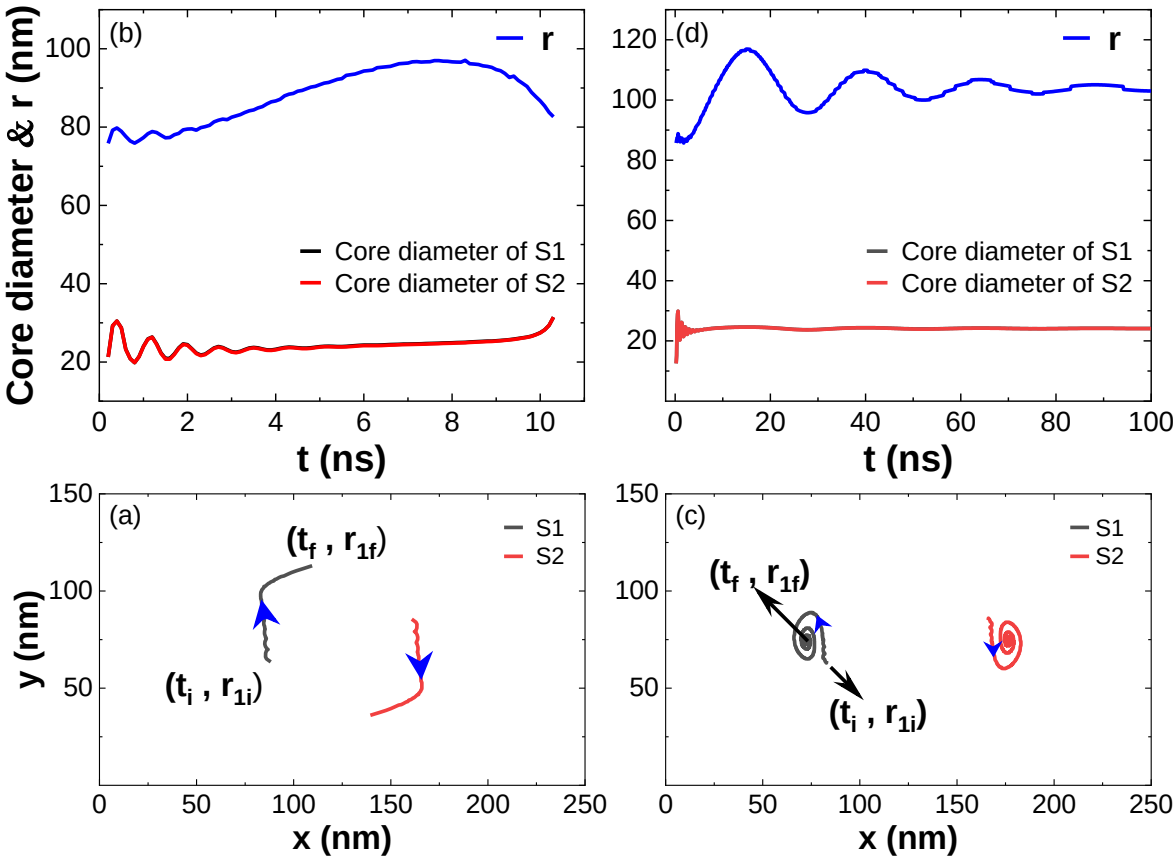

Figure 4.10 Skyrmion pair dynamics in the relaxation for the different positive current pulse widths. (a) and (b) t_p = 10 ps. (c) and (d) t_p = 50 ps. S1: Skyrmion 1 and S2: Skyrmion 2. **r** is the separation distance between the skyrmions S1 and S2. $\mathbf{r_{1i}}$ and $\mathbf{r_{1f}}$, indicate the initial and final positions of skyrmion 1 (S1).

As similar behaviour in the creation of skyrmion pair and antiskyrmion pair are observed, further studies are carried out for fixed isotropic DMI of 0.35 mJ/m^2 for the positive current densities from 1.0 to 5.0 x 10^{12} A/m^2 (+J_z) applied for 10 - 90 ps (t_p), and negative current densities from 2.0 to 4.0 x 10^{12} A/m^2 (-J_z) applied for 40 – 150 ps (t_n). Figs. 4.11a, b, and c show the minimum and maximum negative pulse time (t_n) dependence on the positive current density (+J_z) and its pulse (t_p) for the skyrmion pair formation respectively for 2.0, 3.0 and 4.0 (x 10^{12}) A/m^2 negative current densities. The minimum negative current pulse time (min. t_n: hollow points in Figs. 4.11a, b and c) required for observing the skyrmion pair decreases with increasing positive current density (+J_z) and negative current density (-J_z). The maximum negative current pulse time (max. t_n: solid points in Figs. 4.11a, b and c) is also reduced, except for the case of negative current density 2 x 10^{12} A/m^2 (Fig. 4.11a); this could be due to the strength of the spin transfer torque increasing with the current density. The positive current density (+J_z) applied above 10 ps (t_p) seems to saturate the free 'layer's initial magnetization state. The minimum and maximum negative current pulse width (t_n) saturates for the $t_p > 10$ ps as positive and negative current densities increase. The initial separation of the skyrmion pair increased with positive current density and pulse, as shown in Figures 4.11d, e, and f. We observed a minimum separation of 78 nm between the skyrmions below which the skyrmion pair got annihilated at the edges. The above results were carried out for a zero delay between the positive and negative current pulse, and even when it was introduced a delay of 10 ps, a stable pair of spin textures was created.

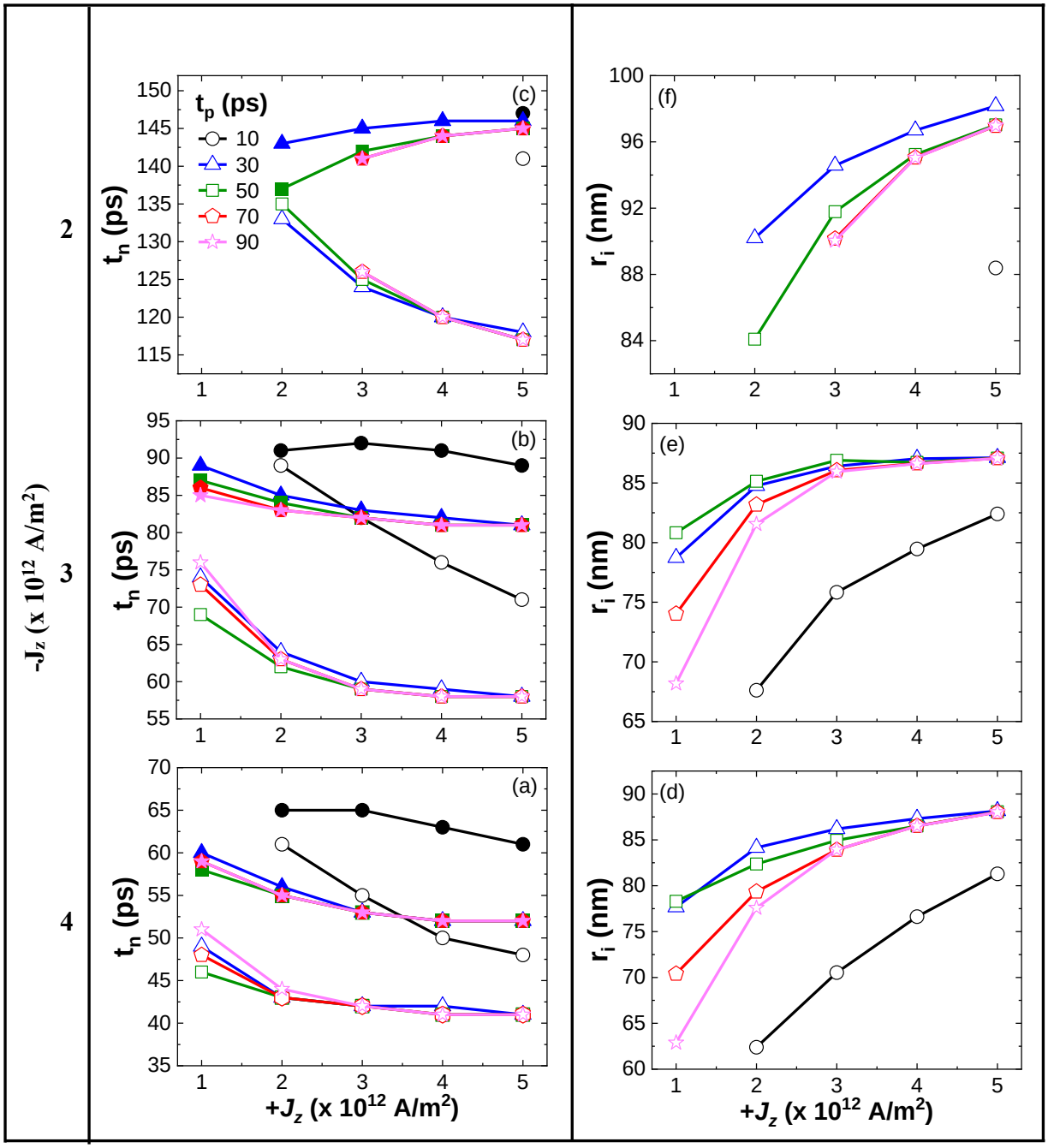

Figure 4.11 (a), (b) and (c) show the negative pulse time (t_n) dependence on the positive and negative current densities, and positive pulse width (t_p) for the skyrmion pair formation. Hollow points indicate minimum t_n and solid points indicate maximum t_n. (d), (e) and (f) show the initial separation between the skyrmion pair dependence on the positive current density ($+J_z$) and its pulse time (t_n). The initial separation is same for the different negative pulse times (t_n) under the fixed positive and negative current density and positive pulse time (t_p).

4.5 Skyrmion – Skyrmion Interaction

To understand the interaction between the skyrmion pair more clearly, we used the Thiele approach to evaluate the force of repulsion exerted by the skyrmions on each other. The position of the two skyrmions is defined as $\boldsymbol{r_1} = (x_1, y_1, 0)$ and $\boldsymbol{r_2} = (x_2, y_2, 0)$ and their speeds $\boldsymbol{v_1} = (v_{x,1}, v_{y,1}, 0)$ and $\boldsymbol{v_2} = (v_{x,2}, v_{y,2}, 0)$. The force can be supposed to be radial and depend only on the distance between the skyrmions $r = |\boldsymbol{r_1} - \boldsymbol{r_2}|$, like a central force. Then, the force will have opposite directions on each Skyrmion and will have the form $\boldsymbol{F_1} = f(r)\hat{\boldsymbol{r}}$ and $\boldsymbol{F_2} = -f(r)\hat{\boldsymbol{r}}$, where $\hat{\boldsymbol{r}} = (\boldsymbol{r_1} - \boldsymbol{r_2})/r$ is the unit vector pointing from skyrmion-1 to skyrmion-2. One can establish a Thiele equation for each Skyrmion.

In general, $\boldsymbol{G} \times \boldsymbol{v} - \alpha \widetilde{\mathcal{D}} \boldsymbol{v} = \boldsymbol{F}$

where $\boldsymbol{G} = \frac{-4\pi Q M_s l}{\gamma} \hat{\boldsymbol{k}}$ is the gyrotropic vector and $\widetilde{\mathcal{D}} \equiv D_{ii}$ is the diagonal component of the dissipative tensor. $D_{ij} = \frac{M_s}{\gamma} \int \frac{\partial m}{\partial x_i} \frac{\partial m}{\partial x_j} dV$ with x_i representing the cartesian coordinates, we always have $D_{xx} = D_{yy} = D$ and $D_{xy} = D_{yx} = 0$ for the skyrmion profile. The Thiele equation for the coupled skyrmions can be rewritten as $\boldsymbol{G} \times \Delta\boldsymbol{v} - \alpha D \Delta\boldsymbol{v} = 2\boldsymbol{F}$. Where $\Delta\boldsymbol{v} = (\Delta\boldsymbol{v_x}, \Delta\boldsymbol{v_y}, 0)$ is the difference in velocities between two skyrmions. We used an FFT filter to smoothen the noisy variation of the skyrmions' position, and from that, we obtained the velocities. From the fitting of the velocities, one can obtain the value of the force $f(r)$.

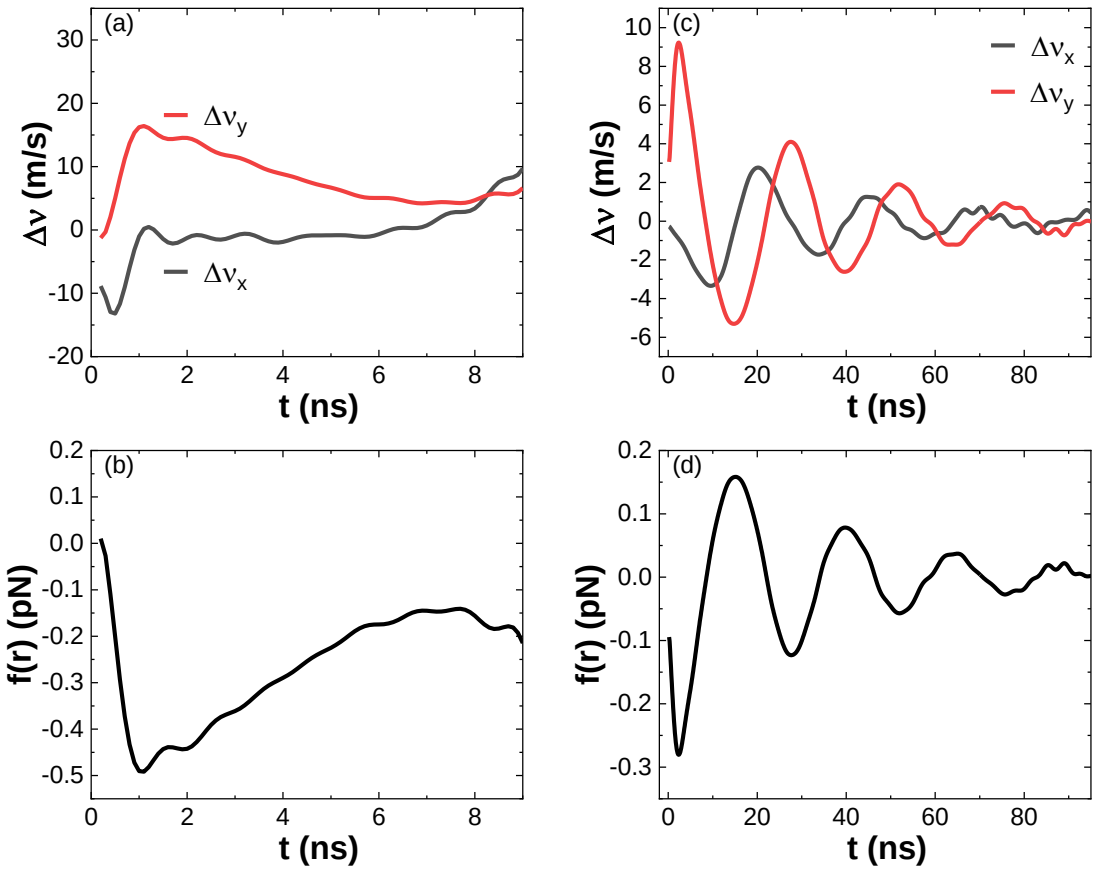

Figure 4.12 The difference in velocities and interaction force variation to the unstable and stable skyrmion pair. **(a)** and **(b)** unstable skyrmion pair, **(c)** and **(d)** stable skyrmion pair (to the dynamics explained in Fig. 4.10).

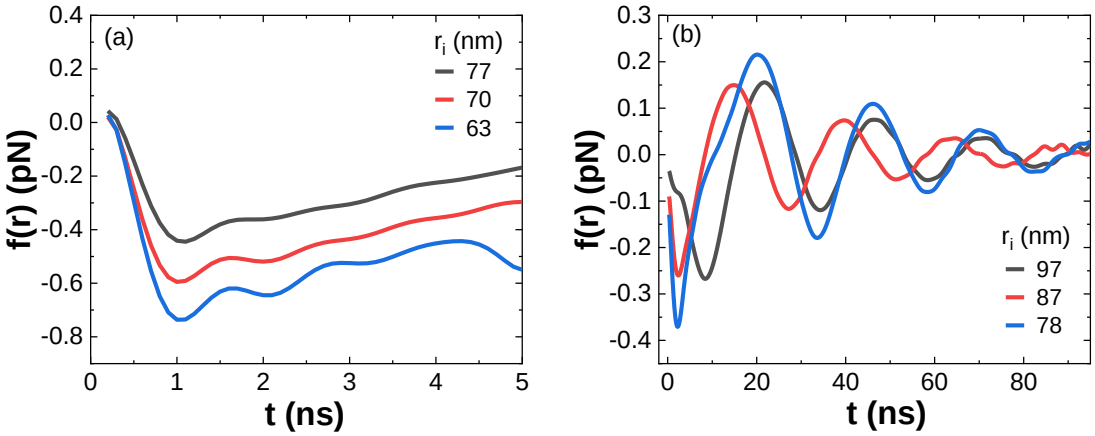

Figure 4.13 Interaction force variation to the different initial distances between the skyrmion pair. **(a)** Unstable skyrmion pair. **(b)** Stable skyrmion pair.

For the skyrmion pair dynamics explained in Fig. 4.10, the $\Delta \boldsymbol{v}$ and $f(r)$ variations are shown in Fig. 4.12. As the skyrmions in the pair are equal, the force is repulsive and increases up to 1 ns for both unstable and stable creation. The dynamics induced by the repulsion force are heavily damped for the unstable pair and lightly damped for the stable pair. In the case of the unstable pair, due to less initial separation (76 nm), the force of repulsion is larger, leading to the annihilation of the skyrmion pair. It is clear from Fig. 4.13 that as the initial separation increases, the interaction force is reduced, and above the threshold separation of 78 nm, the skyrmion pair is stabilized.

4.6 Summary

This study demonstrates the creation of stable chiral spin textures in a rectangular nanostructure using spin-polarized currents. Different types of DMI stabilize different textures, and their size grows with increasing DMI strength. Spin texture stability relies on current density, pulse duration, and DMI strength. We investigated the dynamics of spin textures under perpendicular sinusoidal fields and observed different modes. We also explored the creation and interaction of stable skyrmion pairs, finding a critical separation distance for their stability.

CHAPTER 5

Dynamics in a Circular Nanostructure

- Skyrmion is a flexible spin texture and can be created by flipping spins from the centre or periphery of the system.

In our previous research, we discovered that under the influence of higher spin-polarized currents, a square nanostructure forms a lattice of four skyrmions, while a rectangular nanostructure forms a pair of skyrmions. Continuing from our previous findings, we conducted simulations on a circular nanostructure to investigate how the structural characteristics impact the formation of a skyrmion lattice.

The skyrmion spin texture is created in two different ways. One way is reversing the spins at the core and the other through the edges of the nanostructure. This study has been carried out with CoPd as a free layer in a circular spin valve nanostructure and for the three different fixed layer polarizations: (i) Perpendicular, (ii) Diverging vortex, and (iii) Circular vortex. The formation of a stable skyrmion in the free layer is initiated by magnetization reversal from the edges of the nanostructure, but this occurs only when the fixed layer polarization is perpendicular to the plane of the nanostructure. For spin reversal at the centre of the free layer, the stable skyrmion formation occurred exclusively with diverging and circular vortex fixed layer configurations.

5.1 Model and Simulations

Numerical simulations are performed on a circular spin valve nanostructure using a mumax3 micromagnetic simulator. The structure comprises a free-layer/spacer/fixed-layer (Fig. 5.1a). Initial magnetization of the free layer is considered along the +z direction, and the skyrmion is created using spin-polarized currents under different magnetic polarizations of the fixed layer (Figs. 5.1b and c). The free layer magnetization dynamics are studied with the LLGS equation.

Simulations are employed on a 200 nm diameter free layer with discretized cell sizes of 1 nm x 1nm x 1nm. The material parameters are considered from a Co/Pd multilayer system [94], which has an interfacial DMI required to create skyrmion spin texture. We considered an exchange constant of A = 15 pJ/m, a saturation magnetization of M_s = 280 kA/m, a uniaxial anisotropy of K_u = 0.06 MJ/m^3, an interfacial DMI of D = 0.30 – 0.50 mJ/m^2, a Gilbert damping constant of α = 0.1, spin polarization of P = 0.4 and $\varepsilon' = 0$ for stable skyrmion creation. We used α = 0.001 for the dynamic modes of skyrmion under perpendicular sinusoidal fields. The following sections will investigate the formation of skyrmion spin texture in two ways: one involving magnetization reversal from the edges of the nanostructure and the other from its centre. For stable skyrmion spin texture creation via the spin reversal from the edges of the nanostructure, the spin-polarized current densities of range 0.1 x 10^{12} to 5.0 x 10^{12} A/m^2 are employed in a negative z-direction ($-J_z$). Conversely, for the spin reversal at the centre of the nanostructure with nano contacts of 10 to 40 nm, the spin-polarized current densities of range 1.0 x 10^{15} to 5.0 x 10^{15} A/m^2 are applied in a positive z-direction ($+J_z$). The pulse widths (t_w) of $\leq$ 0.5 ns are used in these two cases.

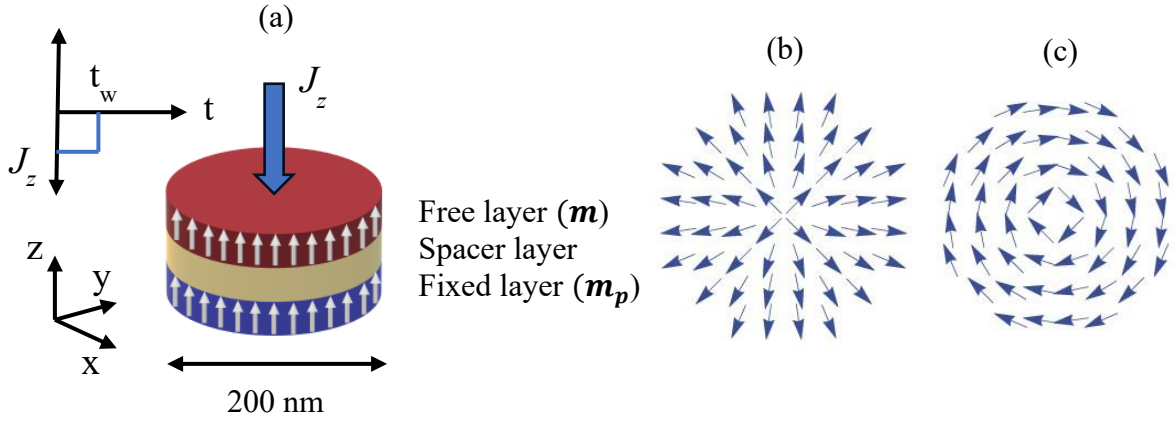

Figure 5.1 (a) A circular spin valve nanostructure with initial magnetization directions in the free and fixed layers. The blue arrow over the spin valve nanostructure represents the spin-polarized current density applied along negative z direction. And t_w indicates its pulse width. (b) and (c) represent the fixed layer diverging and clockwise polarization orientations.

5.2 Perpendicular Fixed Layer Polarization

Initially, the system is relaxed with uniformly oriented and perpendicular free and fixed layer magnetizations. Then, a spin-polarized current density is applied to the entire nanostructure for 0.5 ns along a negative z direction. The current density (J_z) up to -0.3 x

10^{12} A/m^2 didn't induce the magnetization reversal for any DMI values. For J_z = -0.4 x 10^{12} A/m^2, D = 0.30 to 0.40 mJ/m^2, magnetization reversal is initiated from the edges of the nanostructure. However, this reversal is annihilated later due to the short current pulse width (0.5 ns). For D = 0.45 and 0.50 mJ/m^2, the spin reversal from the edges leads to the formation of a skyrmion spin texture within the duration of the current pulse (Fig. 5.2). After the current pulse is off, the spin texture is stabilized through the breathing mode.

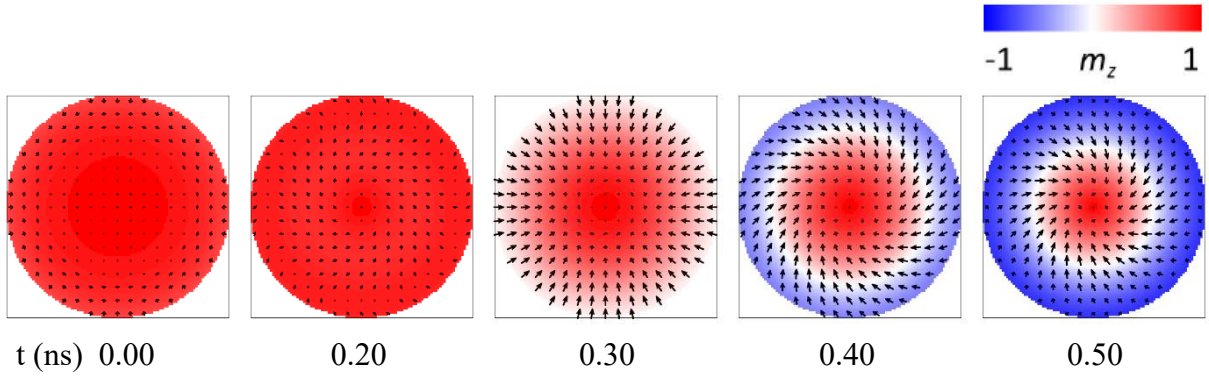

Figure 5.2 Skyrmion formation through the magnetization reversal from the edges of the nanostructure for D = 0.45 mJ/m^2. The respective spin states corresponding to the simulation time are shown for a spin polarized current density of J_z = -0.4 x 10^{12} A/m^2 and the pulse width 0.5 ns.

Figures 5.3a, b and c show the spin transfer torque z component magnitude, topological charge and skyrmion core size variation to the current density -0.5 x 10^{12} A/m^2 for all the DMI values. The spin reversal created a stable skyrmion in all the cases. The spin transfer torque behaviour is similar for all the DMIs, and its strength increases with the DMI strength (Fig. 5.3a). The topological charge reaches 1 at around 0.3 ns for all the DMIs (5.3b), indicating that a skyrmion formation occurred below the current pulse width (0.5 ns). Until the duration of the current pulse, the skyrmion core size shrinks. After the current pulse is off, it exhibits a breathing mode for nearly up to 5 ns and eventually reaches a stabilized state (Fig. 5.3c). The skyrmion core size increases as the strength of the DMI increases. Even though the strength of the spin transfer torque increases for the current density J_z = -0.6 x 10^{12} A/m^2, it decreases with the DMI strength (Fig. 5.3d). In this case, the magnetization reversal initiated from near the boundary to form a skyrmion for all the DMI values (Fig. 5.3e). However, the skyrmion is annihilated within the current pulse width. That could be due to the field-like torque from spin-polarized currents, and its strength increases as the DMI value rises (Fig. 5.3f).

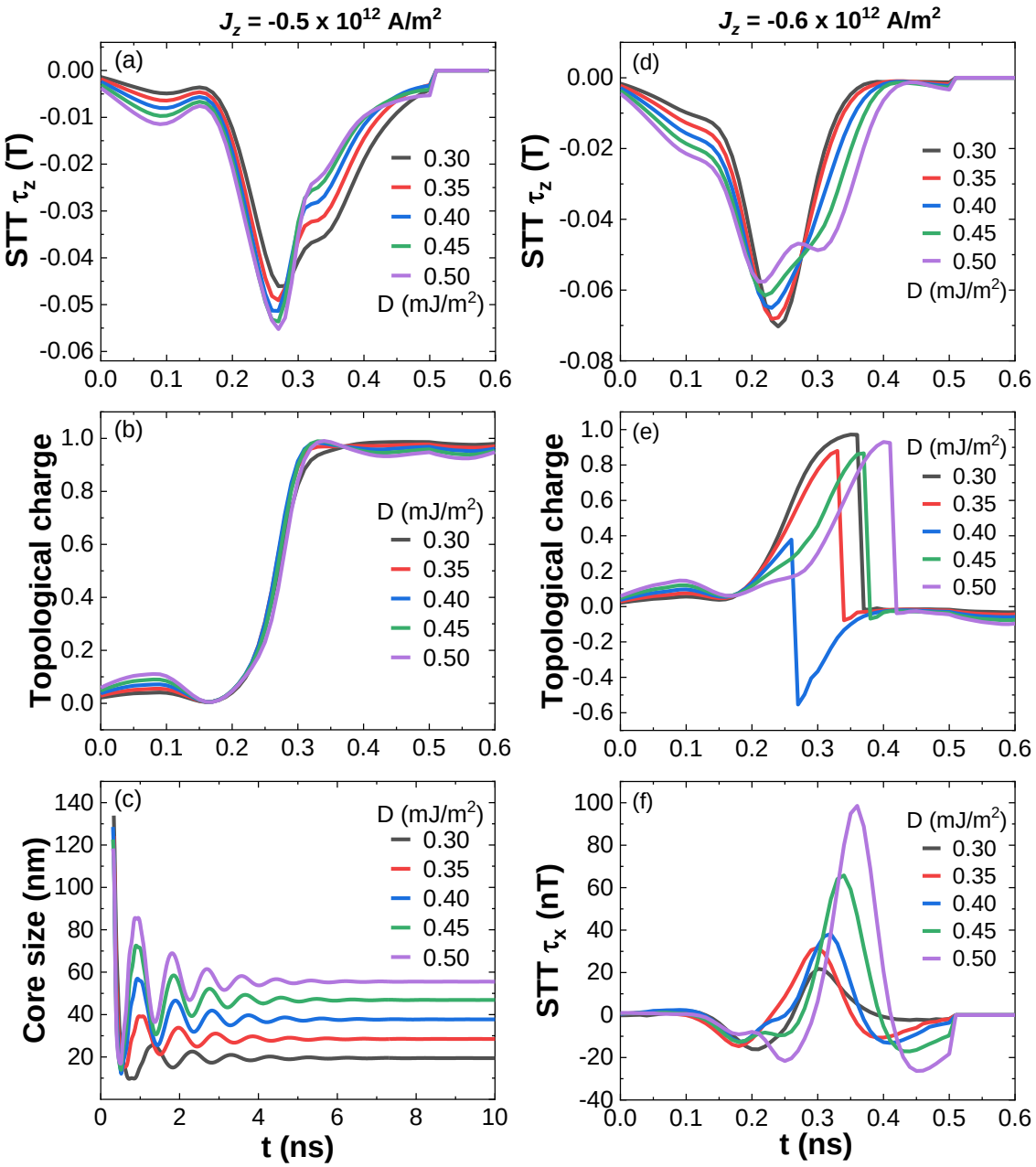

Figure 5.3 (a), (b), and (c) represent spin transfer torque z component, topological charge and skyrmion core size variation versus simulation time for J_z = -0.5 x 10^{12} A/m^2. (d), (e), and (f) represent spin transfer torque z component, topological charge and spin transfer torque x component variation versus simulation time for J_z = -0.6 x 10^{12} A/m^2.

Above J_z = -0.7 x 10^{12} A/m^2, skyrmion formation occurred across all the DMI values. In some cases, it is stabilized after the current is off, while in others, it is annihilated through core compression due to the longer pulse width (0.5 ns). Fig. 5.4a explains the phase diagram of the skyrmion formation for the DMI values 0.30 – 0.50 mJ/m^2 to the different current densities applied for 0.5 ns. SR1 is no skyrmion formation region, SR2 is the region of unstable skyrmion formation, and SR3 is the stable skyrmion region. It is clear from figures 5.4b and 5.4c that for a fixed DMI (0.40 mJ/m^2), when current density increases, the strength of the spin transfer torque increases and consequently, the skyrmion formation happens earlier as expected. Also, the core size of the skyrmion doesn't depend on the current density strength (Fig. 5.4d).

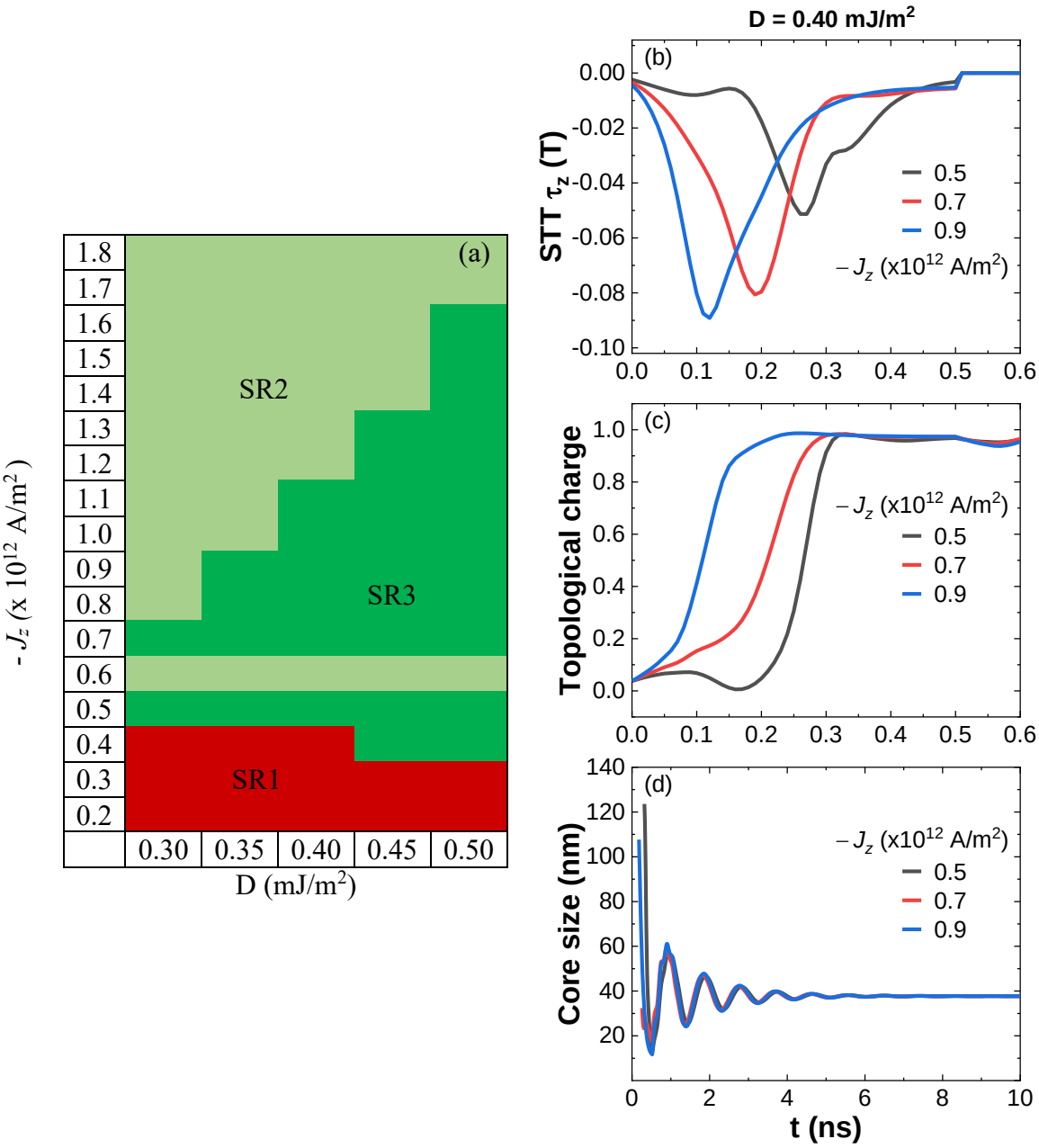

Figure 5.4 **(a)** Phase diagram of the skyrmion formation for different DMIs and current densities applied for 0.5 ns. SR1 is no skyrmion region, SR2 is an unstable skyrmion region, and SR3 is a stable skyrmion region. **(b)**, **(c)**, and **(d)** represent the spin transfer torque, topological charge and skyrmion core size variation versus simulation time for the DMI 0.40 mJ/m^2.

5.3 Fixed Layer Vortex Polarizations

To create a skyrmion using an alternate approach, we applied a spin-polarized current through the nano contacts positioned at the core of the nanostructure. This section used circular nano contacts of 10 to 50 nm diameters, spin-polarized current densities of 1 x 10^{15} to 8 x 10^{15} A/m^2 and pulse widths of 0.1 to 0.5 ns for the DMI of 0.40 mJ/m^2. Our studies focused on the same free layers' magnetization configuration (uniform and perpendicular to the film plane), as described in the previous section and for the three fixed layer polarizations: perpendicular, diverging, and circular vortex. Skyrmion creation only happened for the diverging and circular vortex fixed layer polarizations. Either for diverging or circular vortex polarization, the stable skyrmion nucleation started from the current density 2 x 10^{15} A/m^2 and with a 20 nm nano contact (Fig. 5.5). In the case of a diverging vortex above the current density 2 x 10^{15} A/m^2, stable skyrmion formation is independent of the current pulse duration and the nano contact width.

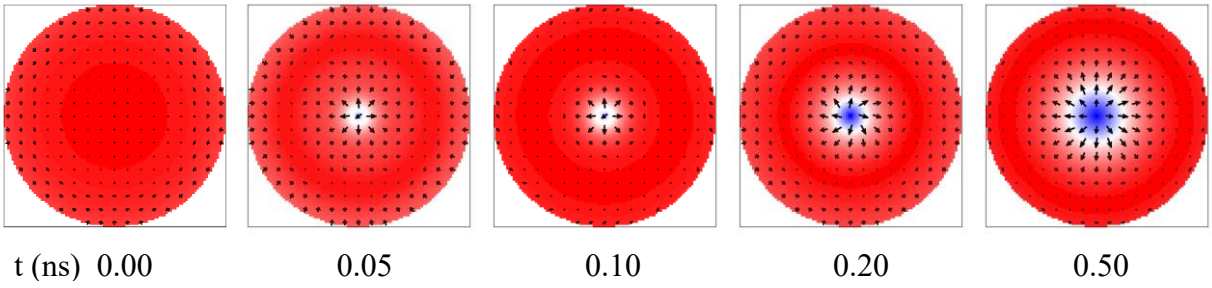

Figure 5.5 Skyrmion nucleation through the spin reversal at the core of the nanostructure, with a diverging vortex polarization for D = 0.40 mJ/m^2. The respective spin states corresponding to the simulation time are shown for a spin polarized current density of J_z = 2.0 x 10^{15} A/m^2 passing through a 20 nm nano contact for a current pulse duration of 0.1 ns.

However, in the case of a circular vortex, for the current density of 2 x 10^{15} A/m^2, stable skyrmion formation occurs with a minimum current pulse duration of 0.2 ns for the nano contact widths 30 and 40 nm. Conversely, for 50 nm contact width, a stable skyrmion does not form regardless of the duration of the current pulse. This could be due to the behaviour of spin transfer torque arising from the different fixed layer polarizations. Figure 5.6 shows the spin transfer torque z component, topological charge and skyrmion core size variation for J_z = 2.0 x 10^{15} A/m^2 to the fixed current pulse width 0.2 ns and fixed nano contact width 20 nm. The STT behaviour is complex, and its strength increases with the expansion of nano contact width (Fig. 5.6a and 5.6d). The topological charge -1 indicates the spin texture is a skyrmion with

core spin orientation downward (Figs. 5.6b and 5.6e). Similar to the preceding section, once the current pulse is off, stabilization of the skyrmion occurs through the breathing mode in the relaxation process, and its size is independent of the nano contact width and the current pulse duration (Figs. 5.6c and 5.6f).

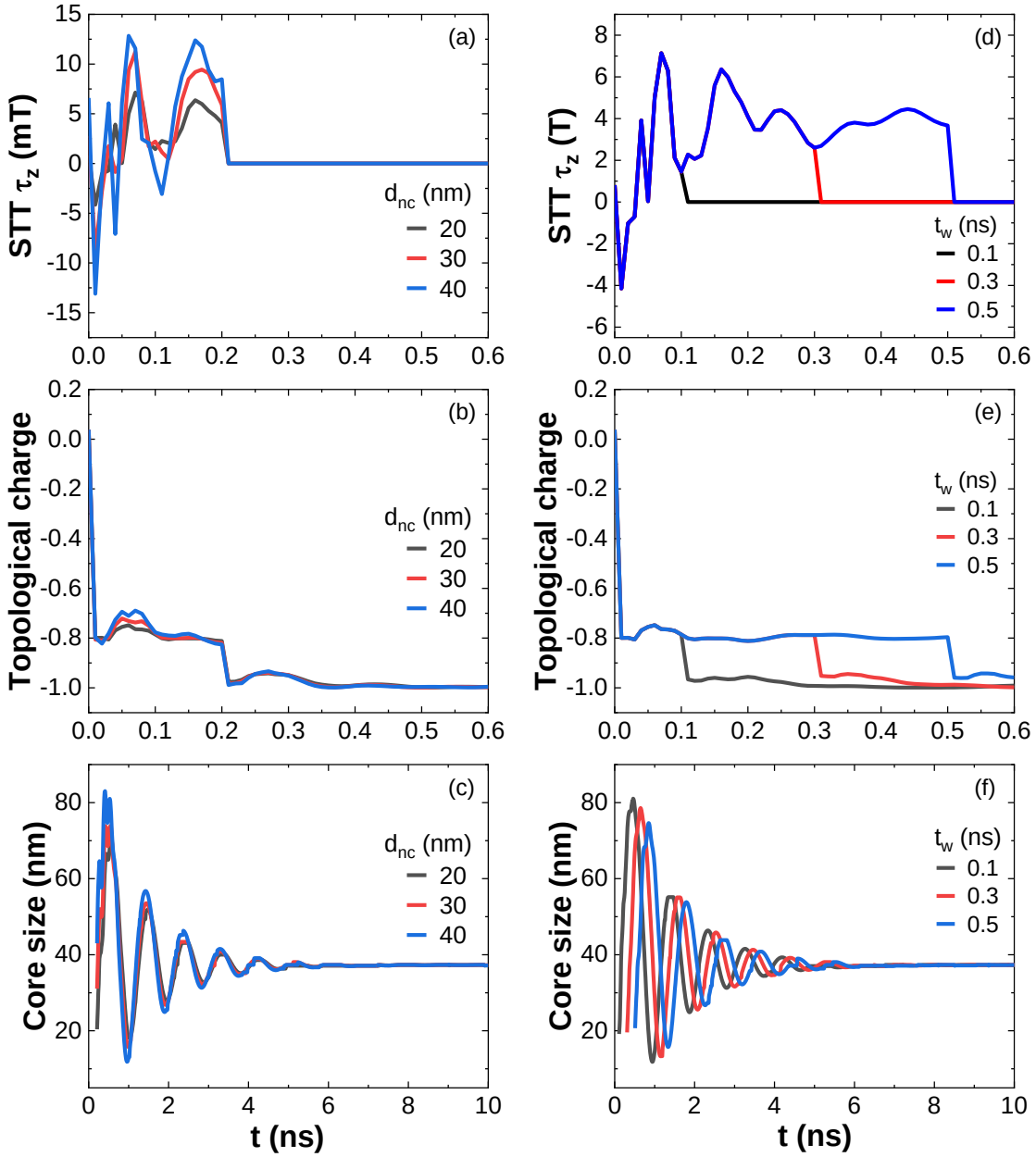

Figure 5.6 Spin transfer torque z component, topological charge and skyrmion core size variation versus simulation time for J_z = 2.0 x 10^{15} A/m^2. d_{nc}: nano contact diameter, t_w: current pulse width. **(a)**, **(b)**, and **(c)** are for fixed current pulse width 0.2 ns. **(d)**, **(e)**, and **(f)** are for fixed contact width 20 nm.

5.4 Skyrmion Dynamics under Alternating Fields

Due to the stabilization of skyrmion by the breathing mode, this section investigates the dynamics of its excitations under alternating magnetic fields for the DMI 0.40 mJ/m^2 under the perpendicular and diverging vortex fixed layer orientations. At first, the skyrmion stability is examined through the uniform static magnetic field applied perpendicular to the system. When a skyrmion is formed by the reversal of magnetization from the boundaries of the nanostructure with a perpendicular fixed layer polarization, its core spin is upward. Consequently, the core size increases for positive fields and decreases for negative fields (Fig. 5.7, -a). On the other hand, when a skyrmion is nucleated by reversing the core spin at the system's centre with a diverging vortex fixed layer orientation, the core spin is downward. Here, the core size decreases for positive fields and increases for negative fields (Fig. 5.7, -b). The skyrmion dynamic modes are determined under a static perpendicular magnetic field (B_z) by analyzing their transient response to a field of the form $h_z(t) = h_0 \sin(2\pi f_c t)/(2\pi f_c t)$. Using an excitation field amplitude (h_0) of 0.1 mT and a 50 GHz cut-off frequency (f_c), the system's dynamics are studied over a period of 20 ns. Figure 5.8 illustrates the power spectral density (PSD) obtained by applying the Fast Fourier Transform (FFT) to the transient dynamic magnetization. The PSD plot reveals two distinct modes (f1 and f2) whose frequencies exhibit a linear correlation with the static field.

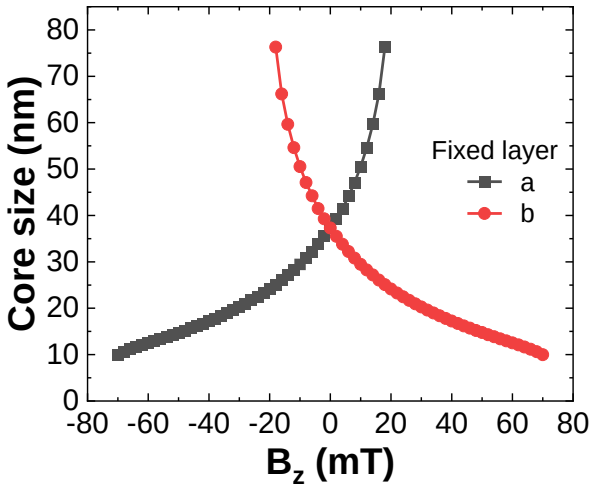

Figure 5.7 Skyrmion core diameter under the uniform perpendicular static magnetic field B_z, a - perpendicular and b - diverging vortex fixed layer orientations.

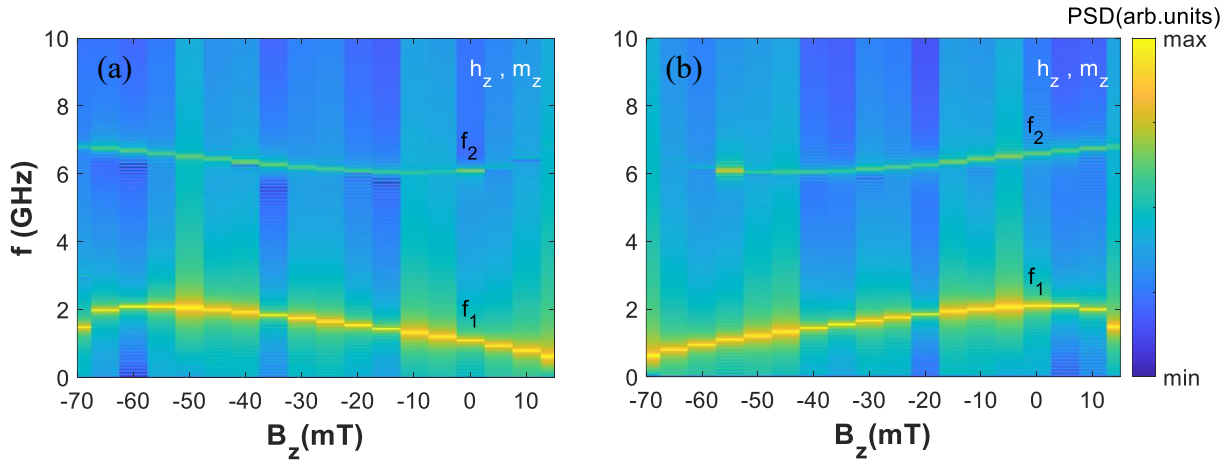

Figure 5.8 Power spectral density (PSD) colour map of excitations of a skyrmion under the static field B_z for **(a)** perpendicular and **(b)** diverging vortex fixed layer orientations.

Furthermore, we investigate the spatial dynamic behaviour of the spin texture by subjecting it to a sinusoidal magnetic field $h_z(t) = h_0 \sin(2\pi f_r t)$ with the resonant mode frequencies determined earlier. After applying the field for 20 ns, magnetic states are recorded at intervals of $1/20f_r$ over ten oscillation periods. To assess the spatial variations in magnetization, we calculate $\delta m(t) = m(0) - m(t)$, where $m(0)$ denotes the initial state. Figure 5.9a depicts the spatial fluctuations in three magnetization components at a specific moment for the two resonant mode frequencies under a zero static magnetic field. Figure 5.9b illustrates the fluctuation of the mz component ($\delta m_z(t)$) along the x-axis, passing through the centre of the nanostructure, for a single oscillation period. In the case of mode one (f_1), the spatial variation of magnetization depicted in Figure 5.9a and the plot of $\delta m_z(x, t)$ in Figure 5.9b reveals that the primary dynamic response originates from the spin texture. This is evident as the core magnetization expands and contracts, concluding that mode one corresponds to the breathing mode of the spin texture. The second mode (f_2) exhibits a hybrid nature, resulting from the excitation of the nanostructure along with the breathing mode of the spin texture. We noticed similar dynamic responses for the respective modes of the spin texture within the stable range of the static magnetic field (B_z).

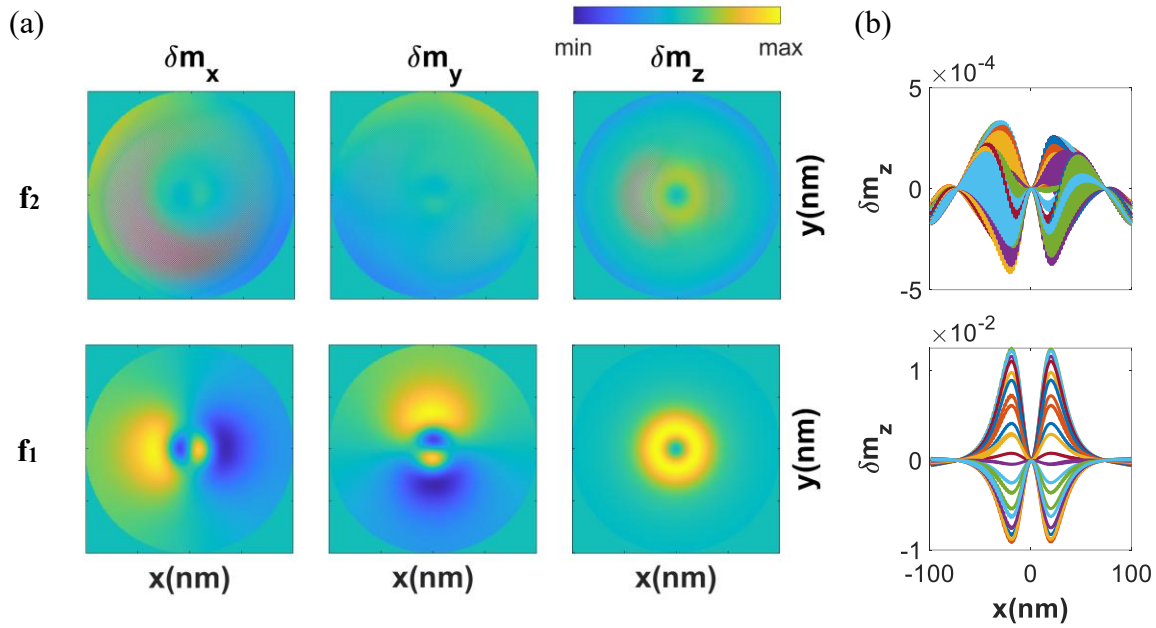

Figure 5.9 Spatial variations in the magnetization of skyrmion spin texture within a circular nanostructure under B_z = 0 mT. **(a)** Three magnetization components spatial fluctuations for modes f_1 and f_2. **(b)** Variation of δm_z along the x - axis for one period of oscillation.

5.5 Summary

Using spin currents under three fixed-layer configurations, we created stable skyrmions in a circular nanostructure. Surprisingly, edge-initiated reversal formed skyrmions only with a perpendicular fixed layer, while core-initiated reversal required specific vortex configurations. Edge reversal needed significantly lower current (0.063 A) compared to core reversal (0.63 A) but was more pulse-width dependent. Both methods resulted in breathing-mode stabilized skyrmions with similar dynamics under alternating fields.

CHAPTER 6

Conclusions and Prospectives

- The topology of the nanostructure is just as crucial as the topology of the spin texture. Which is the best way: flipping spins from the centre or periphery of the system?

The conclusions of our findings are drawn from chapters 3, 4, and 5, which primarily focus on the geometry of the nanostructure.

6.1 Square Nanostructure

In a square nanostructure, we have observed magnetization reversal from the corners of the system due to STT forming an isolated skyrmion. Lower current densities require a longer pulse width to create a skyrmion, which is stabilized through breathing mode. For $J_z < 6x10^{12}$ A/m^2, the action of STT on the free layer is more complex and incomparable to different DMIs. It could be the reason for the unsystematic formation of the skyrmion and antiskyrmions. By decreasing the pulse width to 0.05 ns and increasing the current density to $5x10^{12}$ A/m^2, skyrmion and antiskyrmion lattices are formed from the evolution of the symmetrical magnetic stripes. Antiskyrmion lattice is annihilated during the pulse, and the skyrmion lattice is stable for a longer duration in the case of lower DMIs. Like in real devices, our studies with finite edge roughness are promising to create chiral spin textures using spin-polarized currents. Finally, it is predicted a stable skyrmion lattice and antiskyrmion lattice can be created by tuning the material parameters with the current density and pulse width.

6.2 Rectangular Nanostructure

We showed the creation of stable chiral spin textures through the magnetization reversal using spin-polarized currents in a rectangular nanostructure. The magnetic system with an isotropic DMI helps to stabilize the skyrmions, and an anisotropic DMI stabilizes antiskyrmions. Stable isolated spin texture formation mainly depends on the spin-polarized current density and pulse time. During the current pulse, the spin transfer torque compresses the spin texture; once the pulse is off, the spin texture shows a breathing mode up to 5 ns and stabilizes after. As the size of the stable spin texture increases with increasing DMI strength, the isolated chiral spin texture dynamics are explored under ac magnetic fields for DMI 0.35

mJ/m^2. The dynamic response is similar for skyrmion and antiskyrmion; a primary breathing mode at 1.0 GHz and three hybrid modes at 3.8, 5.2 and 7.0 GHz under zero static field are observed. The resonant mode frequencies(f_1-f_4) exhibited a linear dependence on the static field, and the spatial dynamics response to the corresponding mode frequencies is similar to the zero static field case. In the isolated spin texture creation, it is observed that the spin reversal is earlier for higher DMI due to stronger tilts at the corner edges of the nanostructure. To see the effect of initial configuration dependence on the spin texture formation, we applied a positive current pulse to saturate the state and then reversed the pulse; a spin texture pair evolved from the stripe-like domain. As the skyrmion and antiskyrmion pair formations are similar, we focused mainly on the stable skyrmion pair formation for the current densities and their pulse widths. Finally, the interaction dynamics of the skyrmion pair are studied with the Thiele equation, and it is observed that beyond a critical separation of 78 nm, the skyrmion pair becomes stable.

6.3 Circular Nanostructure

We demonstrated the creation of a stable skyrmion spin texture in a circular nanostructure by employing spin-polarized currents for the three different fixed layer polarizations: (i) Perpendicular, (ii) Diverging vortex, and (iii) Circular vortex. This has been done through two distinct methods: one involving spin reversal at the core with nano contacts and the other via the edges of the nanostructure. It is observed that the formation of a stable skyrmion through the magnetization reversal from the edges of the nanostructure occurs only when the fixed layer polarization is perpendicular to the plane of the nanostructure. When spin reversal is initiated at the centre of the free layer, a stable skyrmion is created only for the diverging vortex and circular vortex fixed layer configurations. In either method, the core size of the skyrmion doesn't depend on the current density and pulse width. In a comparison of both methods for the stable skyrmion creation to the current pulse width of 0.1 ns, the minimum current needed for spin reversal from the periphery of the system (~ 0.063 A) is ten times lower than that required for the spin reversal at the core (~ 0.63 A). At the cost of pulse width, the threshold current can be reduced further for the spin reversal from the boundary case, as it heavily relies on the current pulse width. In both cases, the skyrmion is stabilized through breathing mode once the current is off, and the skyrmion displays similar dynamics under alternating magnetic fields.

In a nutshell, this research reveals the significant influence of nanostructure topology on creating the skyrmion lattice. The findings indicate that spin reversal from the system's periphery offers greater adaptability than spin reversal from the system's centre.

6.4 Future Prospectives

Magnetic skyrmions are a topic of active research in condensed matter physics and materials science. Ongoing research into magnetic skyrmions has unveiled a world of possibilities for their practical applications. These tiny magnetic whirlpools hold the potential to transform various technological domains.

- **High-Density Data Storage:** Magnetic skyrmions offer the potential for significantly higher data storage densities compared to traditional technologies. Ongoing research focuses on optimizing their stability and manipulation for integration into next-generation high-density data storage devices.
- **Spintronic Devices:** Skyrmions hold promise for applications in spintronic devices, particularly in logic and memory functions. This can revolutionize computing by reducing energy consumption and enhancing processing speeds.
- **Skyrmion Dynamics and Interactions:** Ongoing research focuses on understanding the fundamental dynamics and interactions of magnetic skyrmions. Scientists are developing precise techniques for controlling skyrmions' creation, movement, and annihilation, which is crucial for their practical use.
- **Room Temperature Stability:** Researchers are dedicated to identifying materials that can maintain the stability of magnetic skyrmions at room temperature. Recent advances in material design and synthesis have shown promise, creating new possibilities for the practical implementation of skyrmion-based technologies.
- **Skyrmion-Based Sensors:** Magnetic skyrmions demonstrate sensitivity to external magnetic fields, making them suitable for various sensor applications, including biomedical sensing, navigation, and automotive technology.
- **Skyrmions in Quantum Computing:** The unique properties of magnetic skyrmions may benefit quantum computing. Research in this area explores their potential application in qubit design and manipulation.
- **Neuromorphic Computing:** Magnetic skyrmions' distinct characteristics position them favourably for neuromorphic computing applications. Researchers are

investigating their potential to replicate the behaviour of synapses in artificial neural networks, offering advancements in energy-efficient computing and machine learning.

It's important to note that magnetic skyrmion-based research is still a subject of active research and is rapidly evolving. The advancements and ongoing research efforts indicate a promising future for magnetic skyrmions in various technological applications, offering the potential for transformative developments in data storage, computing, sensing, and energy-efficient electronics.

BIBLIOGRAPHY

1. IEA (2022), Data Centres and Data Transmission Networks, IEA, Paris https://www.iea.org/reports/data-centres-and-data-transmission-networks, License: CC BY 4.0
2. Andrae, A.S.G.; Edler, T. On Global Electricity Usage of Communication Technology: Trends to 2030. *Challenges*, *6*, 117-157 (2015).
3. Nicola Jones, How to stop data centers from gobbling up the world's electricity. *Nature* **561**, 163-166 (2018).
4. Beyond CMOS – IEEE International Roadmap for Devices and Systems (IEEE 2018); https://irds.ieee.org/home/what-is-beyond-cmos.
5. Baibich, M. N. et al. Giant magnetoresistance of (001)Fe/(001)Cr magnetic superlattices. *Phys. Rev. Lett.* **61**, 2472–2475 (1988).
6. Binasch, G., Grünberg, P., Saurenbach, F. & Zinn, W. Enhanced magnetoresistance in layered magnetic structures with antiferromagnetic interlayer exchange. *Phys. Rev. B* **39**, 4828–4830 (1989).
7. Slonczewski, J. C. Current-driven excitation of magnetic multilayers. *J. Magn. Magn. Mater.* **159**, L1–L7 (1996).
8. Berger, L. Emission of spin waves by a magnetic multilayer traversed by a current. *Phys. Rev. B* **54**, 9353–9358 (1996).
9. Miron, I. M. et al. Perpendicular switching of a single ferromagnetic layer induced by in-plane current injection. *Nature* **476**, 189–193 (2011).
10. Yuasa, S., Nagahama, T., Fukushima, A., Suzuki, Y. & Ando, K. Giant room-temperature magnetoresistance in single-crystal Fe/MgO/Fe magnetic tunnel junctions. *Nat. Mater.* **3**, 868–871 (2004).
11. Parkin, S. S. P. et al. Giant tunnelling magnetoresistance at room temperature with MgO (100) tunnel barriers. *Nat. Mater.* **3**, 862–867 (2004).
12. Kawahara, T., Ito, K., Takemura, R. & Ohno, H. Spin-transfer torque RAM technology: review and prospect. *Microelectron. Reliab.* **52**, 613–627 (2012).
13. Kent, A. D. & Worledge, D. C. A new spin on magnetic memories. *Nat. Nanotecnolh.* **10**, 187–191 (2015).
14. Apalkov, D., Dieny, B. & Slaughter, J. M. Magnetoresistive random access memory. *Proc. IEEE* **104**, 1796–1830 (2016).

15. Khvalkovskiy, A. V. et al. Basic principles of STT-MRAM cell operation in memory arrays. *J. Phys. D.* **46**, 074001 (2013).
16. Puebla, J., Kim, J., Kondou, K. *et al.* Spintronic devices for energy-efficient data storage and energy harvesting. *Commun Mater* **1**, 24 (2020).
17. McGrath, D. Intel says FinFET-based embedded MRAM is production-ready. *EE Times* (20 February 2019); https://go.nature.com/3gQyWzf
18. Samsung Electronics starts commercial shipment of eMRAM product based on 28nm FD-SOI process. (Samsung, 2019); https://go.nature.com/2KlU8Pj
19. Mason, M. Making new memories: 22nm eMRAM is Ready to Displace eFlash. *GlobalFoundries* (29 Aug 2019); https://go.nature.com/3eBhrCB
20. Dieny, B., Prejbeanu, I.L., Garello, K. *et al.* Opportunities and challenges for spintronics in the microelectronics industry. *Nat Electron* **3**, 446–459 (2020).
21. S.S. Parkin, M. Hayashi, L. Thomas, Magnetic domain-wall racetrack memory, Science 320 (5873), 190–194 (2008).
22. Nagaosa, N. & Tokura, Y. Topological properties and dynamics of magnetic skyrmions. *Nat. Nanotechnol.* **8**, 899–911 (2013).
23. Fert, A., Reyren, N. & Cros, V. Magnetic skyrmions: advances in physics and potential applications. *Nature Rev. Mat.* **2**, 17031 (2017).
24. Dzyaloshinskii, I. E. Theory of helicoidal structures in antiferromagnets. *Sov. Phys. JETP* **19**, 960–971 (1964).
25. Moriya, T. Anisotropic superexchange interaction and weak ferromagnetism. *Phys. Rev.* **120**, 91–98 (1960).
26. Mühlbauer, S. et al. Skyrmion lattice in a chiral magnet. *Science* **323**, 915–919 (2009).
27. X. Yu, et al. "Real-space observation of a two-dimensional skyrmion crystal" *Nature*, 465:901–904 (2010).
28. M. Uchida, Y. Onose, Y. Matsui and Y. Tokura. "Real-space observation of helical spin order" *Science.*, 311:359–361 (2006).
29. W. Munzer, et al. "Skyrmion lattice in the doped semiconductor $Fe_{1-x}Co_xSi$" *Phys. Rev. B*, 81:041203 (2010).
30. T. Adams, et al. "Long-wavelength helimagnetic order and skyrmion lattice phase in Cu_2OSeO_3". *Phys. Rev. Lett.*, 108:237204 (2012).

31. Yu, X., Kanazawa, N., Onose, Y. *et al.* Near room-temperature formation of a skyrmion crystal in thin-films of the helimagnet FeGe. *Nature Mater* **10**, 106–109 (2011).
32. N. Kanazawa, et al. "Possible skyrmion-lattice ground state in the B20 chiral-lattice magnet MnGe as seen via small-angle neutron scattering". *Phys. Rev. B*, 86:134425 (2012).
33. Tanigaki, T. et al. Real-space observation of short-period cubic lattice of skyrmions in MnGe. *Nano Lett.* **15**, 5438 (2015).
34. Münzer, W. et al. Skyrmion lattice in the doped semiconductor Fe_{1-x} Co_x Si. *Phys. Rev. B* **81**, 041203(R) (2010).
35. T. Adams, S. Muehlbauer, A. Neubauer, W. Muenzer, F. Jonietz, R. Georgii, B. Pedersen, P. Boeni, A. Rosch, and C. Pfleiderer, *Skyrmion lattices domains in* $Fe_{1-x}Co_xSi$, J. Phys.: Conf. Ser. **200**, 032001 (2010).
36. Heinze, S. *et al.* "Spontaneous atomic-scale magnetic skyrmion lattice in two dimensions" *Nat. Phys.*, **7**:713–718 (2011).
37. Romming, N. *et al.* "Writing and deleting single magnetic skyrmions" *Science*, 341:636–639, (2013).
38. Heinze, S. *et al.* "Real-space imaging of two-dimensional antiferromagnetism on the atomic scale" *Science*, 288:1805–1808 (2000).
39. Moreau-Luchaire, C. *et al.* "Additive interfacial chiral interaction in multilayers for stabilization of small individual skyrmions at room temperature" *Nat. Nanotechnol.*, 11:444–448 (2016).
40. Jiang, W. *et al.* "Blowing magnetic skyrmion bubbles" *Science*, 349:283–286 (2015).
41. Woo, S. *et al.* "Observation of room-temperature magnetic skyrmions and their current-driven dynamics in ultrathin metallic ferromagnets" *Nat. Mater.*, 15:501–506 (2016).
42. Boulle, O. *et al.* "Room-temperature chiral magnetic skyrmions in ultrathin magnetic nanostructures" *Nat. Nanotechnol.* 11:449–454, (2016).
43. Tokura, Y. & Kanazawa, N. Magnetic skyrmion materials. *Chem. Rev.* **121**, 2857 (2021).
44. Xudong Huai and Thao T. Tran. Design Principles for Noncentrosymmetric Materials. Annual Review of Materials Research, Vol.53:253-274 (2023).
45. Yu, X. Z. et al. Variation of skyrmion forms and their stability in MnSi thin plates. *Phys. Rev. B* **91**, 054411 (2015).
46. Shibata, K., Yu, X., Hara, T. *et al.* Towards control of the size and helicity of skyrmions in helimagnetic alloys by spin–orbit coupling. *Nature Nanotech* **8**, 723–728 (2013).

47. S. Seki, et al. Observation of Skyrmions in a Multiferroic Material. *Science* **336**,198-201 (2012).
48. Yu, X.Z., Koshibae, W., Tokunaga, Y. *et al.* Transformation between meron and skyrmion topological spin textures in a chiral magnet. *Nature* **564**, 95–98 (2018).
49. Nayak, A., Kumar, V., Ma, T. *et al.* Magnetic antiskyrmions above room temperature in tetragonal Heusler materials. *Nature* **548**, 561–566 (2017).
50. Hsu, PJ., Kubetzka, A., Finco, A. *et al.* Electric-field-driven switching of individual magnetic skyrmions. *Nature Nanotech* **12**, 123–126 (2017).
51. Soumyanarayanan, A., Raju, M., Gonzalez Oyarce, A. *et al.* Tunable room-temperature magnetic skyrmions in Ir/Fe/Co/Pt multilayers. *Nature Mater* **16**, 898–904 (2017).
52. Legrand, W., Maccariello, D., Ajejas, F. *et al.* Room-temperature stabilization of antiferromagnetic skyrmions in synthetic antiferromagnets. *Nat. Mater.* **19**, 34–42 (2020).
53. Chen, R. *et al.* Realization of isolated and high-density skyrmions at room temperature in uncompensated synthetic antiferromagnets. *J. Nano Lett.* **20**(5), 3299–3305 (2020).
54. Kézsmárki, I., Bordács, S., Milde, P. *et al.* Néel-type skyrmion lattice with confined orientation in the polar magnetic semiconductor GaV_4S_8. *Nature Mater* **14**, 1116–1122 (2015).
55. Bordács, S., Butykai, A., Szigeti, B.G. *et al.* Equilibrium Skyrmion Lattice Ground State in a Polar Easy-plane Magnet. *Sci Rep* **7**, 7584 (2017).
56. Zhang, X. *et al.* Skyrmion-electronics: Writing, deleting, reading and processing magnetic skyrmions toward spintronic applications. *J. Phys. Condens. Matter* **32**, 143001 (2020).
57. W. F. Brown, Micromagnetics. Interscience Publishers, New York, (1963).
58. Abert, C. Micromagnetics and spintronics: models and numerical methods. *Eur. Phys. J. B* **92**, 120 (2019).
59. Leliaert, J. & Mulkers, J. Tomorrow's micromagnetic simulations. *J. Appl. Phys.* **125**, 180901 (2019).
60. R. M. Dreizler and E. K. U. Gross. Density functional theory. Berlin: Springer, (1990).
61. Brown W F and LaBonte A E. Structure and energy of one-dimensional domain walls in ferromagnetic thin films *J. Appl. Phys.* **36** 1380–6 (1965).
62. M. J. Donahue, Interagency report NISTIR 6376, NIST, Gaithersburg, MD, (1999).

63. T. L. Gilbert, "A phenomenological theory of damping in ferromagnetic materials," in *IEEE Transactions on Magnetics*, vol. 40, no. 6, pp. 3443-3449, (2004).
64. Vansteenkiste, A. et al. The design and verification of MuMax3. *AIP Advances* **4**, 107133 (2014).
65. Mulkers, J., Van Waeyenberge, B. & Milošević, M. V. Effects of spatially engineered Dzyaloshinskii-Moriya interaction in ferromagnetic films. *Phys. Rev. B* **95**, 144401 (2017).
66. Brataas, A., Kent, A. & Ohno, H. Current-induced torques in magnetic materials. *Nature Mater* **11**, 372–381 (2012).
67. Slonczewski, J. C. Currents and torques in metallic magnetic multilayers. *J. Magn. Magn. Mater.* **247,** 324 (2002).
68. E. B. Myers, D. C. Ralph, J. A. Katine, R. N. Louie, R. A. Buhrman, Current-Induced Switching of Domains in Magnetic Multilayer Devices. *Science* **285**, 867 (1999).
69. M. Tsoi, A. G. M. Jansen, J. Bass, W. C. Chiang, M. Seck, V. Tsoi, P. Wyder, Excitation of a Magnetic Multilayer by an Electric Current. *Physical Review Letters* **80**, 4281-4284 (1998).
70. J. Xiao, A. Zangwill, and M. D. Stiles. Boltzmann test of Slonczewski's theory of spin-transfer torque, Physical Review B **70**(17), 172405 (2004).
71. Lu, X., Fei, R., Zhu, L. *et al.* Meron-like topological spin defects in monolayer $CrCl_3$. *Nat Commun* **11,** 4724 (2020).
72. Börge Göbel. *et al.* Magnetic bimerons as skyrmion analogues in in-plane magnets. Phys. Rev. B **99**, 060407(R) (2019).
73. Se Kwon Kim. Dynamics of bimeron skyrmions in easy-plane magnets induced by a spin supercurrent. Phys. Rev. B **99**, 224406 (2019).
74. Jani, H., Lin, JC., Chen, J. *et al.* Antiferromagnetic half-skyrmions and bimerons at room temperature. *Nature* **590,** 74–79 (2021).
75. Parkin, S., Yang, SH. Memory on the racetrack. *Nature Nanotech* **10,** 195–198 (2015).
76. Guoqiang Yu. *et al.* 2017 Room-temperature skyrmion shift device for memory application *Nano Lett.* **17** 261 (2016).
77. Zhang S. *et al.* Topological computation based on direct magnetic logic communication *Sci. Rep.* **5** 15773 (2015).
78. Zhang S F *et al.* Current-induced magnetic skyrmions oscillator *New J. Phys.* **17,** 023061 (2015).

79. Song, K.M. *et al.* Skyrmion-based artificial synapses for neuromorphic computing. *Nat Electron* **3,** 148–155 (2020).
80. Sai Li. *et al.* Magnetic skyrmion-based artificial neuron device. *Nanotechnology* **28** 31LT01 (2017).
81. Bourianoff G, *et al.* Potential implementation of reservoir computing models based on magnetic skyrmions *AIP Adv.* **8** 055602 (2018).
82. Koshibae, W., Nagaosa, N. Creation of skyrmions and antiskyrmions by local heating. *Nat Commun* **5,** 5148 (2014).
83. Bogdanov AN, Rößler UK, Wolf M, Müller KH. Magnetic structures and reorientation transitions in noncentrosymmetric uniaxial antiferromagnets. Phys Rev B **66**:214410 (2002).
84. Hoffmann M, et al. Antiskyrmions stabilized at interfaces by anisotropic Dzyaloshinskii-Moriya interactions. Nat. Commun. (2017).
85. Güngördü U, et al. stability of skyrmion lattices and symmetries of quasi-two-dimensional chiral magnets. Phys Rev B **93**:064428 (2016).
86. Tchoe Y and Han J H Skyrmion generation by current *Phys. Rev.* B **85** 174416 (2012).
87. Sampaio J, Cros V, Rohart S, Thiaville A and Fert A Nucleation, stability and current-induced motion of isolated magnetic skyrmions in nanostructures *Nat. Nanotechnol.* **8** 839 (2013).
88. Yuan H Y and Wang X R Skyrmion creation and manipulation by nanosecond current pulses *Sci. Rep.* **6** 22638 (2016).
89. Yin G, et al. Topological charge analysis of ultrafast single skyrmion creation *Phys. Rev.* B **93** 174403 (2016).
90. Woo S *et al* Spin–orbit torque-driven skyrmion dynamics revealed by time-resolved x-ray microscopy *Nat. Commun.* **8** 15573 (2017).
91. Lemesh I *et al.* Current-induced skyrmion generation through morphological thermal transitions in chiral ferromagnetic heterostructures *Adv. Mater.* **30** 1870372 (2018).
92. Hrabec A, et al. Current-induced skyrmion generation and dynamics in symmetric bilayers *Nat. Commun.* **8** 15765 (2017).
93. Woo, S., Litzius, K., Krüger, B. *et al.* Observation of room-temperature magnetic skyrmions and their current-driven dynamics in ultrathin metallic ferromagnets. *Nature Mater* **15,** 501–506 (2016).

94. Brandão, J., Dugato, D.A., Seeger, R.L. *et al.* Observation of magnetic skyrmions in unpatterned symmetric multilayers at room temperature and zero magnetic field. *Sci Rep* **9,** 4144 (2019).
95. F Garcia-Sanchez *et al*. A Skyrmion-based spin-torque nano-oscillator. *New J. Phys.* **18** 075011 (2016).
96. Kim, J.-V. et al. Breathing modes of confined skyrmions in ultrathin magnetic dots. Phys. Rev. B 90, 064410 (2014).
97. Koshibae, W. & Nagaosa, N. Theory of antiskyrmions in magnets. *Nat. Commun. 7:10542* (2016).
98. Moon, K.-W. *et al.* Skyrmion motion driven by oscillating magnetic field. *Sci. Rep.* **6**, 20360 (2016).
99. Shiino, T. *et al.* Inertia-driven resonant excitation of a magnetic skyrmion. *Sci Rep* **7,** 13993 (2017).
100. Zhang, X. *et al*. Skyrmion-skyrmion and skyrmion-edge repulsions in skyrmion-based racetrack memory. *Sci. Rep.* **5**, 7643 (2015).
101. Du H *et al*. Interaction of individual skyrmions in a nanostructured cubic chiral magnet *Phys. Rev. Lett.* **120** 197203 (2018).
102. D Capic *et al*. Skyrmion-skyrmion interaction in a magnetic film. *J. Phys.: Condens. Matter* **32** 415803 (2020).
103. Kandukuri, S., Murthy, V.S.N. & Thiruvikraman, P.K. Isolated skyrmion, skyrmion lattice and antiskyrmion lattice creation through magnetization reversal in Co/Pd nanostructure. *Sci Rep* **11**, 18945 (2021).
104. Camosi, L. et al. Anisotropic Dzyaloshinskii–Moriya interaction in ultrathin epitaxial Au/Co/W(110). *Phys. Rev. B* **95**, 214422 (2017).
105. Thiele, A. Steady-state motion of magnetic domains. *Phys. Rev. Lett.* **30**, 230 (1973).

LIST OF PUBLICATIONS AND PRESENTATIONS

1. Kandukuri, S., Murthy, V.S.N. & Thiruvikraman, P.K. Isolated skyrmion, skyrmion lattice and antiskyrmion lattice creation through magnetization reversal in Co/Pd nanostructure. *Sci Rep* **11**, 18945 (2021).
2. Sateesh K., Felipe G. S., Thiruvikraman P.K., Satya Narayana Murthy V., Chiral spin textures creation and dynamics in a rectangular nanostructure. arXiv:2310.12129 [cond-mat.mes-hall] (IOP: Journal of Physics D, Applied Physics, 2024) (Provisionally Accepted).
3. Sateesh K., Satya Narayana Murthy V., Unveiling the influence of fixed layer polarization on skyrmion nucleation and dynamics in circular geometry. (JMMM, 2024). (Under review)
4. Oral presentation on “Antiskyrmion nucleation in magnetic tunnel junctions”. IEEE Magnetics ATC-ATG 2023.
5. Sateesh K., Satya Narayana Murthy V., Skyrmion creation and dynamics in a circular nanostructure under distinct fixed layer polarizations. ICMAGMA 2023.

BRIEF BIOGRAPHY OF THE CANDIDATE

Sateesh Kandukuri is a distinguished scholar, having obtained a B.Sc. degree in Mathematics, Physics, and Electronics from Shantiniketan Degree College, affiliated with Kakatiya University, Sathupally, Telangana, in 2006 and an M.Sc. Physics from Loyola Academy Degree & P.G. College affiliated to Osmania University, Hyderabad, Telangana, India, in 2009. He has taught engineering physics for nine years in reputed engineering colleges in Hyderabad, Telangana. He is pursuing a PhD in Physics at Birla Institute of Technology and Science Pilani, Hyderabad Campus, Telangana, India. Sateesh has contributed to two Journals and delivered two conference presentations. His research focus involves the micromagnetic study of magnetic skyrmions and multilayer thin film fabrication using magnetron sputtering techniques for spintronic device applications.

BRIEF BIOGRAPHY OF THE SUPERVISOR

Name: V. Satya Narayana Murthy
Designation: Associate Professor
Department of Physics
BITS Pilani Hyderabad Campus – 500078

Research Interest: Magnetic thin films and nanostructures, Magnetic skyrmions, Magnetic sensors for non-destructive testing of materials, and Micromagnetic study of magnetic materials.

Research Experience: Successfully guided a Ph.D. student; three are working for their doctoral degree. Several M.Sc. students have worked on their dissertations. Completed a DST SERB project on magnetoimpedance sensors.

Education: PhD from the Department of Physics, IIT Madras

Postdoc: Worked as a postdoctoral fellow in the Department of Electrical Engineering, National University of Singapore, and the Department of Mechanical Engineering, IIT Madras.

Recent Publications:

P. Sivasankaraiah, P. Nagaraju and **V. Satya Narayana Murthy** (2023) Effect Annealing Temperature on Pure and Al-Doped Iron Oxide Thin Films for Formaldehyde Gas Sensing Application, ECS J. Solid State Sci. Technol, 12, 097005.

P. Sivasankaraiah, P. Nagaraju and **V. Satya Narayana Murthy** (2022) Spray-deposited iron oxide thin films for the detection of ammonia at room temperature, J Mater Sci: Mater Electron 33, 17064–17078.

Sateesh Kandukuri, **V. Satya Narayana Murthy** and P. K. Thiruvikraman (2021) Isolated skyrmion, skyrmion lattice and antiskyrmion lattice creation through magnetization reversal in Co/Pd nanostructure, Sci Rep 11, 18945.